

# Experimental Investigation and Modeling of Scale

## Effects in Micro Jet Pumps

by

William Geoffrey Gardner

Department of Mechanical Engineering and Material Science  
Duke University

Date: \_\_\_\_\_

Approved:

---

Jonathan Protz, Supervisor

---

F. Hadley Cocks

---

Teh Tan

---

W. Neal Simmons

---

Michael Gustafson II

Dissertation submitted in partial fulfillment of the requirements for the degree of  
Doctor of Philosophy in the Department of Mechanical Engineering and Material  
Science  
in the Graduate School of Duke University  
2011

ABSTRACT

(Microscale Power Generation and Propulsion, Power MEMS)

Experimental Investigation and Modeling of Scale Effects in  
Micro Jet Pumps

by

William Geoffrey Gardner

Department of Mechanical Engineering and Material Science  
Duke University

Date: \_\_\_\_\_

Approved:

\_\_\_\_\_  
Jonathan Protz, Supervisor

\_\_\_\_\_  
F. Hadley Cocks

\_\_\_\_\_  
Teh Tan

\_\_\_\_\_  
W. Neal Simmons

\_\_\_\_\_  
Michael Gustafson II

An abstract of a dissertation submitted in partial fulfillment of the requirements for  
the degree of Doctor of Philosophy in the Department of Mechanical Engineering  
and Material Science  
in the Graduate School of Duke University  
2011

Copyright © 2011 by William Geoffrey Gardner  
All rights reserved

# Abstract

Since the mid-1990s there has been an active effort to develop hydrocarbon-fueled power generation and propulsion systems on the scale of centimeters or smaller. This effort led to the creation and expansion of a field of research focused around the design and reduction to practice of Power MEMS (microelectromechanical systems) devices, beginning first with microscale jet engines and a generation later more broadly encompassing MEMS devices which generate power or pump heat. Due to small device scale and fabrication techniques, design constraints are highly coupled and conventional solutions for device requirements may not be practicable.

This thesis describes the experimental investigation, modeling and potential applications for two classes of microscale jet pumps: jet ejectors and jet injectors. These components pump fluids with no moving parts and can be integrated into Power MEMS devices to satisfy pumping requirements by supplementing or replacing existing solutions. This thesis presents models developed from first principles which predict losses experienced at small length scales and agree well with experimental results. The models further predict maximum achievable power densities at the onset of detrimental viscous losses.

To my grandfather, Russell Menese “Neese” Gardner (T’42, L’48)

# Contents

|   |            |
|---|------------|
| <b>Abstract</b>                                       | <b>iv</b>  |
| <b>List of Tables</b>                                 | <b>ix</b>  |
| <b>List of Figures</b>                                | <b>xi</b>  |
| <b>List of Abbreviations and Symbols</b>              | <b>xiv</b> |
| <b>Acknowledgements</b>                               | <b>xvi</b> |
| <b>1 Introduction</b>                                 | <b>1</b>   |
| 1.1 Motivation . . . . .                              | 1          |
| 1.1.1 Microengines . . . . .                          | 1          |
| 1.1.2 Energy storage and conversion . . . . .         | 2          |
| 1.2 Scaling Laws . . . . .                            | 3          |
| 1.2.1 Cube-square law . . . . .                       | 4          |
| 1.2.2 Scale effects . . . . .                         | 6          |
| 1.2.3 Scale effects in microrockets . . . . .         | 10         |
| 1.2.4 Scale effects in microturbomachinery . . . . .  | 13         |
| 1.3 Current State of the Art . . . . .                | 16         |
| 1.3.1 Turbomachinery tip-speed requirement . . . . .  | 17         |
| 1.3.2 Limitations of macroscale approaches . . . . .  | 18         |
| 1.3.3 Gas bearings . . . . .                          | 20         |
| 1.3.4 Clearances and tolerances . . . . .             | 22         |
| 1.4 Power MEMS . . . . .                              | 24         |
| 1.4.1 Power MEMS applications for jet pumps . . . . . | 24         |
| 1.5 Jet Pumps: A Brief History . . . . .              | 31         |
| 1.5.1 Steam locomotives . . . . .                     | 31         |
| 1.5.2 Jet ejectors . . . . .                          | 32         |
| 1.5.3 Jet injectors . . . . .                         | 33         |
| 1.5.4 Historical perspective . . . . .                | 35         |
| 1.6 Objective . . . . .                               | 37         |
| 1.7 Overview . . . . .                                | 38         |

|          |   |           |
|----------|---|-----------|
| <b>2</b> | <b>Single-Stage Ejector</b>                   | <b>39</b> |
| 2.1      | Motivation . . . . .                          | 39        |
| 2.2      | Background and Literature Search . . . . .    | 40        |
| 2.2.1    | Power MEMS Applications . . . . .             | 40        |
| 2.2.2    | Macroscale Applications . . . . .             | 41        |
| 2.2.3    | Early Work and Theory . . . . .               | 42        |
| 2.3      | Objective . . . . .                           | 42        |
| 2.4      | Theory and Modeling . . . . .                 | 43        |
| 2.4.1    | Physical Description . . . . .                | 43        |
| 2.4.2    | Model Approach . . . . .                      | 44        |
| 2.4.3    | Analytic Model . . . . .                      | 47        |
| 2.4.4    | Efficiency . . . . .                          | 50        |
| 2.4.5    | Power Density . . . . .                       | 52        |
| 2.5      | Experimental Approach . . . . .               | 53        |
| 2.6      | Experimental Results and Discussion . . . . . | 58        |
| 2.7      | Conclusions . . . . .                         | 63        |
| <br>     |   |           |
| <b>3</b> | <b>Injector</b>                               | <b>64</b> |
| 3.1      | Motivation . . . . .                          | 64        |
| 3.2      | Background and Literature Search . . . . .    | 65        |
| 3.2.1    | Power MEMS Applications . . . . .             | 65        |
| 3.2.2    | Macroscale Applications . . . . .             | 66        |
| 3.2.3    | Early Work and Theory . . . . .               | 66        |
| 3.3      | Objective . . . . .                           | 67        |
| 3.4      | Theory and Modeling . . . . .                 | 68        |
| 3.4.1    | Physical Description . . . . .                | 68        |
| 3.4.2    | Typical Injector Geometry . . . . .           | 70        |
| 3.4.3    | Model Approach . . . . .                      | 76        |
| 3.4.4    | Analytic Model . . . . .                      | 77        |
| 3.4.5    | Efficiency . . . . .                          | 83        |
| 3.4.6    | Power Density . . . . .                       | 84        |
| 3.5      | Experimental Approach . . . . .               | 85        |
| 3.6      | Experimental Results and Discussion . . . . . | 91        |
| 3.7      | Conclusions . . . . .                         | 92        |
| <br>     |   |           |
| <b>4</b> | <b>Multi-Stage Ejector</b>                    | <b>95</b> |
| 4.1      | Motivation . . . . .                          | 95        |
| 4.2      | Background and Literature Search . . . . .    | 95        |
| 4.3      | Objective . . . . .                           | 95        |
| 4.4      | Experimental Approach . . . . .               | 96        |
| 4.5      | Experimental Results and Discussion . . . . . | 98        |
| 4.6      | Conclusions . . . . .                         | 101       |

|          |   |            |
|----------|---|------------|
| <b>5</b> | <b>Conclusions</b>  | <b>102</b> |
| 5.1      | Summary of Results and Conclusions . . . . .                  | 102        |
| 5.1.1    | Single-Stage Ejector . . . . .                                | 102        |
| 5.1.2    | Injector . . . . .  | 102        |
| 5.2      | Implications . . . . .  | 103        |
| 5.2.1    | Single-Stage Ejector . . . . .                                | 103        |
| 5.2.2    | Injector . . . . .  | 103        |
| 5.3      | Suggestions for Future Work . . . . .                         | 103        |
| 5.3.1    | Applications . . . . .  | 103        |
| 5.3.2    | Modeling . . . . .  | 104        |
| 5.3.3    | Other Flow Configurations . . . . .                           | 104        |
| <b>A</b> | <b>Single-Stage Ejector: Detailed Model</b>                   | <b>106</b> |
| A.1      | Geometry . . . . .  | 106        |
| A.2      | Conservation of Mass . . . . .                                | 109        |
| A.3      | Conservation of Axial Momentum . . . . .                      | 111        |
| A.3.1    | Motive Fluid: Compressible Flow with Viscous Losses . . . . . | 114        |
| A.3.2    | Secondary Fluid: Inlet Losses . . . . .                       | 121        |
| A.3.3    | Discharge Fluid: Mixer Skin Friction . . . . .                | 123        |
| A.4      | General Model with Losses . . . . .                           | 126        |
| <b>B</b> | <b>Injector: Detailed Model</b>                               | <b>127</b> |
| B.1      | Geometry . . . . .  | 128        |
| B.2      | Conservation of Mass . . . . .                                | 131        |
| B.2.1    | Conservation of Mass and Energy: Minimum Entrainment Ratio    | 132        |
| B.3      | Conservation of Axial Momentum . . . . .                      | 133        |
| B.3.1    | Secondary Fluid: Inlet Losses . . . . .                       | 135        |
| B.3.2    | Motive Fluid: Compressible Flow with Viscous Losses . . . . . | 139        |
| B.3.3    | Discharge Fluid: Mixer Skin Friction and Blockage . . . . .   | 145        |
| B.4      | General Model with Losses . . . . .                           | 149        |
| <b>C</b> | <b>Nozzle Skin Friction Integral Tables</b>                   | <b>151</b> |
| C.1      | Newton-Cotes Numerical Integration . . . . .                  | 151        |
| C.2      | Tables for $\gamma = 1.1$ . . . . .                           | 153        |
| C.3      | Tables for $\gamma = 1.2$ . . . . .                           | 155        |
| C.4      | Tables for $\gamma = 1.3$ . . . . .                           | 157        |
| C.5      | Tables for $\gamma = 1.4$ . . . . .                           | 159        |
|          | <b>Bibliography</b>   | <b>161</b> |
|          | <b>Biography</b>  | <b>170</b> |

# List of Tables

|      |  |     |
|------|--|-----|
| 1.1  | Skin friction flow regime constants . . . . .  | 7   |
| 1.2  | Hydrodynamic development length flow regime constants . . . . .                          | 7   |
| 1.3  | Boundary layer flow regime constants . . . . .   | 8   |
| 1.4  | Size, speed and efficiency comparison between a microturbine and GE-90 turbine . . . . . | 16  |
| 2.1  | Ejector design geometry . . . . .  | 54  |
| 2.2  | Comparison of design versus realized motive nozzle geometry . . . . .                    | 54  |
| 2.3  | Comparison of design versus realized ejector geometry . . . . .                          | 54  |
| 2.4  | Comparison of nozzle exit momentum for ethanol vapor and nitrogen gas . . . . .          | 62  |
| 3.1  | Typical injector area ratios . . . . .   | 71  |
| 3.2  | Typical injector expansion/contraction ratios . . . . .                                  | 72  |
| 3.3  | Typical injector half-angles . . . . .   | 73  |
| 3.4  | Typical injector length-to-diameter ratios . . . . .                                     | 74  |
| 3.5  | Combining cone primary vent . . . . .  | 74  |
| 3.6  | Delivery cone starting vent . . . . .  | 75  |
| 3.7  | Model inputs for loss magnitude plot . . . . .   | 82  |
| 3.8  | Characteristic magnitudes for terms in the injector model . . . . .                      | 83  |
| 3.9  | Comparison of design versus realized injector geometry . . . . .                         | 85  |
| 3.10 | Comparison of design versus realized combining cone geometry . . . . .                   | 86  |
| 4.1  | Ejector design geometry . . . . .  | 97  |
| 4.2  | Comparison of design versus realized motive nozzle geometry . . . . .                    | 97  |
| 4.3  | Comparison of design versus realized ejector geometry . . . . .                          | 97  |
| 4.4  | Throat and secondary mixer Reynolds numbers . . . . .                                    | 98  |
| A.1  | Typical values for computation of motive nozzle hydrodynamic loss . . . . .              | 120 |
| B.1  | Typical values for computation of motive nozzle hydrodynamic loss . . . . .              | 145 |
| B.2  | Boundary layer flow regime constants . . . . .   | 148 |
| C.1  | Skin friction flow regime constants . . . . .  | 152 |
| C.2  | Nozzle integrals and parameters for $\gamma = 1.1$ . . . . .                             | 154 |

|     |  |     |
|-----|--|-----|
| C.3 | Nozzle integrals and parameters for $\gamma = 1.2$ | 156 |
| C.4 | Nozzle integrals and parameters for $\gamma = 1.3$ | 158 |
| C.5 | Nozzle integrals and parameters for $\gamma = 1.4$ | 160 |

# List of Figures

|      |   |    |
|------|---|----|
| 1.1  | Energy densities of some common fuels . . . . .   | 2  |
| 1.2  | System energy densities for various fuels and conversion means . . . . .                              | 4  |
| 1.3  | System energy densities for various fuels and conversion means . . . . .                              | 5  |
| 1.4  | Hydrodynamic entry length . . . . .   | 6  |
| 1.5  | Boundary layer, skin friction and hydrodynamic development length<br>versus Reynolds number . . . . . | 9  |
| 1.6  | Effective flow area versus Reynolds number . . . . .  | 10 |
| 1.7  | Size comparison between a microrocket and a Saturn V . . . . .  | 12 |
| 1.8  | Thrust coefficient versus Reynolds number for a $37.5\mu m$ nozzle . . . . .                          | 13 |
| 1.9  | Model results for thrust coefficient versus Reynolds number for a<br>$37.5\mu m$ nozzle . . . . .     | 14 |
| 1.10 | Thrust efficiency for a $37.5\mu m$ throat nozzle . . . . .   | 15 |
| 1.11 | Boundary layer thickness from the nozzle throat to exit . . . . .                                     | 16 |
| 1.12 | Turbine efficiency as a function of diameter and velocity ratio . . . . .                             | 17 |
| 1.13 | Size comparison between a microengine and a GE-90 . . . . .   | 18 |
| 1.14 | System energy densities for microengines compared to batteries . . . . .                              | 19 |
| 1.15 | RPM as a function of rotor tip speed . . . . .  | 20 |
| 1.16 | Examples of miniaturized conventional bearings . . . . .  | 21 |
| 1.17 | Hydrodynamic thrust bearings and hydrostatic thrust bearings . . . . .                                | 22 |
| 1.18 | Schematic of tip leakage over a turbomachine blade . . . . .  | 23 |
| 1.19 | Schematic of the Power MEMS field . . . . .   | 24 |
| 1.20 | Schematic of the Power MEMS applications for micro jet pumps . . . . .                                | 25 |
| 1.21 | Conventional steam locomotive cycle schematic . . . . .   | 26 |
| 1.22 | Steam locomotive (Rankine) cycle schematic with a turbine . . . . .                                   | 27 |
| 1.23 | Turbocharged Rankine cycle . . . . .  | 28 |
| 1.24 | Cold power turbine Brayton and Rankine combined cycle . . . . .                                       | 29 |
| 1.25 | Schematic of a microrocket bipropellant injector-pumped expander cycle . . . . .                      | 30 |
| 1.26 | Typical steam locomotive engine flow paths and schematic . . . . .                                    | 31 |
| 1.27 | Lempor nozzle . . . . .   | 33 |
| 1.28 | Picture of a Kylchap blastpipe . . . . .  | 34 |
| 1.29 | Drawing of a multi-stage Kylchap blastpipe and chimney . . . . .                                      | 35 |
| 1.30 | Giffard's injector from his 1860 US patent . . . . .  | 36 |
| 1.31 | Cross section of a self-acting Penberthy injector . . . . .   | 37 |

|      |  |     |
|------|--|-----|
| 2.1  | Example ejector assembly and flow paths . . . . .  | 44  |
| 2.2  | Ejector assembly and flow paths . . . . .  | 45  |
| 2.3  | Control volume detailing nomenclature . . . . .  | 46  |
| 2.4  | Magnitude of losses versus Reynolds number . . . . .   | 49  |
| 2.5  | Optimum efficiency line . . . . .  | 51  |
| 2.6  | Optimum efficiency line with $C_d = 0.5$ . . . . .   | 52  |
| 2.7  | SEM images of (a) $64\mu m$ nozzle, (b) $187\mu m$ nozzle, (c) $733\mu m$ nozzle . . . . .   | 55  |
| 2.8  | Ejector test rig . . . . .   | 57  |
| 2.9  | Nitrogen mass flow experimental results compared to an isentropic flow model for a $187\mu m$ throat diameter nozzle with a 2.7:1 expansion ratio. . . . . | 59  |
| 2.10 | Model and experimental data for ejector efficiency and suction draft performance versus entrainment ratio for nitrogen gas / air . . . . .                 | 60  |
| 2.11 | Model and experimental data for ejector efficiency and suction draft performance versus entrainment ratio for ethanol vapor / air . . . . .                | 61  |
| 2.12 | Model and experimental data for power density and ejector efficiency as a function of nozzle throat diameter . . . . .                                     | 62  |
|      |  |     |
| 3.1  | Schematic of the injector test piece, showing the motive nozzle, combining cone and flow paths . . . . .   | 68  |
| 3.2  | Injector nomenclature . . . . .  | 70  |
| 3.3  | Injector control volume . . . . .  | 77  |
| 3.4  | Magnitude of losses versus Reynolds number . . . . .   | 82  |
| 3.5  | Injector assembly and flow paths . . . . .   | 86  |
| 3.6  | SEM images of (a) $64\mu m$ nozzle, (b) $187\mu m$ nozzle, (c) $733\mu m$ nozzle . . . . .   | 87  |
| 3.7  | Injector test rig . . . . .  | 89  |
| 3.8  | Injector test article assembly . . . . .   | 91  |
| 3.9  | Cantilever beam FEA . . . . .  | 92  |
| 3.10 | Nondimensional injector performance across different boiler pressures for ethanol vapor and liquid . . . . .   | 93  |
| 3.11 | Injector power density and efficiency as a function of nozzle throat diameter . . . . .  | 94  |
|      |  |     |
| 4.1  | Schematic and nomenclature for a multi-stage ejector . . . . .   | 96  |
| 4.2  | Schematic and nomenclature for a multi-stage ejector . . . . .   | 99  |
| 4.3  | Computed isentropic thrust coefficients vs. entrainment ratio . . . . .  | 100 |
|      |  |     |
| A.1  | Jet ejector assembly and flow paths . . . . .  | 107 |
| A.2  | Jet ejector nomenclature . . . . .   | 108 |
| A.3  | Constant area control volume detailing nomenclature . . . . .  | 110 |
|      |  |     |
| B.1  | Jet ejector assembly and flow paths . . . . .  | 128 |
| B.2  | Jet injector assembly and flow paths . . . . .   | 129 |
| B.3  | Injector nomenclature . . . . .  | 130 |

|     |                                   |     |
|-----|-----------------------------------|-----|
| B.4 | Injector control volume . . . . . | 131 |
|-----|-----------------------------------|-----|

# List of Abbreviations and Symbols

|           |   |  |
|-----------|---|--|
| $M$       | = | Mach number                                  |
| $Re$      | = | Reynolds number                              |
| $a_o$     | = | local speed of sound [ $m/s$ ]               |
| $u$       | = | velocity [ $m/s$ ]                           |
| $C_F$     | = | thrust coefficient                           |
| $F$       | = | force [ $N$ ]                                |
| $C_f$     | = | skin friction coefficient                    |
| $f$       | = | Darcy friction factor                        |
| $\dot{m}$ | = | mass flow rate [ $kg/s$ ]                    |
| $m''$     | = | mass flux [ $kg/m^2 - s$ ]                   |
| $\dot{Q}$ | = | heat transfer rate [ $W$ ]                   |
| $\dot{W}$ | = | power [ $W$ ]                                |
| $t_{res}$ | = | combustion residence time [ $s$ ]            |
| $h_{vap}$ | = | latent heat of vaporization [ $kJ/kg$ ]      |
| $c_p$     | = | specific heat [ $J/kgK$ ]                    |
| $R$       | = | gas constant [ $J/kgK$ ]                     |
| $P$       | = | static pressure [ $atm$ ]                    |
| $P_t$     | = | total pressure [ $atm$ ]                     |
| $T$       | = | static temperature [ $K$ ]                   |
| $T_t$     | = | total temperature [ $K$ ]                    |
| $T_{NBP}$ | = | normal boiling point at STP [ $K$ ]          |
| $T_{sat}$ | = | saturation temperature [ $K$ ]               |
| $L$       | = | length [ $m$ ]                               |
| $D_H$     | = | hydraulic diameter [ $m$ ]                   |
| $D$       | = | diameter [ $m$ ]                             |
| $V$       | = | volume [ $m^3$ ]                             |
| $C$       | = | flow regime coefficient                      |
| $m$       | = | flow regime Reynolds number exponent         |
| $n$       | = | flow regime length-to-diameter exponent      |
| $a$       | = | ejector area ratio, $A_s/A_{m,e}$            |
| $\alpha$  | = | entrainment ratio, $\dot{m}_s/\dot{m}_m$     |
| $\theta$  | = | expansion / contraction half-angle [ $deg$ ] |
| $\gamma$  | = | specific heat ratio                          |

|                   |   |                                       |
|-------------------|---|---------------------------------------|
| $\epsilon$        | = | nozzle expansion ratio, $A_e/A^*$     |
| $\kappa$          | = | expansion / contraction ratio         |
| $\eta$            | = | efficiency                            |
| $\delta$          | = | boundary layer thickness              |
| $\delta^*$        | = | displacement boundary layer thickness |
| $\rho$            | = | density [ $kg/m^3$ ]                  |
| $\omega$          | = | angular velocity [ $rad/s$ ]          |
| $\Pi$             | = | pressure ratio                        |
| $\Delta$          | = | difference                            |
| $( )^*$           | = | nozzle throat                         |
| $( )_m$           | = | motive, or primary                    |
| $( )_s$           | = | secondary, or suction                 |
| $( )_d$           | = | discharge                             |
| $( )_e$           | = | exit                                  |
| $( )_i$           | = | inlet                                 |
| $( )_{cc}$        | = | combining cone                        |
| $( )_{dc}$        | = | delivery cone                         |
| $( )_t$           | = | total                                 |
| $( )_{eff}$       | = | effective                             |
| $( )_{isen}$      | = | isentropic                            |
| $( )_{amb}$       | = | ambient                               |
| $( )_{drag}$      | = | drag                                  |
| $( )_{thrust}$    | = | thrust                                |
| $( )_{laminar}$   | = | laminar flow regime                   |
| $( )_{turbulent}$ | = | turbulent flow regime                 |
| MEMS              | = | Micro- electro- mechanical system     |
| EDM               | = | Electrical discharge machining        |
| RPM               | = | Revolutions per minute                |
| SEM               | = | Scanning electron microscope          |

# Acknowledgements

This would not have been possible without the encouragement, guidance and support of my friends and labmates, my committee, my professors, my family, my wife and my advisor, Professor Jonathan Protz. Their efforts have forever changed me in ways I cannot currently fully perceive and have helped me to discover myself and move towards being the man I want to be. I will forever be unable to have the same impact on those who mentored me, and I will thus spend the rest of my days in effort to pay this gift forward to the next generation.

I would also like to express tremendous gratitude to the United States of America for providing me with the opportunity to pursue this degree and respectfully extend my deepest thanks to all of the men and women who have sacrificed to make this possible.

William Geoffrey Gardner  
*Durham, North Carolina*

# 1

## Introduction

This chapter provides a brief background on the motivation behind efforts to miniaturize power generation and propulsions systems and the accompanying engineering challenges. It then provides a brief description of the Power MEMS (microelectromechanical systems) field and motivates the use of microscale jet pumps in Power MEMS applications. Finally, it provides a brief overview on the birth and development of jet pumps in the 1800's and the role they played in the Industrial Revolution.

### 1.1 Motivation

#### *1.1.1 Microengines*

Since the mid-1990s there has been an active effort to develop hydrocarbon-fueled power generation and propulsion systems on the scale of centimeters or smaller [1–27]. High energy density portable systems will enable both new technologies and improved performance in existing systems. High power density devices, such as micro heat engines, enable designers to package the power plant and fuel required to meet system requirements with minimal volume, allowing more fuel volume and greater energy density. In principle any thermodynamic cycle implemented at the

macroscale could be miniaturized, whether it be the steady flow Brayton or Rankine cycles, or unsteady flow engines using a Diesel, Otto or Stirling cycle. However, “the Brayton power cycle (gas turbine) is superior based on considerations of power density, simplicity of fabrication, ease of initial demonstration, ultimate efficiency, and thermal anisotropy” [16]. Reference [25] provides a detailed overview of these efforts.

### 1.1.2 Energy storage and conversion

Although energy can be stored in many ways (chemical, mechanical, potential, nuclear), chemical energy densities far exceed any other current storage methods, excluding nuclear [25], as shown in Figure 1.1 (p.2).

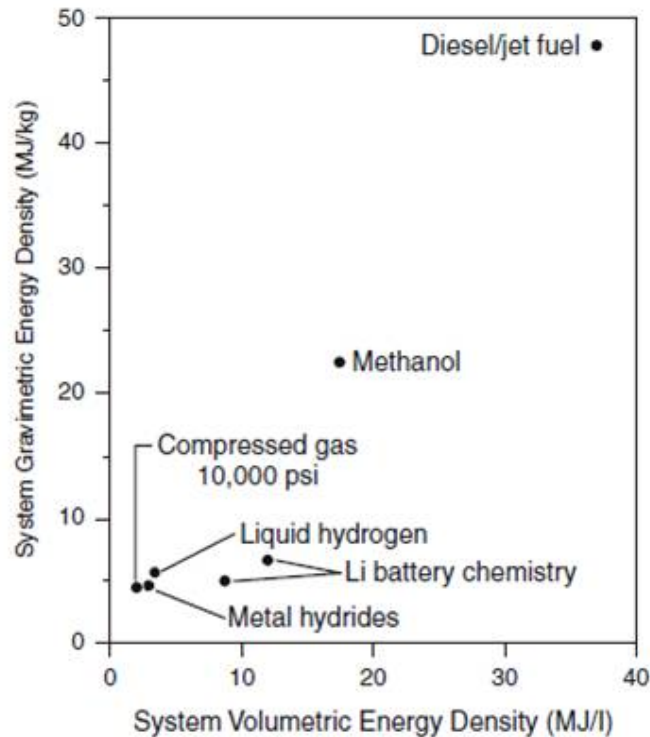


FIGURE 1.1: Energy densities of some common fuels [25]

For this reason, we see automobiles, aircraft and ships operating exclusively on chemical fuels, and in the particular case when either range or weight constraints play a dominant role in design, we see the heat engine implemented as the transferor of chemical potential into work. We should note the exception, however, of large nuclear powered ships and submarines, where the volume of chemical fuel required for satisfactory range given large vehicle mass would occupy too great of a volume to be practical, which has led designers to instead implement nuclear power systems. Nuclear fuels have the highest known energy densities, for example, 1 kilogram of uranium fission releases energy equivalent to burning about 3,000,000 kilograms of coal [28]. However, the equipment required to convert nuclear energy safely into power requires great volume and mass, which limits its current practical use to stationary facilities or ships. Nuclear systems have been explored in applications where no other effective methods of energy storage exist that allow extreme range and endurance, such as deep space exploration [28], and future investigation of such systems may allow eventual miniaturization in the distant future.

Chemically fueled systems currently possess the highest known energy densities, excluding nuclear [25], as shown in Figure 1.2 (p.4). Figure 1.3 provides system energy densities for devices with smaller conversion efficiencies.

## 1.2 Scaling Laws

For many typical Power MEMS devices, power density increases with a decreasing characteristic length scale until losses due to scale effects become overwhelming and prevent intended device operation. This section provides brief description of a few scaling laws of interest.

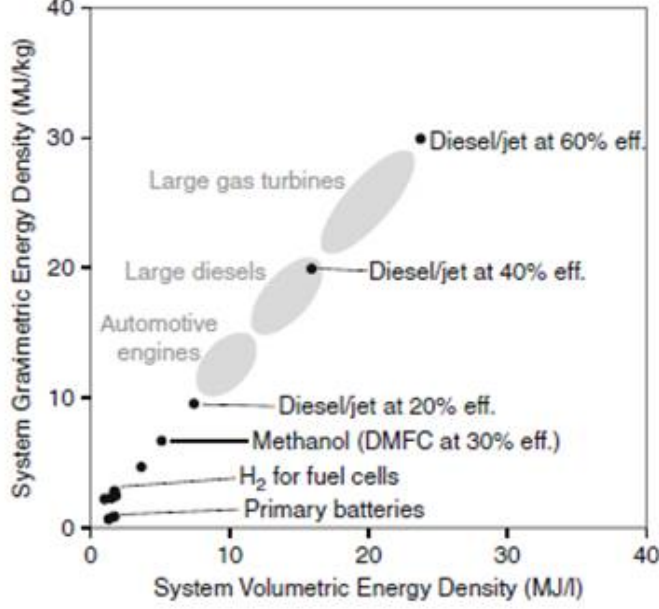


FIGURE 1.2: System energy densities for various fuels and conversion means [25]

### 1.2.1 Cube-square law

In the absence of scale effects, the power output of a gas turbine engine scales with length squared,  $\dot{W}_t \propto L^2$ , and the volume scales with length cubed,  $V \propto L^3$ . Thus, the power density scales with the inverse of length, resulting in increasing power densities as device size decreases. For example, the power output from a turbine,  $\dot{W}_t$ , is given by

$$\dot{W}_t = \eta_t \dot{m} c_p T_{t,4} \left(1 - \Pi_t^{\gamma-1/\gamma}\right) \quad (1.1)$$

where  $\eta_t$  is the turbine isentropic efficiency,  $\dot{m}$  is the mass flow through the turbine,  $c_p$  is the constant pressure specific heat of the exhaust gas,  $T_{t,4}$  is the exhaust gas total temperature, 4 denotes the flow station at the turbine inlet (the numbered flow station convention is commonly used in turbomachinery analysis and appears in Kerrebrock [29] and Mattingly [30]),  $\Pi_t$  represents exit-to-inlet turbine total pressure

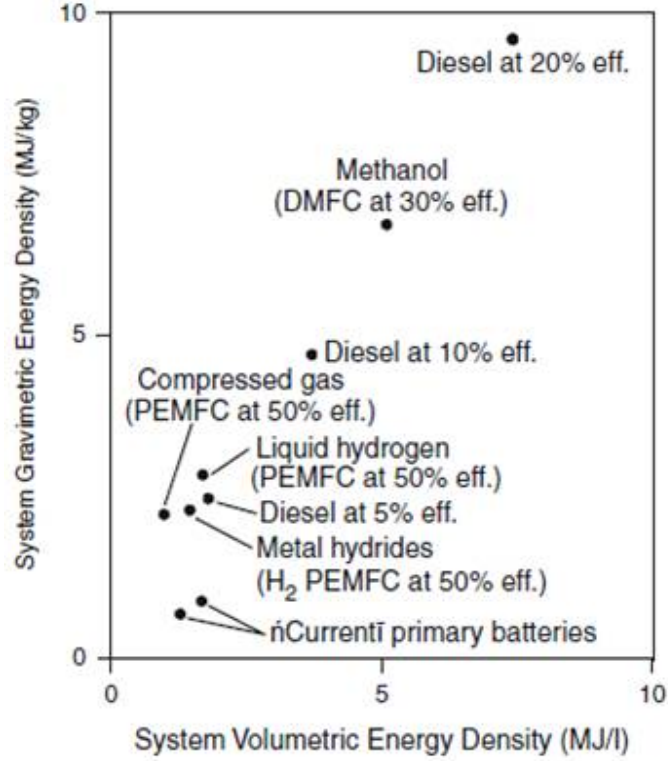


FIGURE 1.3: System energy densities for various fuels and conversion means [25]

ratio, and finally  $\gamma$  is the ratio of specific heats,  $\gamma = c_p/c_v$ , which is typically  $\gamma \approx 1.3$  for hydrocarbon exhaust,  $\gamma \approx 1.4$  for nitrogen and air,  $\gamma \approx 1.3$  for steam and  $\gamma \approx 1.1$  for ethanol vapor.

From the conservation of mass,

$$\dot{m} = \rho u A \propto L^2 \quad (1.2)$$

where  $\rho$  is the fluid density,  $u$  represents the core or average axial velocity,  $A$  represents the flow area and  $L$  is an arbitrary length scale, such as an intake diameter.

Since volume scales with length cubed,  $V \propto L^3$ , the power density,  $\dot{W}/V$  scales with the inverse of length scale,

$$\dot{W}/V \propto 1/L \quad (1.3)$$

### 1.2.2 Scale effects

As length scale or Reynolds number, decreases, losses due to scale effects become increasingly significant and at some point impede intended device operation [2, 3, 6, 8, 22, 31–33]. Above this lower limit, these losses manifest in the form of reduced component efficiencies.

#### Scaling laws

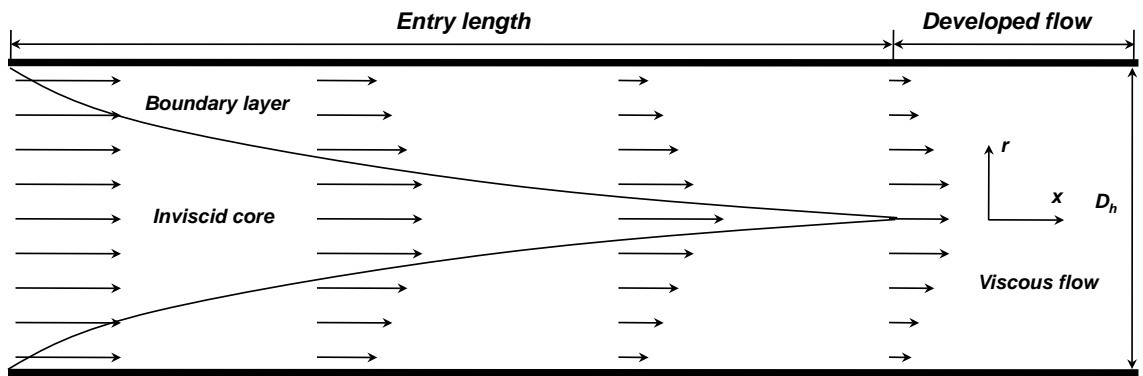


FIGURE 1.4: Illustration of hydrodynamic entry length. The flow becomes developed when the skin friction coefficient,  $C_f$ , is within 2% of its fully-developed value.

Figure 1.4 (p.6) illustrates boundary layer growth for the case of internal flow. Once the boundary layers merge, the inviscid core disappears, and the flow becomes developed and the axial velocity varies in the radial direction. The hydrodynamic entry length,  $L_h$ , is typically taken to be the point where the non-dimensional wall drag or skin friction coefficient,  $C_f$  (the subscript  $f$  denotes 'friction' whereas  $F$  denotes force due to thrust in the thrust coefficient  $C_F$ ), is within 2% of its fully developed value [34]. The skin friction coefficient can be generally expressed in terms of Reynolds number as

$$C_f = C \text{Re}_{D_h}^{-m} \left( \frac{L}{D_h} \right)^{-n} \quad (1.4)$$

where  $C$ ,  $m$ , and  $n$  are constants whose values depend on flow regime and appear below in Table 1.1 [34, 35].

Table 1.1: Skin friction flow regime constants

| <i>Skin Friction</i> | $C$   | $m$ | $n$ |
|----------------------|-------|-----|-----|
| Turbulent            | 0.046 | 1/5 | 0   |
| Laminar entry        | 3.72  | 2/3 | 1/3 |
| Laminar developed    | 16    | 1   | 0   |

The required length-to-diameter ratio,  $L/D_H$ , for fully-developed flow varies with Reynolds number, as seen in equation 1.5 [34]. Typically, conventionally sized rocket nozzles and turbomachines operate with length-to-diameter ratios below the development length-to-diameter ratio for a given Reynolds number, avoiding losses incurred from fully-developed viscous flow. Flows are modeled as streamtubes with an average inviscid axial core velocity [29, 30, 36]. However, at the microscale, these rockets and turbomachines have much smaller Reynolds numbers, making them susceptible to viscous fully-developed flow and a commensurate decrease in performance. Figure 1.5 (p.9) plots hydrodynamic development  $L/D$  versus Reynolds number using a laminar to turbulent transition Reynolds number of 4,000.

$$\left( \frac{L}{D_h} \right)_H = C \text{Re}_{D_h}^{-m} \quad (1.5)$$

Table 1.2: Hydrodynamic development length flow regime constants

| <i>Entry Length</i> | $C$   | $m$ |
|---------------------|-------|-----|
| Turbulent           | 1.359 | 1/4 |
| Laminar             | 0.05  | 1   |

Boundary layer thickness,  $\delta$ , is also a function of Reynolds number, as seen in Figure 1.5 (p.9). Boundary layer thickness can be generally expressed in terms of Reynolds number as

$$\left(\frac{\delta}{L}\right) = CRe_{D_h}^{-m} \left(\frac{L}{D_h}\right)^{-n} \quad (1.6)$$

Table 1.3: Boundary layer flow regime constants

| <i>Boundary Layer</i> | <i>C</i> | <i>m</i> | <i>n</i> |
|-----------------------|----------|----------|----------|
| Turbulent             | 0.037    | 1/5      | 1/5      |
| Laminar               | 5        | 1/2      | 1/2      |

Boundary layer displacement thickness,  $\delta^*$ , quantifies the flow area blockage from boundary layer growth. Displacement thickness is approximately equal to a certain fraction of the general boundary layer thickness,  $\delta$ , based on flow regime. Greitzer recommends use of the following values [37]

$$\begin{aligned} \delta_{turbulent}^* &= \delta/8 \\ \delta_{laminar}^* &= \delta/3 \end{aligned} \quad (1.7)$$

For flow geometries with circular cross-sectional areas, the effective flow area,  $A_{eff}$ , can be expressed in terms of the displacement thickness,  $\delta^*$ , and the diameter,  $D$ , as

$$A_{eff} = \frac{\pi}{4}D^2 \left[ 1 - \left( 1 - 2\frac{\delta^*}{D} \right)^2 \right] \quad (1.8)$$

The ratio of geometric flow area to effective flow area,  $A/A_{eff}$ , can be approximated using equation 1.8 as

$$\frac{A}{A_{eff}} \approx 1 + 4\frac{\delta^*}{D} \quad (1.9)$$

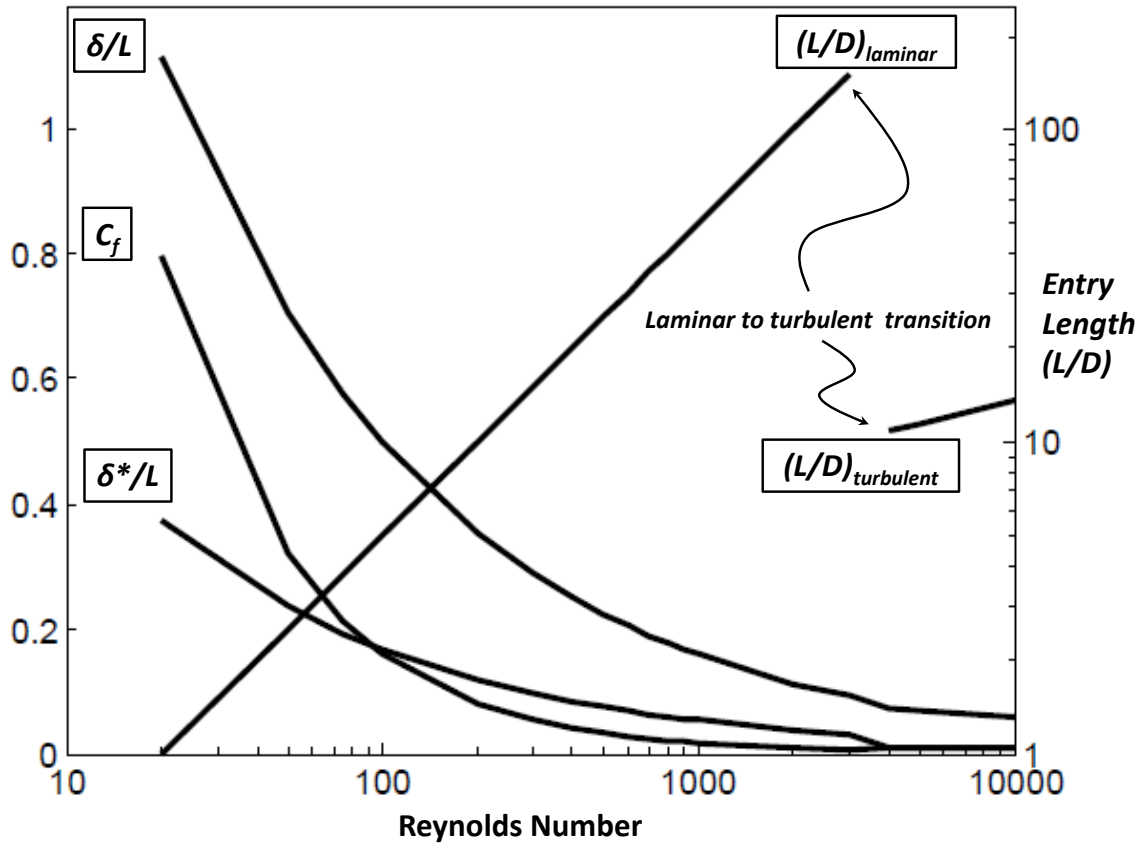


FIGURE 1.5: Boundary layer thickness, skin friction coefficient and hydrodynamic development length across Reynolds number.

At low Reynolds numbers and length scales, boundary layer thickness can become significant and displace flow area. Figure 1.6 (p.10) plots blockage due to boundary layer growth versus Reynolds number for different non-dimensional lengths, where a non-dimensional effective area of 1 indicates no blockage from displacement thickness. The effective flow area values indicate that, for shorter length-to-diameter ratios, the flow cannot develop into fully viscous flow. However, the hydrodynamic length-to-diameter ratio required decreases with Reynolds number, so even relatively shorter length-to-diameter ratios suffer from developed flow at comparatively lower Reynolds.

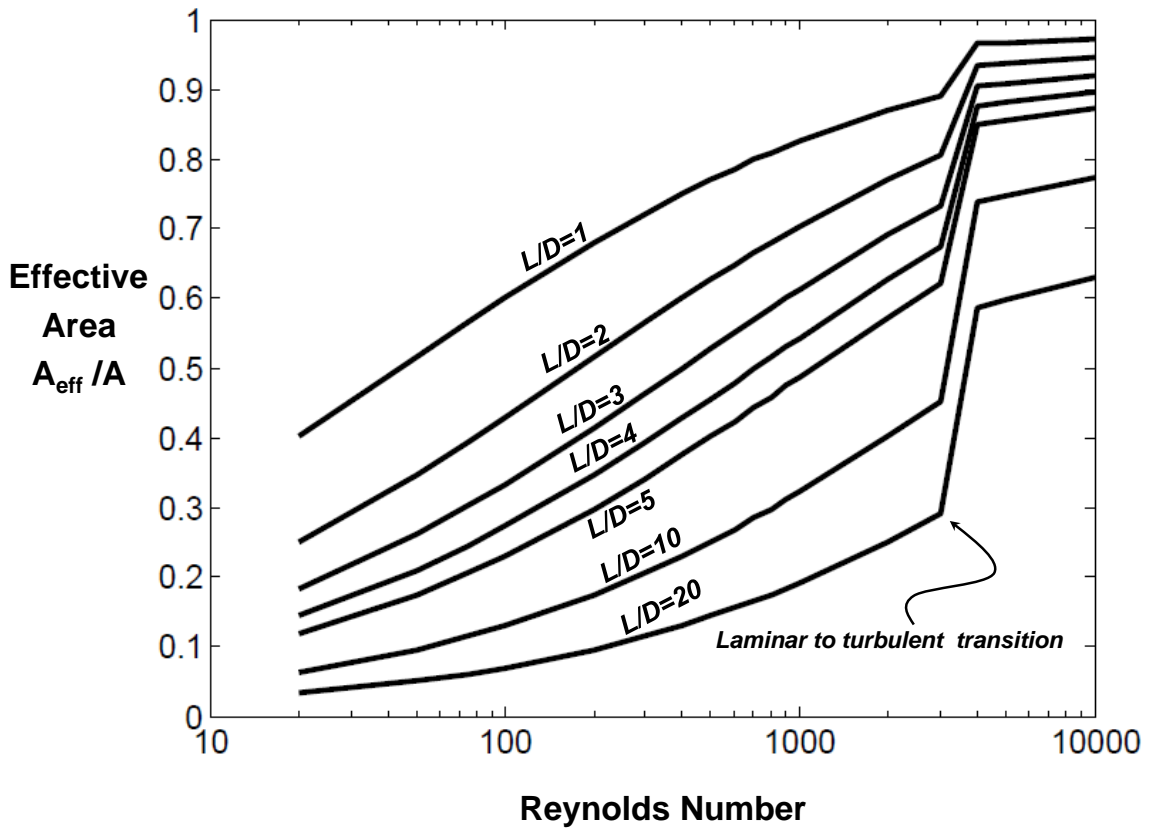


FIGURE 1.6: Effective flow area versus Reynolds number for various length-to-diameter ratios ( $L/D$ ). Flow displacement from boundary layer blockage becomes significant at low Reynolds numbers

Although scale effects manifest in different forms, such as wall drag and displaced flow area, these effects all result from the presence of boundary layers and are the consequence of the effective no-slip boundary condition at the wall.

### 1.2.3 Scale effects in microrockets

Characterization of microscale supersonic nozzles for micro propulsion systems began in the mid-1990's when investigators tested two-dimensional (2-D) supersonic micronozzles fabricated in silicon using deep-reactive-ion-etching (DRIE) with throat

diameters near  $30\mu m$ . Sonic flow was confirmed around 1997 for the 2-D micronozzles etched in silicon and sandwiched between two glass plates [2]. The thrust coefficient,  $C_F$ , which is a typical metric for nozzle performance, represents the actual thrust divided by the ideal thrust produced by expanding gases through a rocket nozzle

$$\begin{aligned}
 C_F &= \frac{F_{thrust}}{P_t A^*} \\
 &= \frac{\dot{m} u_{e,isen} - (P_{amb} - P_e) A_e - F_{drag}}{P_t A^*}
 \end{aligned}
 \tag{1.10}$$

where  $F_{thrust}$  represents the actual thrust,  $P_t$  is throat total pressure, or combustion chamber pressure,  $A^*$  is the nozzle throat area, or the minimum area where choked flow occurs,  $\dot{m}$  is the mass flow,  $u_{e,isen}$  is the isentropic velocity at the nozzle exit,  $P_{amb}$  is the ambient static pressure at the nozzle exit plane,  $P_e$  is the exhaust flow static pressure at the exit plane of the nozzle,  $A_e$  is the nozzle exit area, and  $F_{drag}$  represents the nozzle wall drag resulting from the no-slip boundary condition at the surface of the nozzle walls. For conventionally-sized rocket nozzles,  $C_F$  is typically between 1.4-2 [36]. Early experimental results for a  $37.5\mu m$  micronozzle, shown below in Figure 1.8 (p.13), reported thrust coefficients ranging from  $C_F \approx 0.4 - 1.4$  at Reynolds numbers near  $10^2 - 10^3$ , respectively. This reduction in performance stems from the onset of scale effects experienced at low Reynolds numbers, as typical nozzles with Reynolds numbers near or above  $10^5$  typically experience a 1% reduction in thrust due to boundary layer losses [36]. Figure 1.7 (p.12) provides pictures comparing the sizes of a microrocket [9] and a Saturn V rocket.

Follow-on work began to experimentally investigate losses in micronozzles at low Reynolds numbers [3]. Figure 1.10 (p.15) plots measured thrust efficiency for a  $37.5\mu m$  throat nozzle [3]. The steep decrease in thrust efficiency results from boundary layer growth at low Reynolds number, especially near the nozzle exit where



FIGURE 1.7: Size comparison between a microrocket [9] and a Saturn V rocket

boundary layers will be thickest and may even merge, producing viscous fully-developed flow [3]. Figure 1.9 (p.14) plots model results for a  $37.5\mu m$  throat nozzle with a 16.9 : 1 expansion ratio. The operating conditions and nozzle geometry are taken from Reference [8]. The model used to generate this plot uses the methods presented in this dissertation in effort to capture the physics associated with losses experienced at low Reynolds numbers. These methods allow prediction of device performance for both on- and off-design scenarios with minimal computational effort in comparison to approaches which simulate device performance using computational fluid dynamics.

Figure 1.11 (p.16) compares boundary layer growth in a nozzle for Reynolds numbers near  $10^2$  and  $10^3$ . Boundary layer thickness is typically on the order of  $10^0\mu m$  at the nozzle throat and increases to  $10^1\mu m$  for Reynolds numbers between  $10^2$  and  $10^3$ . In the nozzle exit region, it is possible for the boundary layers to grow and merge, resulting in fully-developed, viscous flow and a commensurate plummert

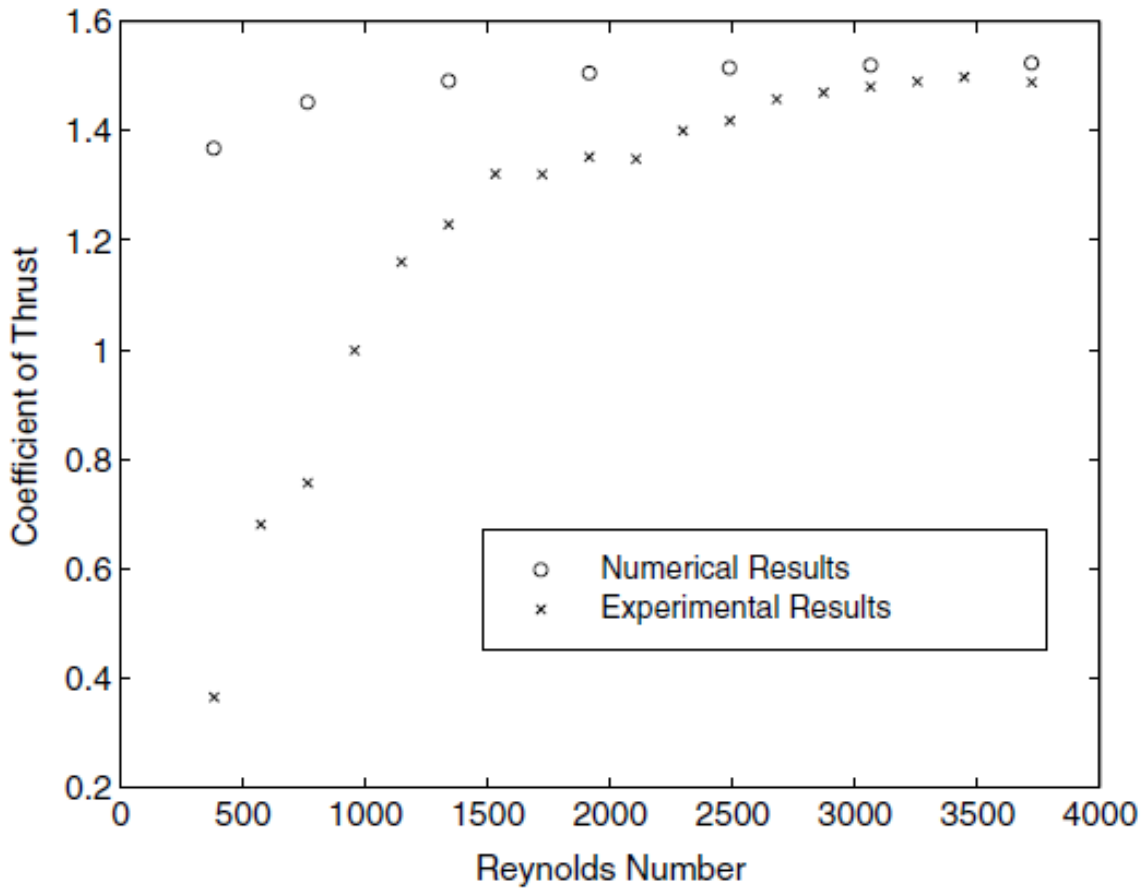


FIGURE 1.8: Thrust coefficient versus Reynolds number for a  $37.5\mu m$  nozzle, from [8]

in performance [3].

#### 1.2.4 Scale effects in microturbomachinery

Computational and analytic investigations have been performed with low Reynolds number turbomachinery [6, 22, 32, 33], where scale effects manifest as decreased component efficiencies. Work in this area to date has been mostly computationally or analytically driven as the instrumentation for performing fluid flow analysis in microscale turbomachinery requires tremendous effort to create [16]. Low Reynolds

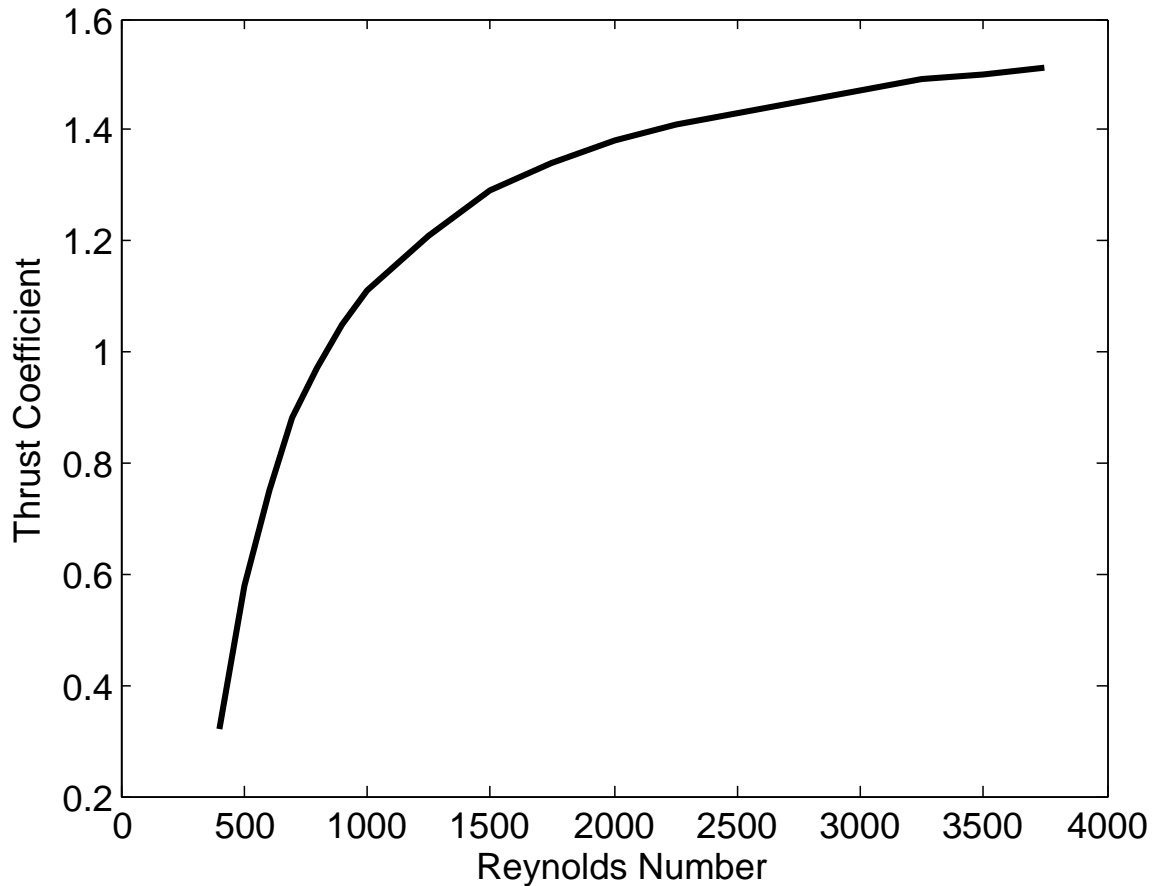


FIGURE 1.9: Model results for thrust coefficient versus Reynolds number for a  $37.5\mu m$  nozzle with a 16.9:1 expansion ratio. The model predicts micronozzle performance using the methods presented in this dissertation and shows good agreement with experimental data from Reference [8].

number losses in turbomachines are often compounded with additional fluid dynamic losses such as diffuser separation or inadequate diffusion of high-velocity flow. These fluid dynamic losses result in part due to the challenges associated with using existing microfabrication techniques to implement features commonly employed at the macroscale which minimize diffuser losses, some of which include the twisting of airfoils, variation of blade heights and aspirating compressors [16]. Additionally, the

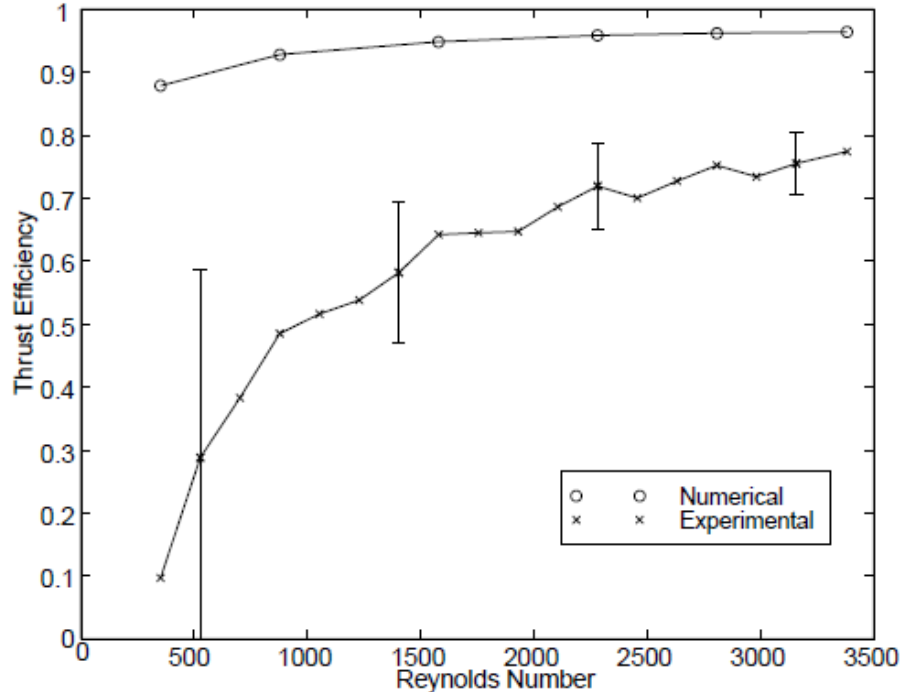


FIGURE 1.10: Thrust efficiency for a  $37.5\mu m$  throat nozzle [3]

relatively thick trailing edges resulting from current MEMS fabrication techniques produce airfoils which have trailing edge thicknesses of similar length scale to the rotor-to-stator tip clearance, which results in increased drag [16]. The combination of these losses reduces microscale turbomachinery efficiencies with respect to their macroscale counterparts. For example, Figure 1.12 (p.17) maps turbine efficiency across length scale and velocity ratio. Here we see that a  $10mm$  turbine at  $10^6$  RPM operates with approximately 60% efficiency with a nearly matched ( $\approx 1$ ) velocity ratio, whereas a  $1m$  diameter turbine easily achieves 80% efficiency at lower velocity ratios of ( $\approx 0.7$ ) [33]. Table 1.4 (p.16) provides comparison between the turbine diameters, operating speeds and efficiencies for a microengine [9, 15] and a General Electric GE-90 engine. Figure 1.13 (p.18) provides pictures of these two engines.

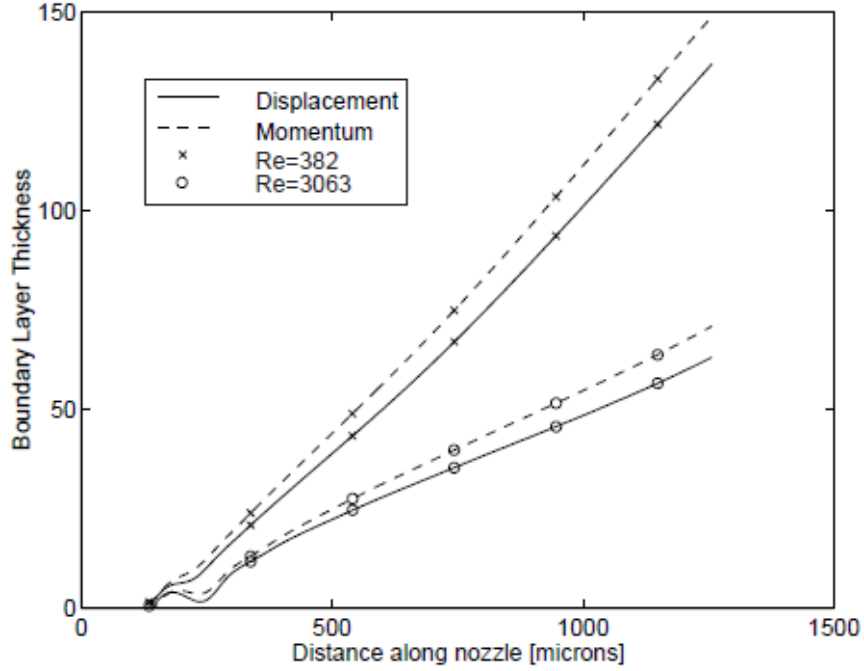


FIGURE 1.11: Boundary layer thickness from the nozzle throat to exit, from [3]

Table 1.4: Size, speed and efficiency comparison between a microturbine [9] and GE-90 turbine

|                   | Microturbine                 | GE-90           |
|-------------------|------------------------------|-----------------|
| Turbine diameter  | $\approx 6 \times 10^{-3} m$ | $\approx 1 m$   |
| Rotor speed (RPM) | $\approx 500,000$            | $\approx 5,000$ |
| Efficiency        | $\approx 60\%$               | $\approx 93\%$  |

### 1.3 Current State of the Art

Figure 1.14 (p.19) provides comparison between microengine energy density and current state-of-the-art battery chemistries. Even at relatively low thermal efficiencies ( $\approx 5\% - 10\%$ ), with respect to macroscale combined cycle power plants ( $\approx 50\%$ ), microscale gas turbine power generators achieve a  $2x - 5x$  multiple in energy density compared to current high-performance lithium-ion batteries with energy densities of 175 W-hr/kg.

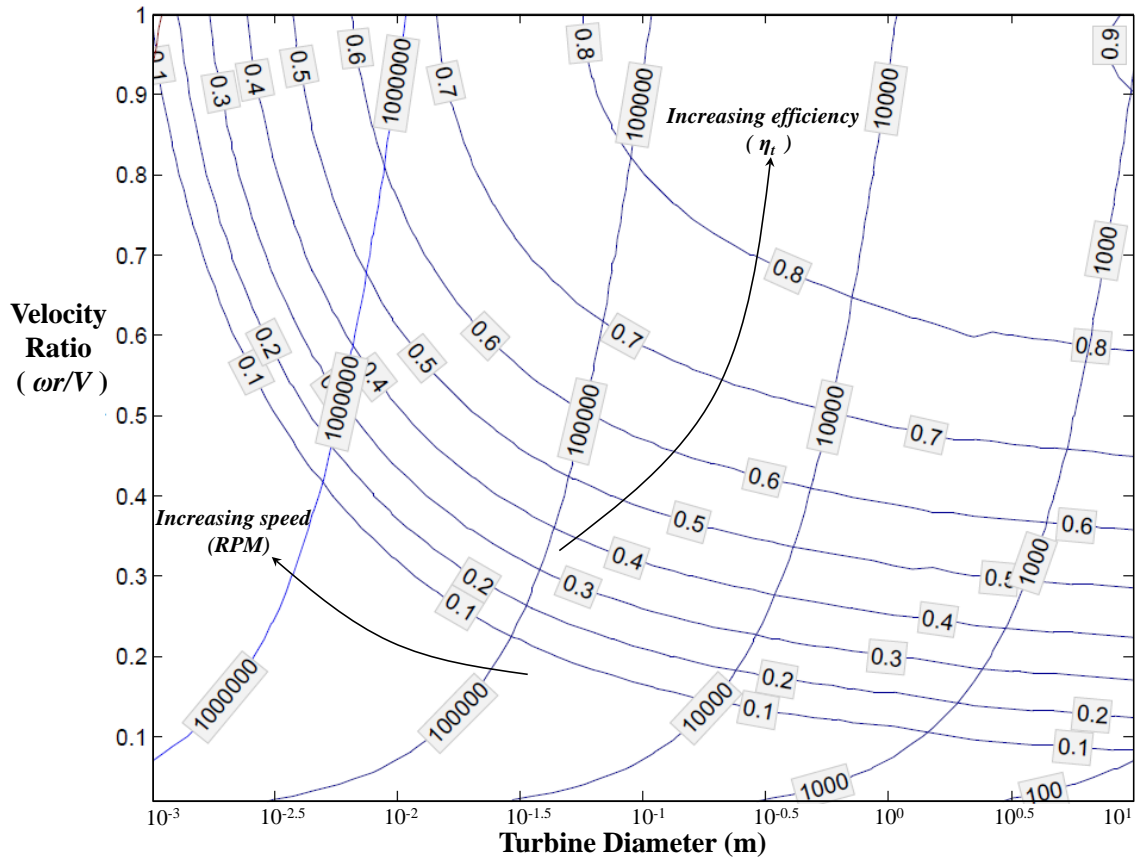


FIGURE 1.12: Turbine efficiency as a function of diameter and velocity ratio, data from [33]

### 1.3.1 Turbomachinery tip-speed requirement

Designers have investigated microscale Brayton cycle (gas turbine) engines which require high-speed compressors and turbines [1, 4, 15, 20, 21, 25, 38], as well as microrockets which require high-speed turbopumps [5, 12, 14, 39]. Both devices involve high-speed turbomachinery which requires high-speed bearings. High-speed operation is desired because high-efficiency turbomachines require high pressure ratios which in turn create a high velocity fluid. In order to accept the high velocity flow efficiently without inducing excessive swirl or losses, the rotor tip speed must ap-

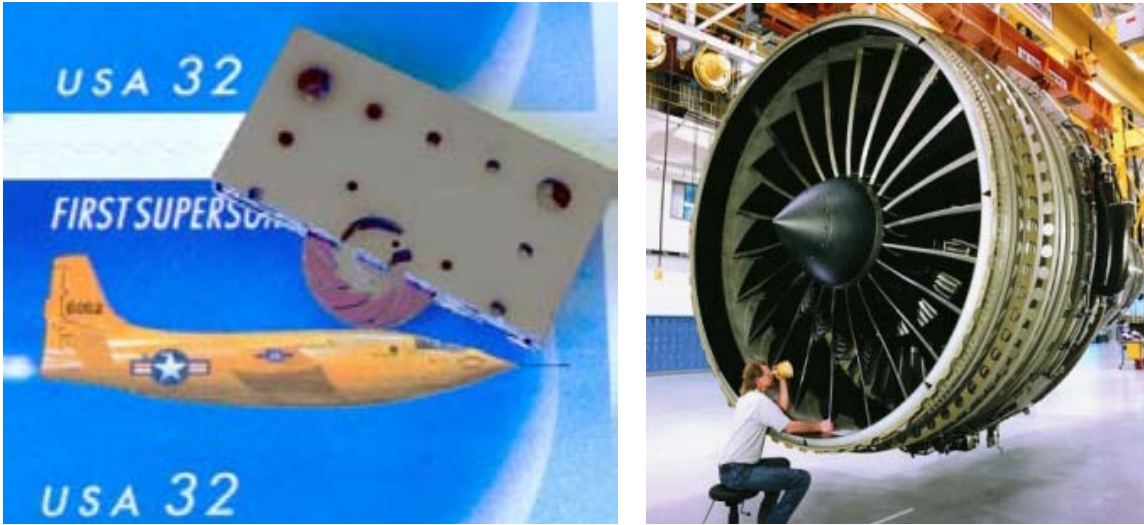


FIGURE 1.13: Size comparison between a microengine [9] and a GE-90 turbofan engine

proach the fluid velocity, which is typically transonic [29, 30]. Thus, turbomachines typical operate with transonic rotor tip speeds near Mach 1 with a velocity ratio near 1, which corresponds to a range typically between 400 - 600 m/s depending on temperature [29, 30, 40]. As length scale decreases, angular velocity increases, requiring high-speeds at the microscale. Figure 1.15 (p.20) gives a few example rotor diameters and RPM at different tip speeds.

### *1.3.2 Limitations of macroscale approaches*

From Figure 1.15 (p.20), we see that the design space exists beyond the speed capabilities of current micro ceramic bearings of roughly 450,000 RPM. In addition to the speed limit, these ball bearings require shafts to mate to the inner bore to allow rotation. This shaft requirement adds an additional burden to the designer with regards to assembly and also is of similar magnitude to the rotor diameter, which increases inertia, material and assembly complexity. The Japanese company NSK

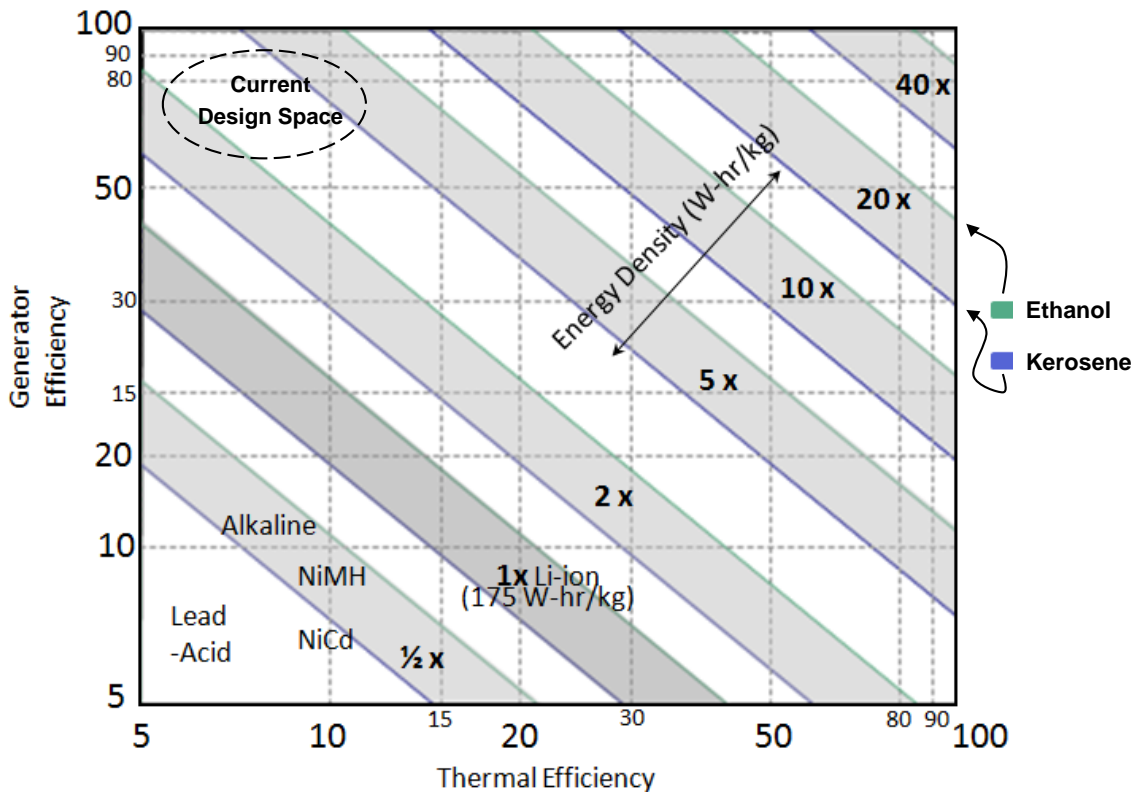


FIGURE 1.14: System energy densities for microengines compared to batteries

Micro Precision, which supplies bearings for high-speed turbine driven dental drills, has produced the world's smallest ball bearing, with an outer diameter of 2mm and a shaft diameter of 0.6 mm, shown in Figure 1.16(a) (p.21). In addition to radial loads, bearing systems for a turbomachine also require the ability to resist the thrust forces created by the unequal pressures on the upstream and downstream faces of the rotor. Angular contact bearings in pairs could satisfy this requirement if the design speed were satisfactory. Used in some timepieces, a low-friction jeweled bearing assembly, such as the one shown in Figure 1.16(b) (p.21), can support radial and thrust loads. Some options involve ruby or sapphire thrust pad endstones and journals, which are durable and feature a coefficient of friction of 0.15 with steel (teflon is roughly

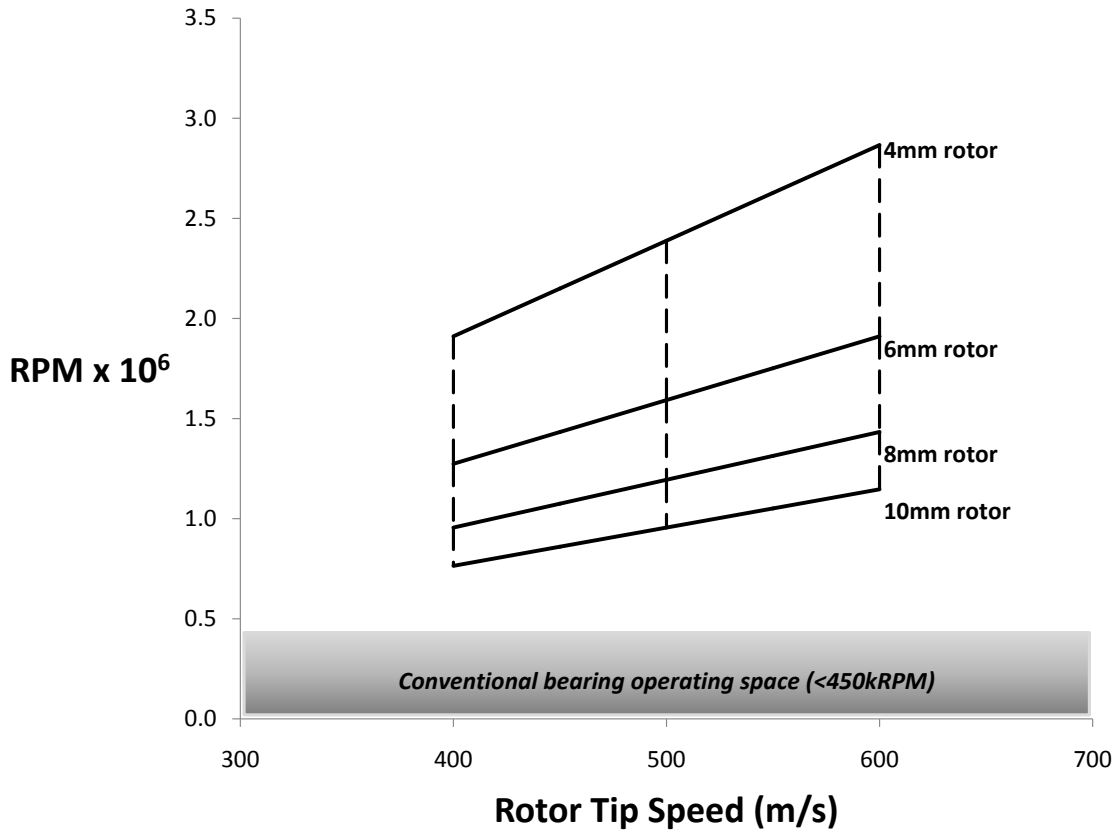


FIGURE 1.15: RPM as a function of rotor tip speed

0.04). However, design speeds for these systems are typically limited to 10,000 RPM. These systems also impose a shaft requirement. Ball bearing and jeweled bearing systems also typically occupy similar or greater volumes than the turbomachinery subassemblies themselves in microengines.

### 1.3.3 Gas bearings

The high-speed requirement motivated the development of gas bearings [4, 16, 20, 41, 42]. Due to the limitations of existing mechanical bearings, engineers implemented and developed the theory for microscale gas bearing systems, which were an elegant

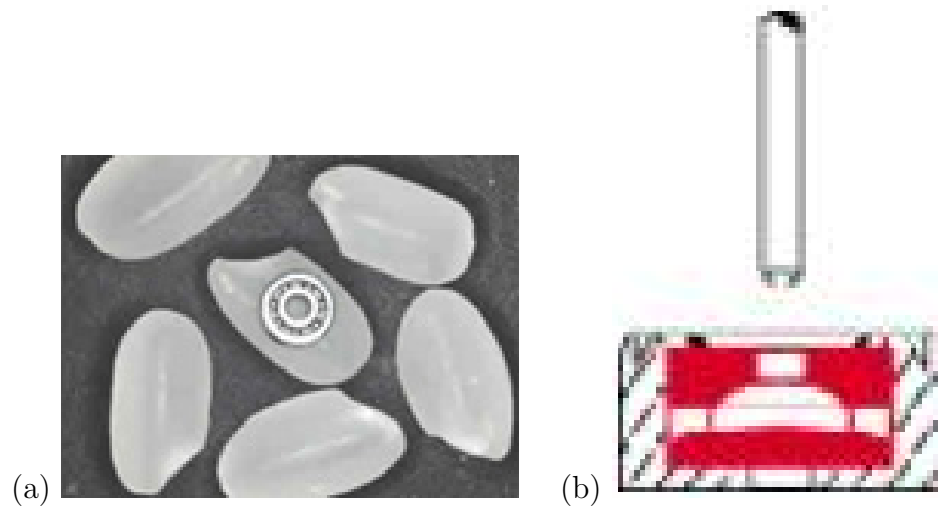


FIGURE 1.16: Examples of miniaturized conventional bearings. (a) NSK Micro Precision's micro ball bearing and rice grains (image courtesy of NSK), and (b) schematic of a jeweled thrust bearing assembly (image courtesy of Bird Precision)

solution but require the use of pressurized fluid to both start and sustain operation. The pressurized fluid first floats the rotor, and during operation supplies a small jet discharging onto thrust pad of the rotor to create axial thrust. Dynamic loading, typically resulting from rotor imbalance during steady state operation, is compensated by use of hydrodynamic bearings. Investigators have developed both the theory as well as the fabrication recipes to successfully implement silicon high speed gas bearing supported turbomachinery, which feature the highest tolerance requirement in the microengine, typically on the order of a few microns [4, 16, 20, 41, 42]. In addition to preventing tip leakage, high-tolerances are required to minimize rotor imbalance and eccentricity. Eccentricities require a greater gap between the rotor and journal bearing to avoid rotor-stator contact during operation. Figure 1.17 (p.22) shows the configurations and photographs for hydrodynamic and hydrostatic thrust bearings from [16]. The use of high-speed gas bearing systems in microengines is a design requirement for practical engines. This requirement is also evidenced by the use of gas

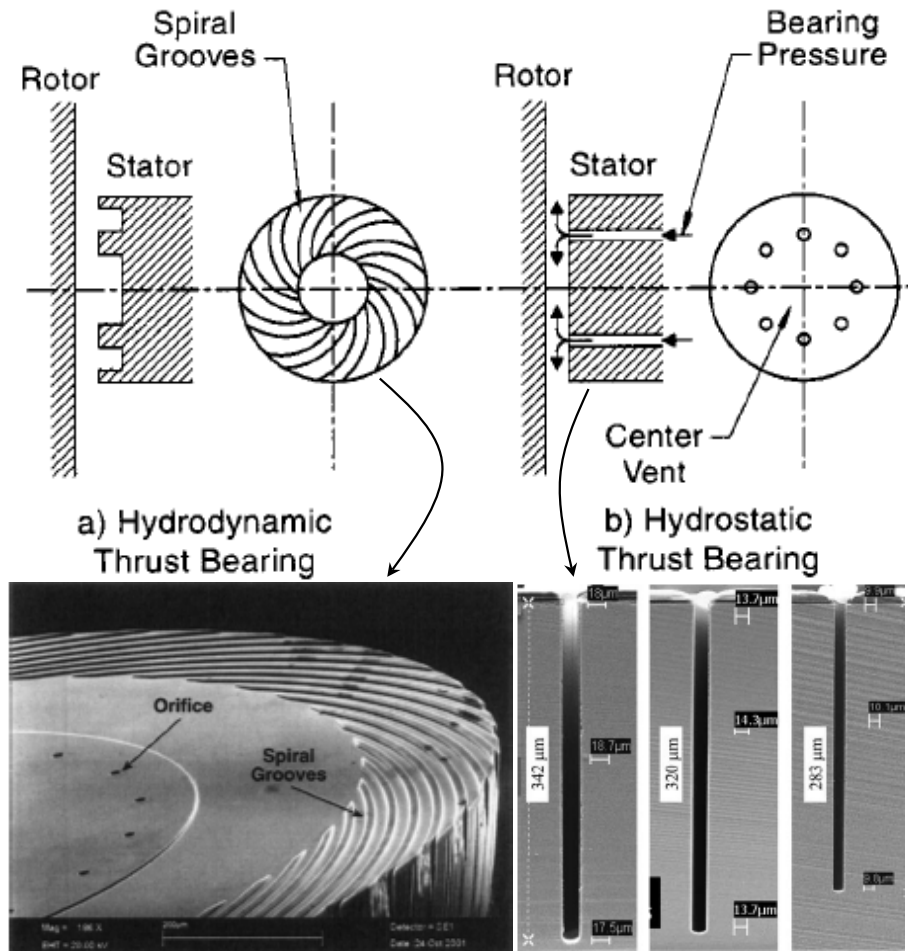


FIGURE 1.17: Hydrodynamic thrust bearings and hydrostatic thrust bearings, images courtesy of [16]

bearings in turbomachinery systems which are comparatively much greater in size but smaller than typical aircraft jet engines, such as the 30 kW Capstone engines.

### 1.3.4 Clearances and tolerances

For microengines, the ratio of clearance to a component length scale, or fabrication tolerance, is typically much larger than a corresponding macroscale device [1, 16, 38]. If large enough, this clearance will permit an excessive mass flow leakage around the

rotor and prevent the cycle from closing since the compressor will be unable to sustain operation. Figure 1.18 (p.23) shows a schematic of tip leakage over a turbomachine blade [33]. During steady-state operation, it is reasonable to have the

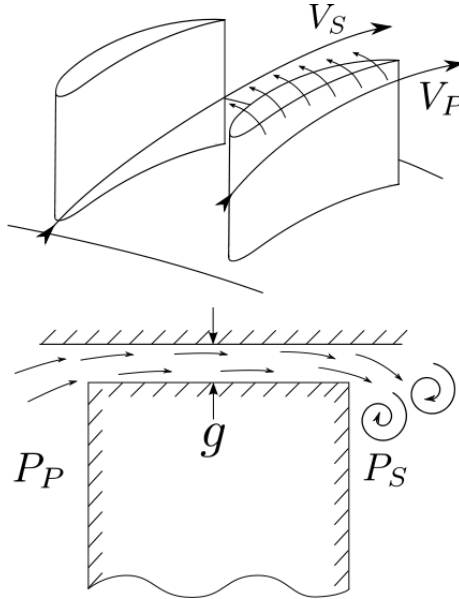


FIGURE 1.18: Schematic of tip leakage over a turbomachine blade, from [33]

compressor bleed adequate mass flow for gas bearing operation while simultaneously providing enough core mass flow to operate and close the cycle. However, the original work required an externally supplied source of pressurized gas for the starting sequence, which can lead to impracticalities when implementing the engine in volume constrained applications, or in scenarios requiring repeated start up sequences [4]. Furthermore, maintenance and refilling the pressurized tank would may create an additional burden if the application prohibits constant refilling of the pressurize tank by the compressor.

## 1.4 Power MEMS

First suggested in 1996, Power MEMS (micro-electro-mechanical systems) originally referred to MEMS fabricated heat engines, specifically those operating on a Brayton cycle [1, 9, 25]. The contemporary definition of Power MEMS encompasses any microfabricated device which generates power or pumps heat [9, 25]. In the words of Professor Carol Livermore, “Power MEMS are MEMS devices that manipulate macroscopically-significant amounts of power in a small package.” Figure 1.19 (p.24) shows a schematic focused on the heat engine within the Power MEMS field.

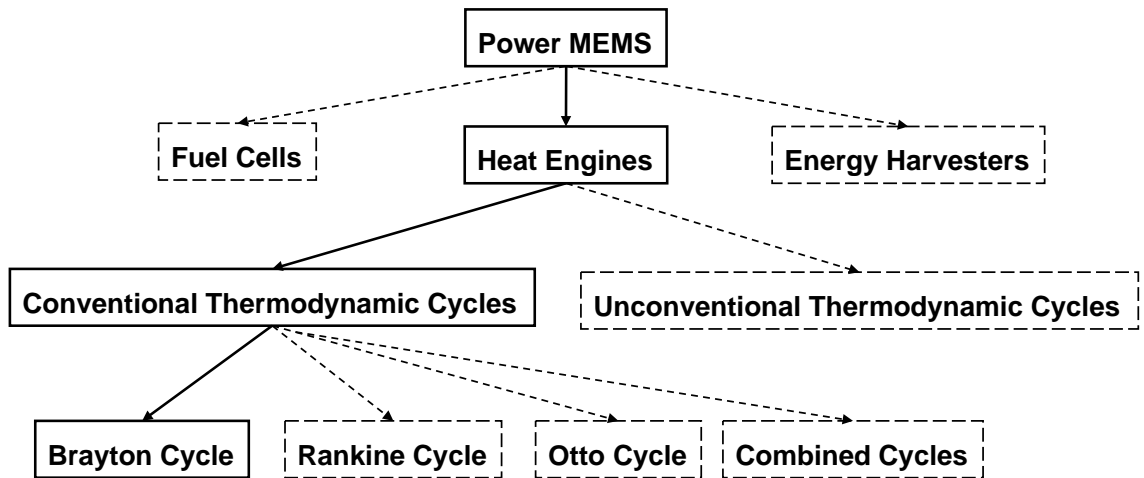


FIGURE 1.19: Schematic of the Power MEMS field

### 1.4.1 Power MEMS applications for jet pumps

Many MEMS devices require the means for pumping fluids at the microscale. Since the 1980's, investigators have explored various methods to satisfy pumping requirements [43–46], some of which include mechanical, electro-osmotic, electrohydrodynamic and magnetohydrodynamic pumps. Non-rotating pumping devices, such as jet ejectors and jet injectors, which are more broadly classed as jet pumps, can serve

as alternatives to pumping turbomachinery or other rotating pumps, supplementing or eliminating some of the high-speed components in microscale turbogenerators and rockets, enabling the fabrication of Power MEMS devices that rely on a reduced number moving parts. Figure 1.20 (p.25) shows a schematic of Power MEMS applications for jet pumps.

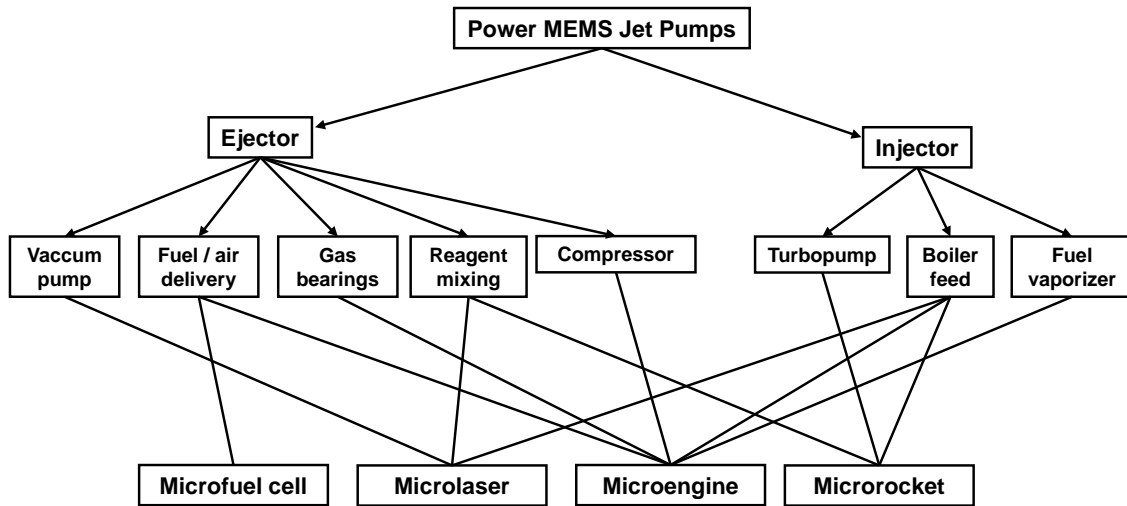


FIGURE 1.20: Schematic of the Power MEMS applications for micro jet pumps

### *Microengines*

For example, ejectors and injectors can be used to implement microscale vapor cycle (Rankine) engines, one example of which is a steam locomotive engine, whose only moving part is a piston [47], as shown below in Figure 1.21 (p.26). In lieu of a piston, a low-speed gas turbine could be used for power offtake, as shown in Figure 1.22 (p.27) [32, 48].

When a Brayton (air) cycle 'tops' a Rankine (vapor) cycle, some useful work can be recovered from the exhaust gas output from the Brayton cycle [29]. Given the

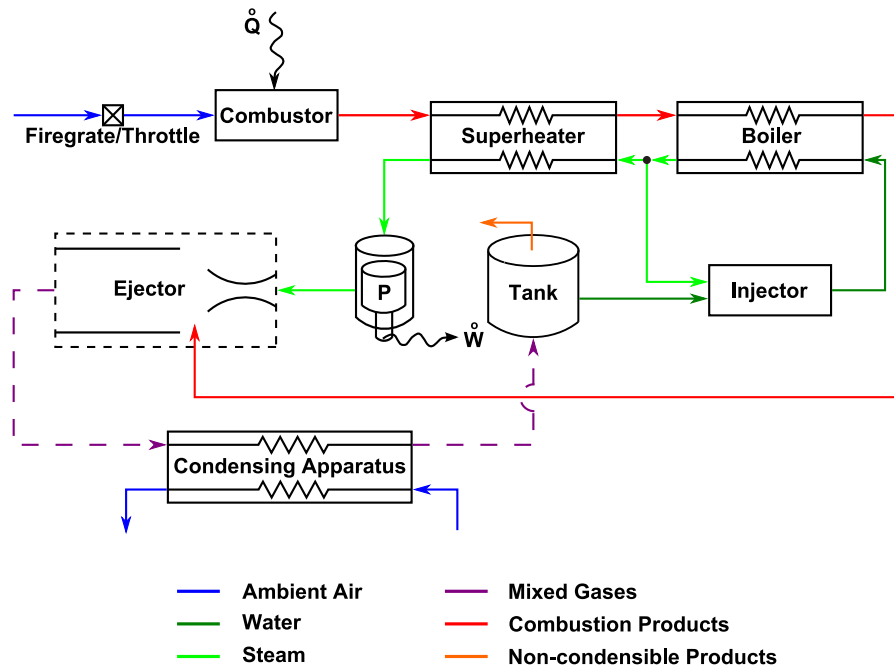


FIGURE 1.21: Conventional steam locomotive cycle schematic

comparatively low thermal efficiencies of microengines, the exhaust gas contains a comparatively large amount of high quality heat [16], making the gains from heat recovery or recuperation relatively significant. Exhaust energy is ultimately transferred to a power turbine, though the intermediate path may vary. Figure 1.23 (p.28) shows a turbocharged vapor cycle in which the exhaust gas directly drives a power turbine and then exhausts through a boiler to generate vapor.

Figure 1.24 (p.29) shows a combined cycle featuring cold turbines with an after-burner combustor in effort to thermally isolate the power turbine.

### *Microrockets*

Jet pumps could also enable a microrocket requiring only a static structure through substitution of turbopumps with jet injectors [49–52]. Figure 1.25 (p.30) shows an expander cycle which uses regenerative heating in the nozzle to generate vapor,

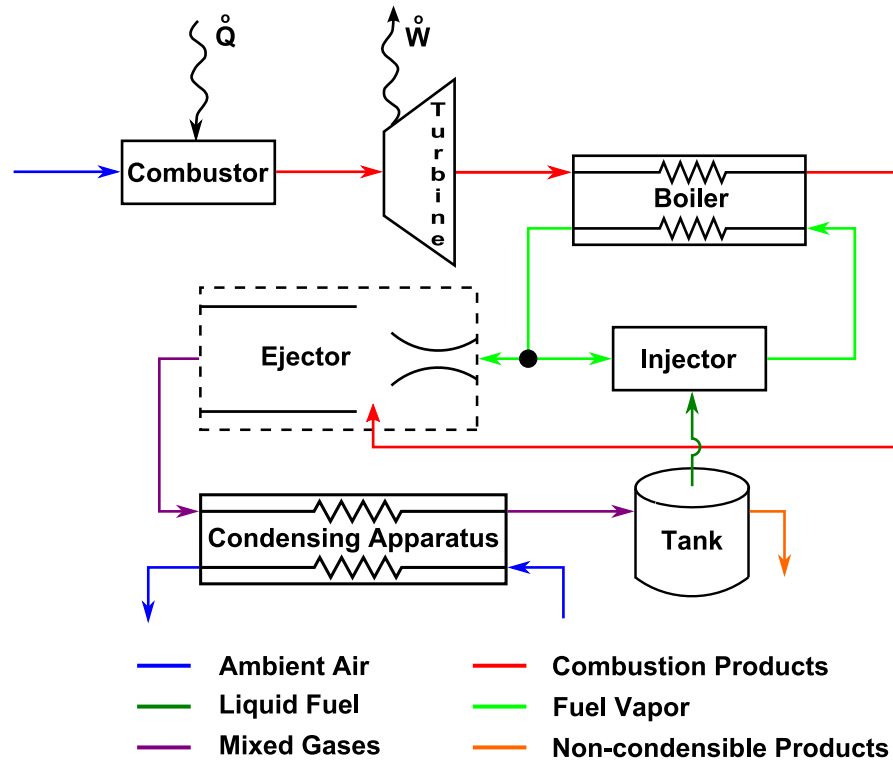


FIGURE 1.22: Schematic of a steam locomotive (Rankine) cycle with a turbine providing power off-take

conventionally used to drive a turbopump, that becomes the motive fluid for an injector which is capable of pumping propellants at or above combustion chamber pressures. In these Power MEMS applications mentioned, the resulting reduction in complexity compared to pumping turbomachinery affords the designer a simple start-up protocol, robust operation, and the flexibility to use microfabrication processes that offer comparatively low tolerances. Other potential applications within the Power MEMS field exist, as shown in Figure 1.20 (p.25), to include some that have been demonstrated [54–60].



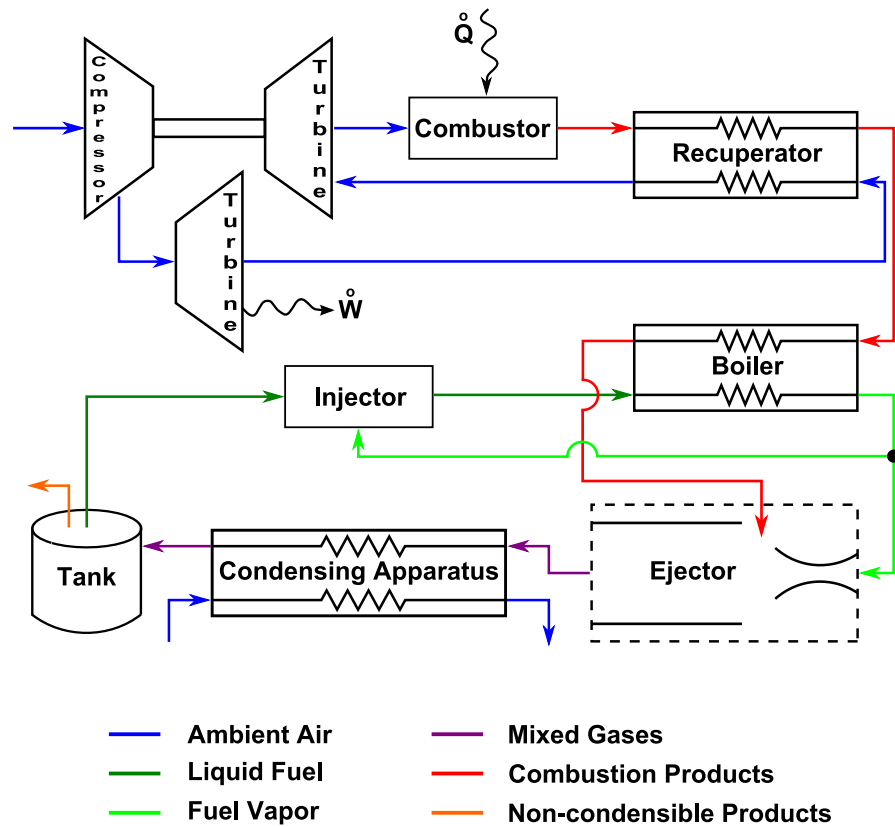


FIGURE 1.24: Schematic of a Brayton cycle topping a steam locomotive (Rankine) cycle with a fluidically coupled power turbine

$$\dot{W} = \dot{m}\Delta P_t/\rho \quad (1.11)$$

where  $\dot{W}$  is the required pump work,  $\dot{m}$  is the pumped mass flow rate,  $\Delta P_t$  represents the change in total pressure of the pumped fluid across the pump inlet to outlet, and  $\rho$  is the fluid density, we can see that consequences of inefficiency will be less pronounced for incompressible fluids simply due to density. Liquids are of order  $10^3 kg/m^3$ , whereas gases are typically of order  $1 kg/m^3$  at typical ambient conditions ( $P \approx 1 atm$ ,  $T \approx 300K$ ). Thus, jet injectors operating in vapor cycles (Rankine or combined cycle engines) or expander cycles (rockets) will incur less penalty from

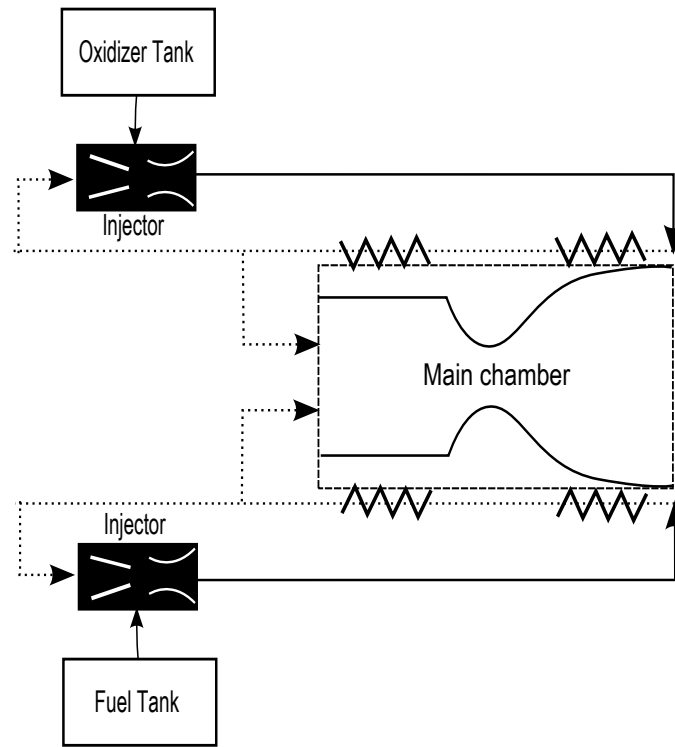


FIGURE 1.25: Schematic of a microrocket bipropellant injector-pumped expander cycle [53],[49]

inefficiency than jet ejectors pumping vapors or gases. In other words, in devices which have the option to pump either the liquid or vapor phase of a substance, it requires less pumping work when delivering a fixed mass flow rate of liquid phase versus vapor or gas phase. For turbomachinery or, more generally, mechanically driven pumps, this effect from density results in a smaller shaft work input to pump a given mass flow rate. For the case of vapor driven jet pumps, this effect from density results in a smaller motive vapor mass flow rate input, or decreased motive total pressure, to pump a fixed mass flow rate.

## 1.5 Jet Pumps: A Brief History

### 1.5.1 Steam locomotives

The core of the steam locomotive engine contains no moving parts; steam injectors pump liquids, and steam ejectors pump gases. Low entrainment steam jet ejectors were first used during the 19th century to induce a draft across the firebox of coal-fired steam locomotives and expel its exhaust out of the stove pipe (diffuser) [47]. The ejector's lack of moving parts affords designers a simple start up protocol, the ability to pump fluids containing particulates, and a reduction of moving parts. Figure 1.26 (p.31) shows a schematic of the flow paths and components in a typical steam locomotive engine.

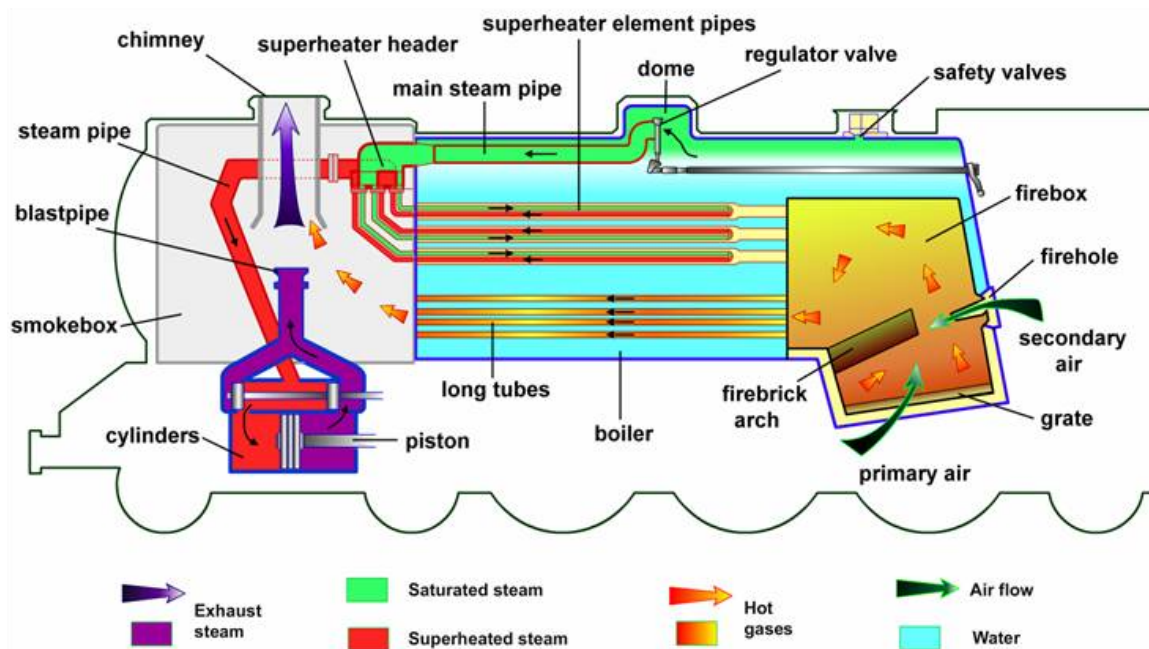


FIGURE 1.26: Typical steam locomotive engine flow paths and schematic

### 1.5.2 *Jet ejectors*

Jet ejectors appeared perhaps by accident in steam locomotives during the 1820's when designers began injecting exhaust steam from the cylinders into the base of the chimney, allegedly to reduce noise to avoid frightening animals such as horses used for transport [47]. The steam jet entrained and pumped additional fluid through the firebox, which in early application was fed solely by natural convection through a chimney. Designers increased the volume in front of the boiler to accommodate the steam jet and to assist the removal of ash which would travel through the boiler firetubes, leading to the name 'smokebox' [47].

Operators noticed that greater steam discharge rates increased draft through the firebox, elevating firebox temperatures and in turn evolving more steam. The process was effectively self-acting. The performance of this ejector depends on the surface area of the motive jet, as well the jet velocity, which is a function of supply pressure. A high supply pressure improves performance but can lead to lower system efficiencies due to reduced conversion of pressure potential energy into useful work by the piston, requiring a balance. Professor and Dean William F.M. Goss at Purdue University carried out the first comprehensive experimentation on the locomotive draft systems around 1891, recommending geometries that were implemented on the Great Western Railway and in the United Kingdom through the 1950's [47, 62–69]. Since locomotives operated over a range of speeds, a variety of throttling systems were implemented to allow control of air flow. Designs evolved into multi-nozzle, multi-stage systems which increased entrainment per a given supply pressure when compared to single-nozzle and single-stage system. One successful version was the Kylchap double exhaust blast pipe, developed and patented by the Finnish engineer, Kylala and the French engineer, Chapelon [47]. These systems were successfully implemented in the UK on the A4 Pacifics in 1936, and then later found greater adoption in the

1950's. Reference [47] provides an overview on historical development efforts of early steam locomotive ejector systems, and Professor Goss's book [62] provides extensive presentation of experimental work performed on many locomotive components and subsystems. Figure 1.27 (p.33) shows a picture of a Lempor blastpipe found in the smoke box of a steam locomotive, and Figures 1.28 (p.34) and 1.29 (p.35) show a picture and drawing of a Kylchap blastpipe, which was a multi-staged version featuring two mixers.



FIGURE 1.27: Lempor nozzle

### *1.5.3 Jet injectors*

In addition to using jet pumps for pumping gases into steam engines, they were also developed for use as a feed-water delivery system by the French engineer and inventor Henri Giffard during the 1850's [70, 71]. Giffard designed and patented his injector (1860, US Patent No. 27,979 [70]) which, when supplied with live steam, expands through a motive nozzle, entraining feed-water, and then condenses into

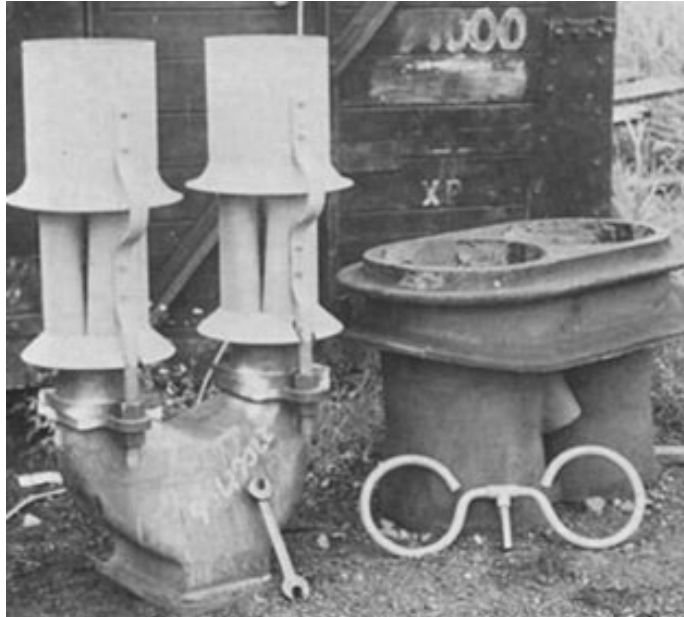


FIGURE 1.28: Picture of a Kylchap blastpipe

the water stream and 'lifts' the water stream up to boiler pressures. Figure 1.30 (p.36) shows Giffard's sketch from his US patent in 1860 [70]. Giffard's injector soon became widely adopted, replacing the mechanical pumps of the era [47]. The injector featured no continuously moving parts and required simple valves to ensure proper operation. Later improvements, such as those featured in the Sellers injector, incorporated venting schemes which allowed the injector to regulate itself, reducing the need for operator input to ensure proper injector operation [71]. Reference [72] provides the first real attempt to describe the theory behind different injector designs that proceeded Giffard's original work, and Reference [71] provides updates on theory and practice circa 1900. Crawford (2003) [73] provides excellent contemporary discussion of steam injectors and provides examples of typical dimensions for miniature hobbyist steam locomotive applications. Figure 1.31 (p.37) displays a cross section of a vented, self-acting injector developed by Penberthy that found fairly wide

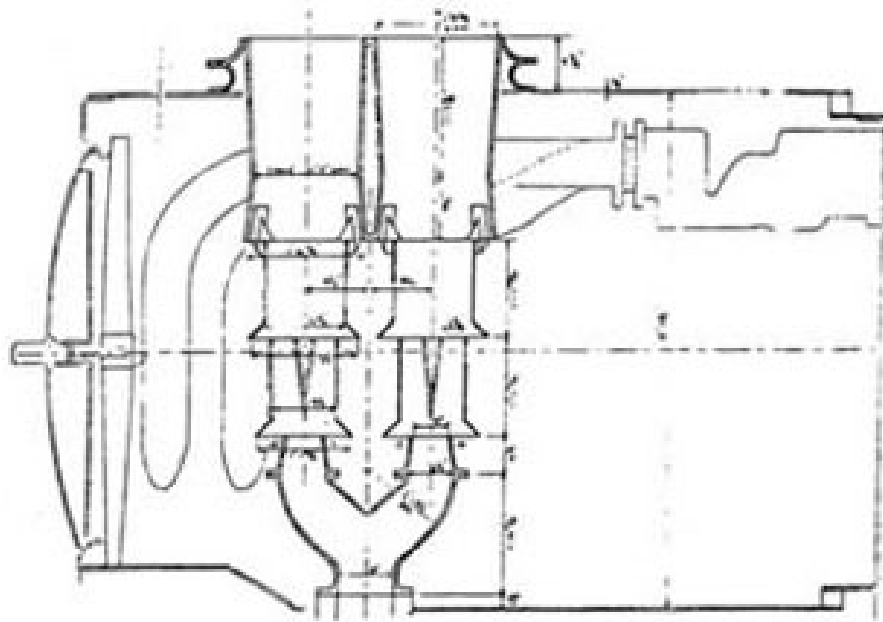


FIGURE 1.29: Drawing of a multi-stage Kylchap blastpipe and chimney

adoption. The venting scheme eliminates the need for manual adjustment.

#### 1.5.4 *Historical perspective*

Based on the historical use of jet pumps in improving the driving force behind the Industrial Revolution, the steam engine, it seems reasonable to conclude that they may be able to assist in the reduction to practice of the microengine or microrocket, which also has great potential to shape the future. The implementation of jet pumps in Power MEMS devices also reflects contemporary microscale manufacturing tolerances as well as macroscale tolerances achievable during the Industrial Revolution. Despite tremendous improvements in microfabrication processes and techniques during the last half-century, microscale manufacturing techniques remain limited when compared to temporary conventional machining capabilities. Manufacturing techniques used during the Industrial Revolution were crude by today's standards. Then, and

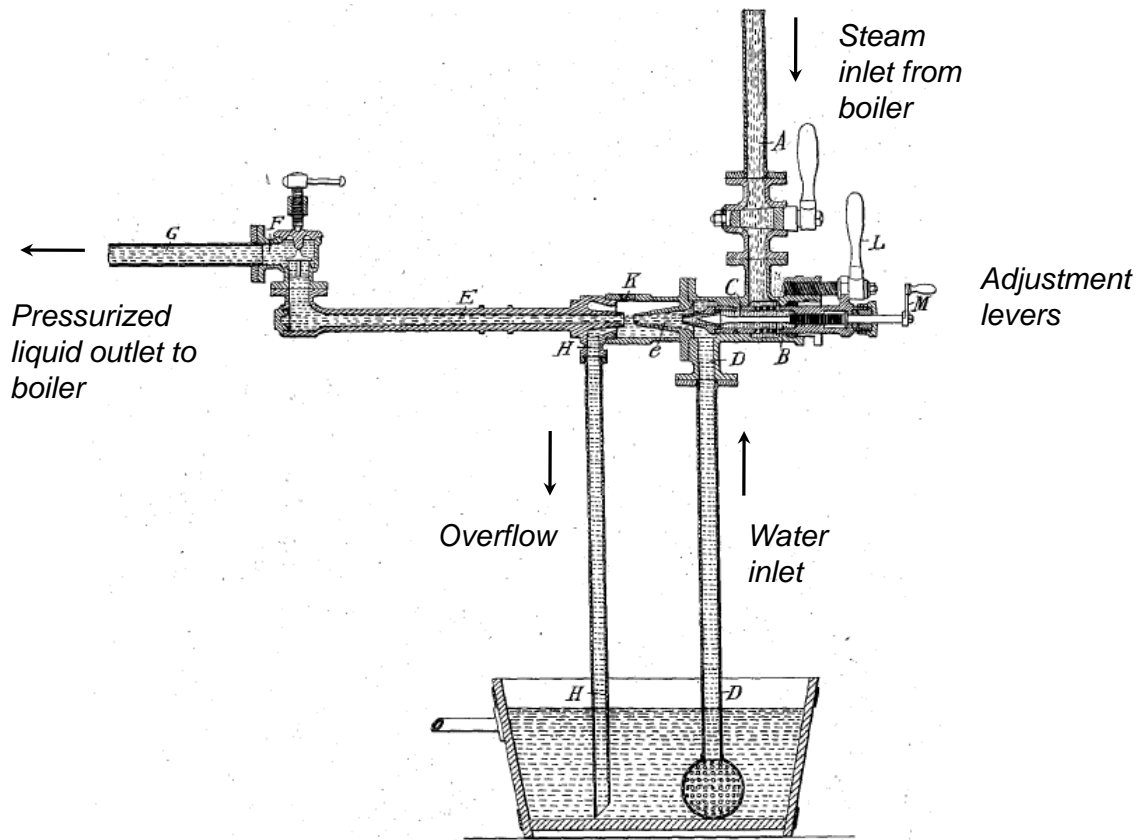


FIGURE 1.30: Giffard's injector from his 1860 US patent [70]

now, the use of jet pumps affords designers the flexibility to accommodate techniques with comparatively low tolerances. Although it is possible for jet pumps to operate less efficiently than mechanical pumps, there may be instances when the designer chooses to accept this design trade-off to enable reduction to practice or simplification, which tends to enable greater adoption through ease of use and decreased cost. This reasoning motivates the current investigation into the use of jet pumps in Power MEMS devices.

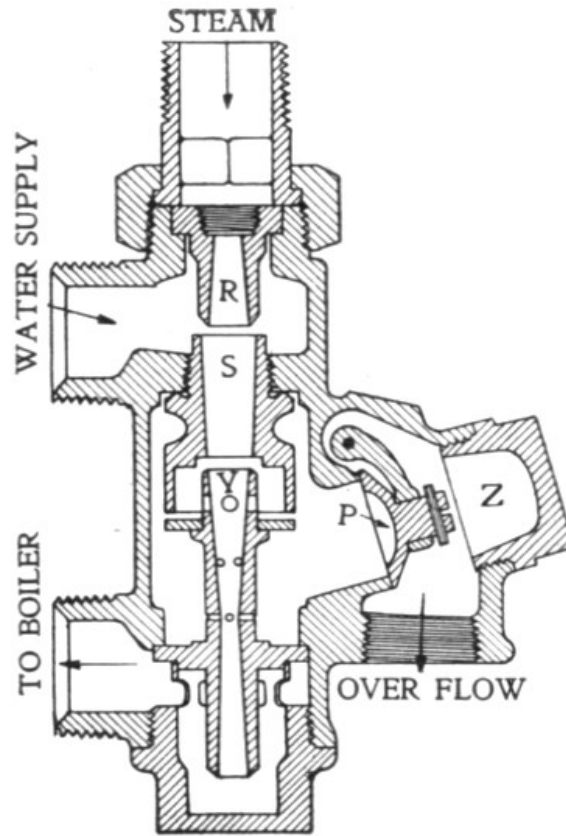


FIGURE 1.31: Cross section of a self-acting Penberthy injector

## 1.6 Objective

The objective of this thesis is to present modeling efforts verified with experimental results for microscale jet ejectors and jet injectors. Microscale jet pumps can assist or enable the reduction to practice of some Power MEMS devices that require fluid pumping. This thesis presents explanation of the approach used to derive analytic models from first principles that capture scale effects experienced at low Reynolds numbers. The models are relatively easy to implement and are presented in effort aid in device design.

## 1.7 Overview

Chapter 1 provides the motivation and background for jet pumps. Chapter 2 presents experimental and analytic results for a single-stage jet ejector tested at three different length scales for different fluids. Chapter 3 presents experimental and analytic results for a single-stage jet injector tested at two different length scales for different fluids. Chapter 4 presents experimental and analytic results for a two-stage jet ejector tested at three different length scales. Chapter 5 presents conclusions and recommendations for future work. The appendices contain the models derived from first principles that include losses experienced at small length scales or low Reynolds numbers.

# 2

## Single-Stage Ejector

This chapter provides a brief background on jet ejectors and potential applications in Power MEMS devices. It also compares a model derived from first principles inclusive of losses to experimental results for a single-stage jet ejector tested at three length scales. Detailed derivations appear in Appendix A (p.106).

### 2.1 Motivation

Microelectromechanical systems (MEMS) have enabled the miniaturization of many macroscale devices, to include systems for power generation, propulsion, sensing, analysis, and flow processing. Devices involving fluid flow require miniaturized fluidic components much like their macroscale analogs. Figure 1.20 (p.25) shows some potential applications for jet ejectors within the Power MEMS field.

One potential application of interest is a MEMS-fabricated Rankine cycle engine (in abstract similar to a steam locomotive engine) whose only moving parts are those associated with power off-take. The core of a jet-pumped Rankine cycle engine, an example being a steam locomotive engine, contains no moving parts; vapor-driven jet injectors pump liquids, and vapor-driven jet ejectors pump gases, as shown in

Chapter 1 in Figure 1.22 (p.27). Low-entrainment vapor-driven jet ejectors first appeared during the 19th century and were ultimately optimized to induce air flow or draft across the firebox, or combustor, of coal-fired steam locomotive engines, expelling entrained exhaust gases out of the stove pipe, or diffuser, as seen in Figure 1.26 (p.31) [47]. The ejector's lack of moving parts affords designers a simple start up protocol, the ability to pump fluids containing particulates, and a reduction of moving parts.

## 2.2 Background and Literature Search

### *2.2.1 Power MEMS Applications*

#### *$\mu$ COIL laser*

One possible Power MEMS application for low entrainment vapor driven jet ejectors is the portable micro-chemical-oxygen-iodine-laser ( $\mu$ COIL). The laser generates hydrogen peroxide steam by catalytic decomposition, driving an ejector-based pressure recovery system that pumps low pressure fluid to the atmosphere [54, 55].

#### *Steam generators and microthrusters*

Investigators have also designed and tested a MEMS vapor generator which can be used to generate motive fluid for vapor driven MEMS jet ejectors, or as a monopropellant microthruster for nanosatellite propulsion [56]. The device decomposes high concentration hydrogen peroxide using a homogenous catalytic solution of ferrous chloride and demonstrated reactor pressures of around  $2atm$ .

#### *Fuel and air delivery*

Investigators have also used butane-vapor-driven, high-entrainment ratio micro jet ejectors to supply fuel-air mixtures to micro combustors in Power MEMS applications [57–60]. Two-dimensional (2-D) motive nozzles were fabricated using deep-reactive-

ion-etching (DRIE) from bonded silicon/glass wafers and silicon/silicon wafers [57–59]. Investigators also performed tests using a  $75\mu\text{m}$  capillary tube that discharged into a larger diameter tube [60]. In other tests, a one-dimensional (1-D) axisymmetric nozzle fabricated in stainless steel by electrical-discharge-machining (EDM) was tested with a throat diameter of  $42\mu\text{m}$  and throat Reynolds numbers near 3,600 [60].

### *Micro analytics*

Other investigators have micromachined 2-D single- and multi-stage vapor driven vacuum pumps for use in miniaturized analytical ('lab on a chip') systems such as mass spectrometers [74, 75]. These vacuum pumps demonstrated jet pump operation at the microscale [74], achieving a vacuum of 495 mbar, and presented a system with an integrated heater and Pirani pressure sensor [75].

## *2.2.2 Macroscale Applications*

### *Aerospace*

Ejector nozzles have found use in high-performance supersonic aircraft to aerodynamically vary the exhaust nozzle expansion ratio to allow for operation at different conditions [29]. Secondary flow enters the exhaust nozzle, varying the flow area available for the engine core flow. These ejectors can be implemented using tail flaps or blown in doors which adjust depending on operating speed. At low aircraft speed, the secondary flow also prevents separation in the exhaust nozzle if the core engine flow is lower than the amount required for proper nozzle operation [29].

Investigators have proposed the use of ejectors for thrust augmentation and heat signature suppression in turbofan, rotary wing and rocket propelled aircraft [76]. These results demonstrate an increase in efficiency with multi-staging and will be discussed in Chapter 4.

### *Chemical engineering*

Ejectors have also historically found wide use in the chemical engineering field, especially for steam and air driven applications, where they have been used to exhaust fumes or air, drive vacuum evaporation, distillation, refrigeration, filtration, drying, and air conditioning [77]. Some researchers in the chemical engineering and process fields are examining the use of ejectors as heat pumps in lieu of electrically powered mechanically driven vapor compressors, or the comparatively larger absorption chillers [78, 79]. Experimental work and CFD simulations have been used to analyze ejectors driven by the vapors of ammonia, FC-134a, propane [78], methanol [79], and water [80]. A summary of recent work in the refrigeration field appears in Reference [81].

#### *2.2.3 Early Work and Theory*

Goss carried out the first “comprehensive work” on steam locomotive ejectors between 1890-1908 at Purdue University [47, 62–69]. Kroll provides design guidelines and a brief summary of data for steam-air and air-air ejectors dating between 1928-1943 [77]. Keenan presents an analytic model developed from first principles for conventionally sized ejectors [82]. Batchelor presents equations of motion for laminar free jets [83], White and Greitzer present empirical results for turbulent free jets and shear layers [37, 84]. Shapiro, Kerrebrock, and Greitzer present inviscid ejector models for both compressible [29, 85] and incompressible [37] flows.

## 2.3 Objective

The work presented in Chapter 2 demonstrates the feasibility of using single-stage jet ejectors to either substitute or supplement mechanically driven microscale pump. Microscale jet ejectors can meet the gas pumping requirements of Power MEMS devices and can, in some cases, serve as a viable substitute for compressors or draft

fans [31, 48, 86], in addition to substituting for fuel-air delivery systems [57–60] and vacuum pumps [74, 75].

Chapter 2 reports on experiments performed on microscale ejectors of similar geometry, which feature three different motive nozzle throat diameters of  $64\mu\text{m}$ ,  $187\mu\text{m}$  and  $733\mu\text{m}$ . A theoretical model is developed from first principles (see Appendix A on p. 106 for the detailed derivation) that includes losses due to scale effects, or low Reynolds numbers, as well as the secondary fluid inlet losses. The model is used to further predict a theoretical minimum ejector size corresponding to a maximum achievable power density on the order of 1 MW/L.

## 2.4 Theory and Modeling

### 2.4.1 *Physical Description*

A single-stage ejector consists of a motive nozzle and mixer/diffuser. Figure 2.1 (p. 44) outlines the ejector configuration and flow paths used for analysis. Jet ejectors pump fluid by exchanging momentum between a high velocity primary, or motive, flow and a quiescent or low velocity secondary flow, producing a mixed-out discharge flow with an intermediate velocity. The motive jet entrains the surrounding fluid by viscous interaction. The jet inviscid core centerline velocity does not vary with axial distance until the downstream point where shear layers thicken and merge, resulting in the disappearance of the core flow. Entrainment of secondary fluid is assisted by the local drop in static pressure surrounding the jet, which is caused by movement of secondary fluid from viscous entrainment and also by motive jet expansion for the case of a supersonic jet expanding to pressure lower than ambient. This drop in static pressure causes some secondary flow towards the jet's centerline axis and is sometimes commonly referred to as the 'Venturi effect' [37, 83, 84]. This effect is driven by secondary flow motivated by friction or viscous entrainment between the motive jet issuing into the quiescent secondary fluid.

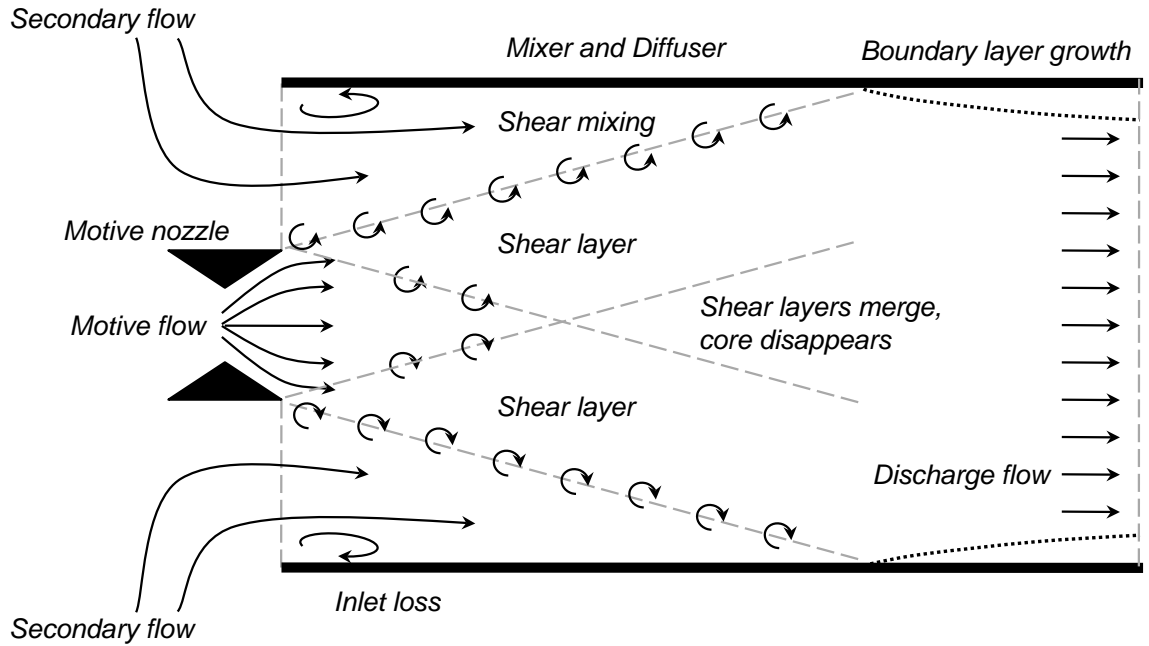


FIGURE 2.1: Example ejector assembly and flow paths

#### 2.4.2 Model Approach

The ejector model develops from theoretical first principles, applying the conservation of mass, momentum and energy across a constant area mixing duct. The model assumes compressible flow through the motive nozzle and models incompressible flow through the secondary fluid inlet and mixer region for a single-stage axial flow configuration shown in Figure 2.2 (p. 45).

In Figure 2.3 (p. 46),  $A_m$  represents the motive nozzle exit area. It should be noted that the  $e$  subscript has been dropped,  $A_{m,e} \Rightarrow A_m$ . The secondary flow area,  $A_s$ , is computed by taking the difference between the mixer area,  $A_d$ , and motive nozzle exit area,  $A_s = A_d - A_m$ . In practice, the axial distance between the motive nozzle exit plane and the mixer inlet plane can be used to restrict secondary flow. This axial distance is typically set between  $0.5 - 1D_d$  and is made to be adjustable

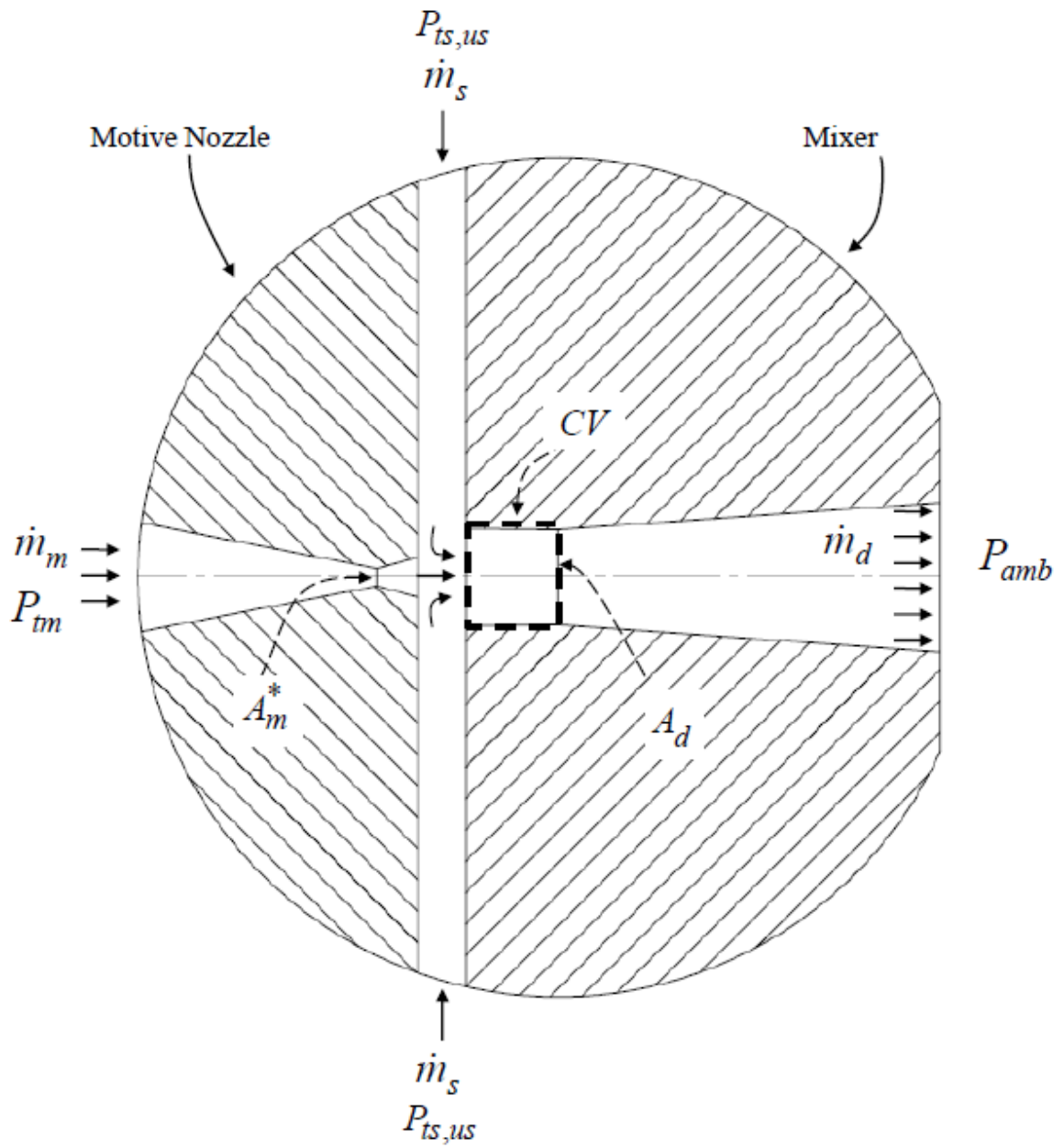


FIGURE 2.2: Ejector assembly and flow paths [31]

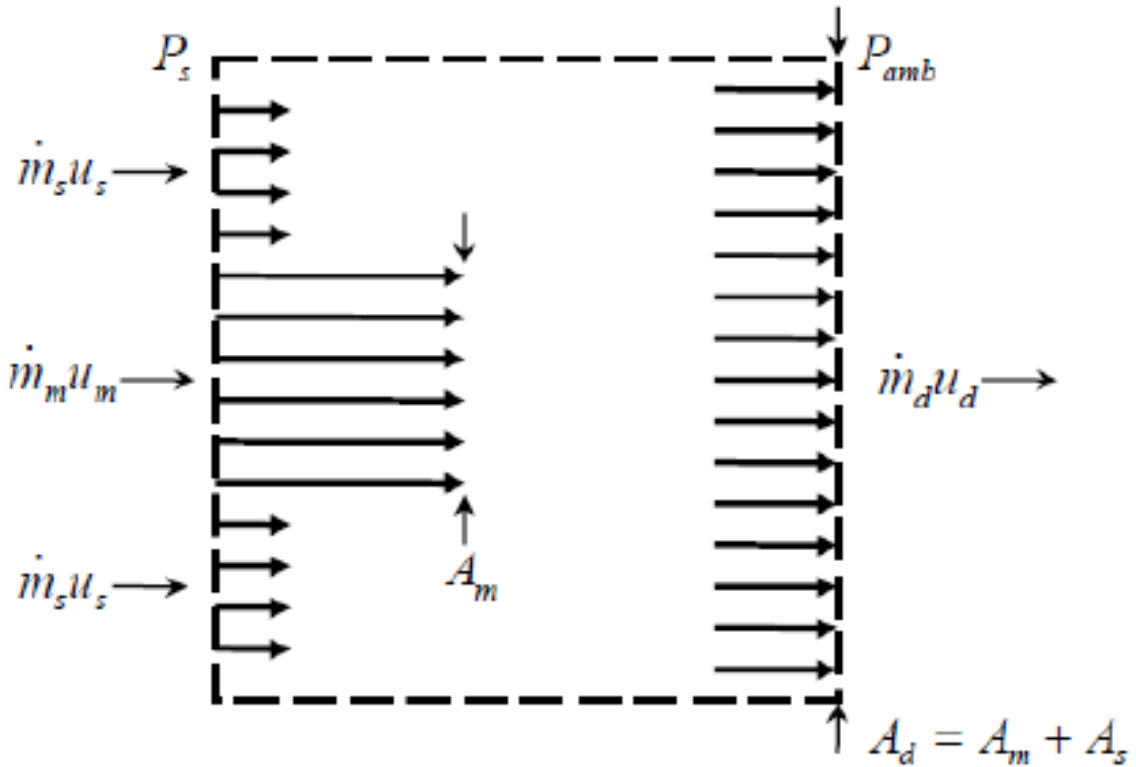


FIGURE 2.3: Control volume detailing nomenclature [31]

for macroscale ejectors [77, 87]. The model includes losses associated with secondary flow inlet restriction and viscous losses throughout the motive nozzle and mixing region. The detailed derivation of this model appears in Appendix A beginning on p. 106. The ratios of discharge and secondary fluid densities to motive fluid density are assumed to approximately equal unity in the mixing region,  $\rho_d/\rho_m \approx \rho_s/\rho_m \approx 1$ , by use of an approximate similarity principle first introduced by Munk and Prim and described by Greitzer and Presz in References [76, 88, 89]. The conservation of mass and momentum in conjunction with the conservation of energy in the form of the steady Bernoulli equation establishes expressions for entrainment ratio and ejector suction draft. For the design considered below, we assume that the discharge

static pressure is equal to ambient conditions with an arbitrary supply total pressure,  $P_{t,s,supply} = P_{t,s,us} = P_{t,s}$  for the secondary fluid.

### 2.4.3 Analytic Model

Using the aforementioned approach, the inviscid model, assuming optimal nozzle expansion (matched exit static pressure), for ejector suction draft (or pressure coefficient) can be expressed as a function of entrainment ratio, defined as the ratio of secondary to motive mass flow rates,  $\alpha \equiv \dot{m}_s/\dot{m}_m$ , and the ejector area ratio, defined as the ratio of secondary to motive flow areas,  $a \equiv A_s/A_m$ , shown in equation (2.1).

$$\frac{P_d - P_{t,us}}{1/2\rho u_{m,isen}^2} = \frac{2a}{(1+a)^2} \left[ 1 - 2\frac{\alpha}{a} - \frac{1}{2} \left( a + 1/a \right) \frac{\alpha^2}{a^2} \right] \quad (2.1)$$

Inclusive of losses, equation (2.1) becomes equation (2.2). The approach and detailed steps are provided in Appendix A (106).

$$\begin{aligned} \frac{P_d - P_{t,us}}{1/2\rho u_{m,isen}^2} &\approx \frac{2a}{(1+a)^2} \left[ 1 - 2\frac{\alpha}{a} - \frac{1}{2} \left( a + 1/a \right) \frac{\alpha^2}{a^2} \right] \dots \\ &\quad - \left( \frac{1}{C_d^2} - 1 \right) \frac{\alpha^2}{a^2} \dots \\ &\quad - \frac{4/\epsilon_m}{\cos \theta} \frac{\left( 1 + \frac{\gamma-1}{2} M_{e,m}^2 \right)^{\frac{\gamma}{\gamma-1}}}{\frac{\gamma}{2} M_{e,m}^2} CRe_{D_m^*}^{-m} \left( \frac{L}{D_m^*} \right)^{1-n} \dots \\ &\quad - 4 \frac{(1+\alpha)^2}{(1+a)^2} CRe_{D_d}^{-m} \left( \frac{L_d}{D_d} \right)^{1-n} \dots \\ &\quad - \frac{1}{1+a} \frac{P_s - P_{m,e}}{1/2\rho u_{m,isen}^2} \end{aligned} \quad (2.2)$$

The leading-bracketed term represents the suction or vacuum created when the entrainment ratio is zero, indicating no secondary flow, which occurs when the secondary flow is throttled to zero. The first term represents the incompressible, inviscid

model which computes ejector performance for a given geometry and entrainment ratio. The discharge static pressure, or ejector back pressure, is general but is set equal to ambient pressure for the data presented below. The secondary fluid supply pressure or total pressure upstream of the ejector is also general. The secondary inlet discharge coefficient,  $C_d$ , captures the losses associated with sharp turning or non-ideal inlet geometries. References [37, 83, 90] provide typical values for different inlet geometries, some of which can be derived from first principles. This loss mechanism physically manifests itself as a flow area restriction.

The third term in equation (2.2) results from friction in the motive nozzle. Typically, for nozzles which operate in the turbulent flow regime, the local skin friction coefficient,  $C_f$ , which is the non-dimensional drag force on the nozzle walls, experiences negligible variation across the nozzle's axial length [36]. However, as nozzle length scale decreases, the local skin friction coefficient varies and must be computed as the assumption of negligible variation may no longer hold. This computation also allows for prediction of more pronounced viscous losses experienced at small length scales. The drag force on the nozzle walls is computed by integrating the product of the local skin friction coefficient and local dynamic pressure across the wetted area of the nozzle, as shown in equation (A.38) (p.117) in Appendix A.

The fourth term in equation (2.2) accounts for viscous losses in the mixing region due to mixer wall drag. The drag force is modeled for a constant area duct and is a function of the mixer Reynolds number, ejector geometry and entrainment ratio.

The fifth term in equation (2.2) results from the conservation of momentum applied to the motive nozzle. The nozzle exit plane pressure matching term can result in decreased nozzle performance if the exit static pressure of the nozzle flow differs from the surrounding ambient static pressure. Under optimal conditions for matched nozzles, this last term is zero.

Figure 2.4 (p.49) illustrates the magnitudes of the different loss terms in equa-

tion (2.2) for an arbitrarily selected entrainment ratio of  $\alpha = 0.4$ , as well as the total magnitude of viscous losses compared to the inviscid model given by equation (2.1) across different Reynolds number based on the motive nozzle throat diameter. Losses increase from roughly 10% at Reynolds numbers above  $10^6$  to nearly 100% for Reynolds numbers near  $10^2$ . The jump discontinuities result from flow regime transition from turbulent to laminar.

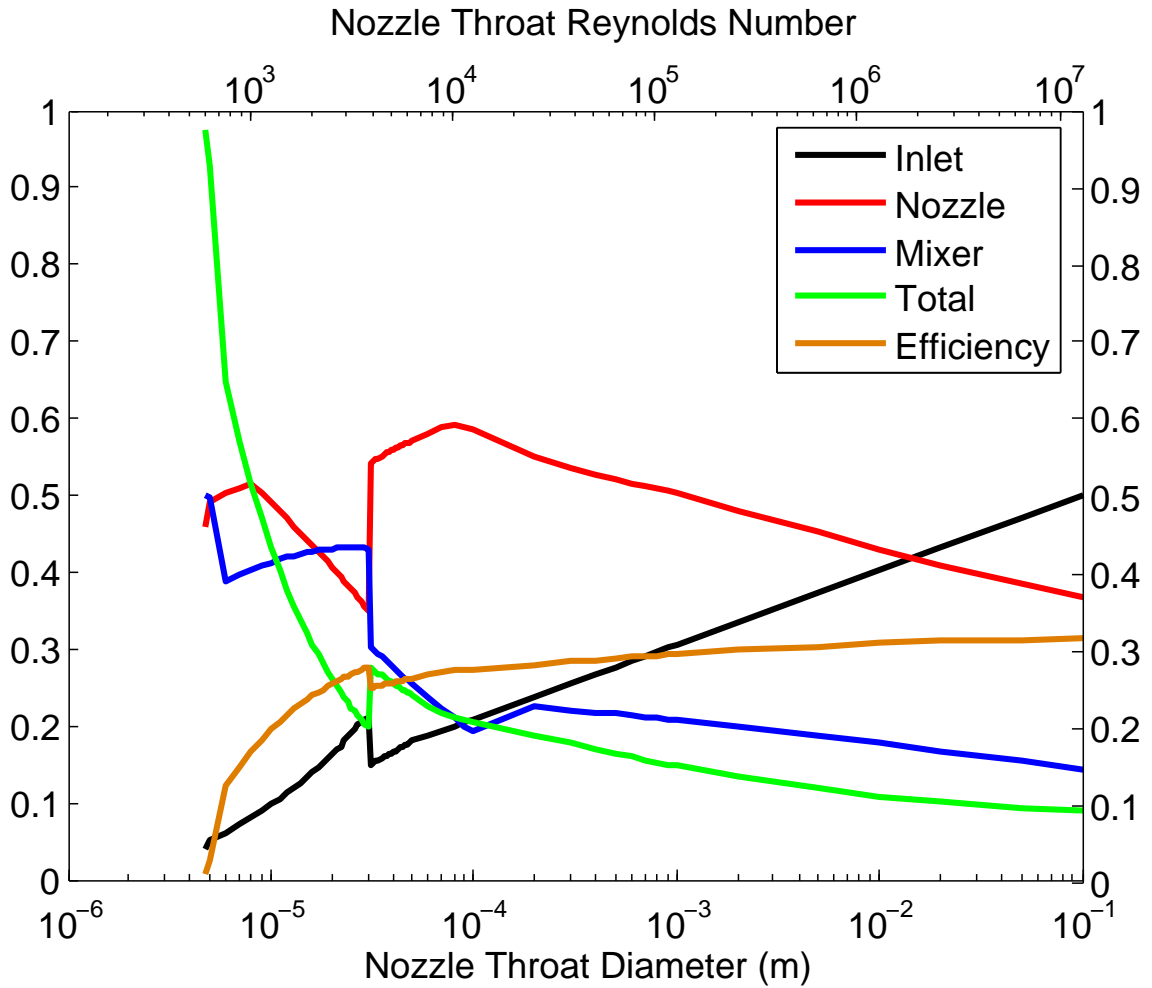


FIGURE 2.4: Magnitude of losses with respect to the inviscid model versus Reynolds number. The jump discontinuities arise from flow regime transition.

#### 2.4.4 Efficiency

To establish an ejector efficiency, we invoke the conservation of momentum and mass, assuming constant static pressure throughout the ejector, and can express the ideal ejector suction draft as

$$\frac{P_{amb} - P_{t,us}}{1/2\rho u_{m,isen}^2} = \frac{1}{(1 + \alpha)^2} \quad (2.3)$$

where the suction draft is independent of area ratio and is purely a function of entrainment ratio. Using this as a bound on the upper performance limit, the ejector efficiency can be defined as the ratio of the realized suction draft to the idealized result in equation 2.3.

$$\begin{aligned} \eta &\equiv \frac{P_{amb} - P_{t,us}}{1/2\rho u_{m,isen}^2} \bigg/ \frac{P_{amb} - P_{t,us}}{1/2\rho u_{m,isen}^2} \bigg|_{ideal} \\ &= \left( \frac{P_{amb} - P_{t,us}}{1/2\rho u_{m,isen}^2} \right) (1 + \alpha)^2 \end{aligned} \quad (2.4)$$

From the defined ejector efficiency in equation 2.4, we see that, for any given area ratio, an optimum entrainment ratio exists which maximizes efficiency. Neglecting viscous losses in the motive nozzle and mixer, the ejector efficiency becomes

$$\eta = 2a \left( \frac{1 + \alpha}{1 + a} \right)^2 \left[ 1 - 2\frac{\alpha}{a} - \frac{\alpha^2}{a^2} \left( \frac{1}{C_d^2} \frac{(1 + a)^2}{2a} - 1 \right) \right] \quad (2.5)$$

which can be optimized analytically by setting  $\partial\eta/\partial\alpha = 0$  to yield

$$\alpha_{opt} = \frac{-2a^3 + a^2(1 + a)\sqrt{1 + \frac{a-1/a}{C_d^2}}}{\frac{(1+a)^3}{C_d^2} - a(1 + 3a)} \quad (2.6)$$

For the special case where both suction inlet and viscous loss mechanisms are neglected, Figure 2.5 (p.51) identifies this optimum efficiency curve across various entrainment ratio and area ratio pairings.

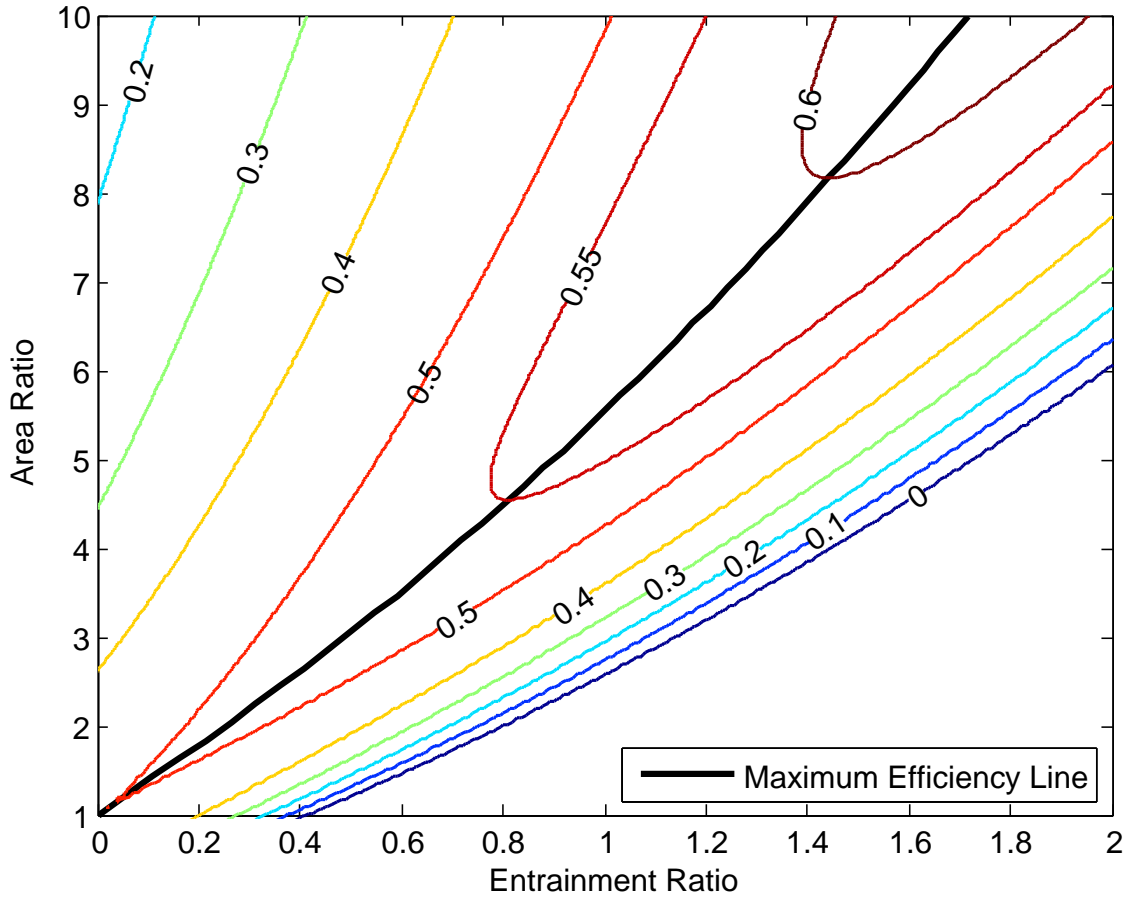


FIGURE 2.5: Optimum efficiency line from equation 2.5, [31]

To see the effects of the secondary discharge coefficient in equation (2.5), Figure 2.6 (p.52) plots the optimum efficiency curve for a value of  $C_d = 0.5$  across various entrainment ratio and area ratio pairings.

For convenience, the relationship between the entrainment and area ratios for maximum ejector efficiency can be approximated by a power law curve fit,

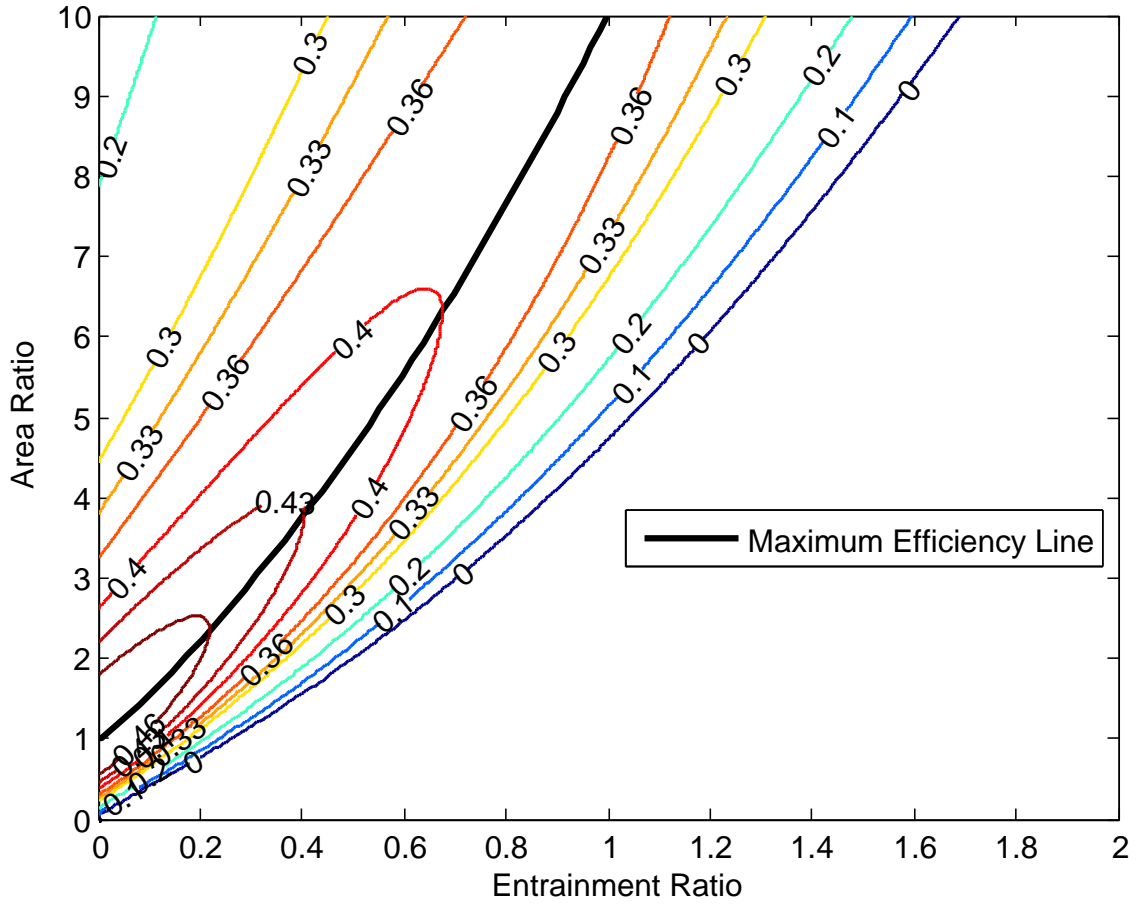


FIGURE 2.6: Optimum efficiency line from equation 2.5 with  $C_d = 0.5$ , [31]

$$1 + \alpha_{opt} \approx 0.685(1 + a)^{0.57} \quad (2.7)$$

which predicts the optimum entrainment ratio for a loss-free ejector to within 7% of equation (2.5) across a range of ejector area ratios from 8 to 20.

#### 2.4.5 Power Density

Ejector power density scaling laws may be predicted theoretically for a loss-free device. Then, through substitution of full-loss model for the inviscid model, the

minimum theoretical ejector size can be predicted. We begin by estimating the the ejector volume as

$$V = \frac{\pi}{4} D^{*3} [(L/D^*_m)_{nozzle} + (L/D)_{mixer} a^{3/2} \epsilon^{3/2}] \quad (2.8)$$

The pumping power is

$$\dot{W} = \dot{m}_s \Delta P_t / \rho \quad (2.9)$$

which gives a non-dimensional power density of

$$\frac{\dot{W}/V}{1/2\rho u_{m,isen}^3} = \frac{1}{D^*} \alpha \frac{\Delta P}{1/2\rho u_{m,isen}^2} [(L/D^*_m)_{nozzle} \epsilon^{-1} + (L/D)_{mixer} a^{3/2} \epsilon^{1/2}]^{-1} \quad (2.10)$$

Therefore, in the absence of losses the power density scales with the inverse of the nozzle throat diameter.

## 2.5 Experimental Approach

The motive nozzle is a 1-D axisymmetric converging-diverging nozzle. The diverging section for the nozzle produces a design expansion ratio of 2.5:1. Table 2.1 (p.54) provides the ejector design geometry, and Tables 2.2 (p.54) and 2.3 (p.54) compare this design geometry to the manufactured geometries for the nozzle and ejector assembly, respectively [31]. Figure 2.2 (p.45) depicts the ejector assembly, which consists of the motive nozzle and mixer. Electrical-discharge machining (EDM) was used to fabricate the nozzle geometries of Figures 2.7b and 2.7c (p.55) in stainless steel. The  $64\mu m$  nozzle shown in Figure 2.7a (p.55) was microfabricated from aluminum using a  $50\mu m$  carbide drill bit from Drill Bit City (Chicago, IL) and a single-lip cutter. In a batch process, DRIE could be used in lieu of EDM or CNC to produce 2-D nozzle geometries [2, 3, 57, 58, 75]. The mixer region allows the motive and suction flows

to mix out and then decelerate. An adequate mixing length must be provided to ensure proper on-design operation, typically from  $5 - 10D_d$  for conventional mixers and diffusers without mixing features [77].

Table 2.1: Ejector design geometry

| Expansion ratio $\epsilon_m$ | Expansion angle $\theta_m$ | Nozzle $L/D$ | Ejector area ratio $a$ | Mixer $L/D$ |
|------------------------------|----------------------------|--------------|------------------------|-------------|
| 2.5                          | $15^\circ$                 | 4.3          | 8                      | 10          |

Table 2.2: Comparison of design versus realized motive nozzle geometry

| Motive Nozzle | Design throat width $D_m^*$ | Design expansion ratio $\epsilon_m$ | Actual throat width $D_m^*$ | Actual expansion ratio $\epsilon_m$ |
|---------------|-----------------------------|-------------------------------------|-----------------------------|-------------------------------------|
| Small         | $50\mu m$                   | 2.5                                 | $64\mu m$                   | 3.3                                 |
| Medium        | $168\mu m$                  | 2.5                                 | $187\mu m$                  | 2.7                                 |
| Large         | $755\mu m$                  | 2.5                                 | $733\mu m$                  | 2.2                                 |

Table 2.3: Comparison of design versus realized ejector geometry

| Motive nozzle exit diameter | Design ejector area ratio | Actual ejector area ratio |
|-----------------------------|---------------------------|---------------------------|
| $116\mu m$                  | 8                         | 7.6                       |
| $309\mu m$                  | 8                         | 5.1                       |
| $1097\mu m$                 | 8                         | 8.7                       |

Ejector performance tests were carried out using nitrogen gas or ethanol vapor as the motive fluid using the test rig shown in Figure 2.8 (p.57) [31, 48, 53]. The secondary fluid for both motive fluids was quiescent ambient air. For nitrogen tests, pressurized tank nitrogen was delivered to the ejector using a regulated valve. For ethanol vapor tests, a stainless steel boiler was heated to the desired pressure using an electric hot plate. An inline  $7\mu m$  filter placed directly upstream of the ejector was used to avoid clogging the motive nozzle. The secondary air mass flow rate was measured using an MKS Alta-180 mass flow meter with a 0-20,000 sccm range and measured reading error of 1%. The entrainment ratio was varied by adjusting an air-side needle valve downstream of the mass flow meter at constant motive supply

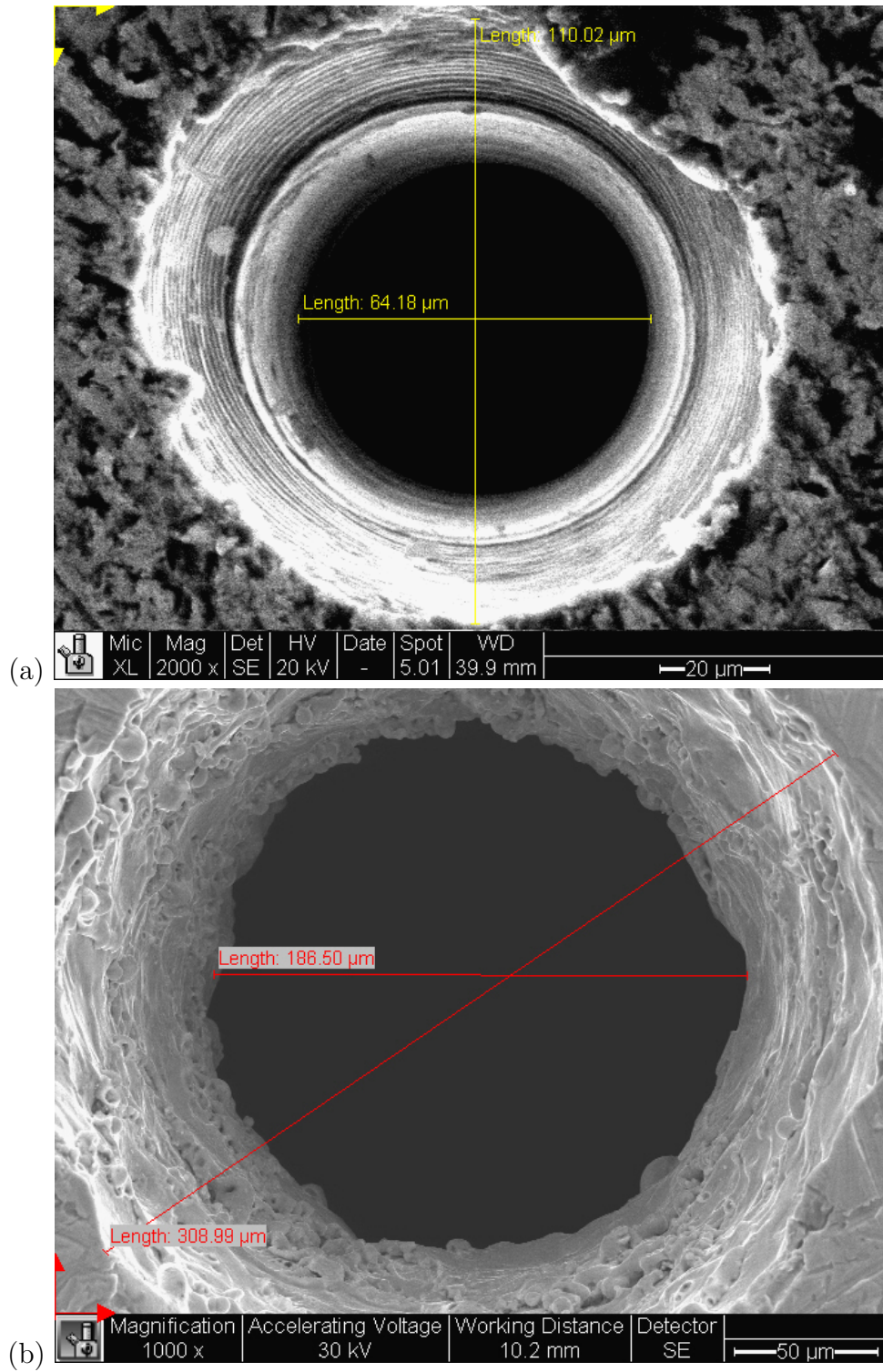
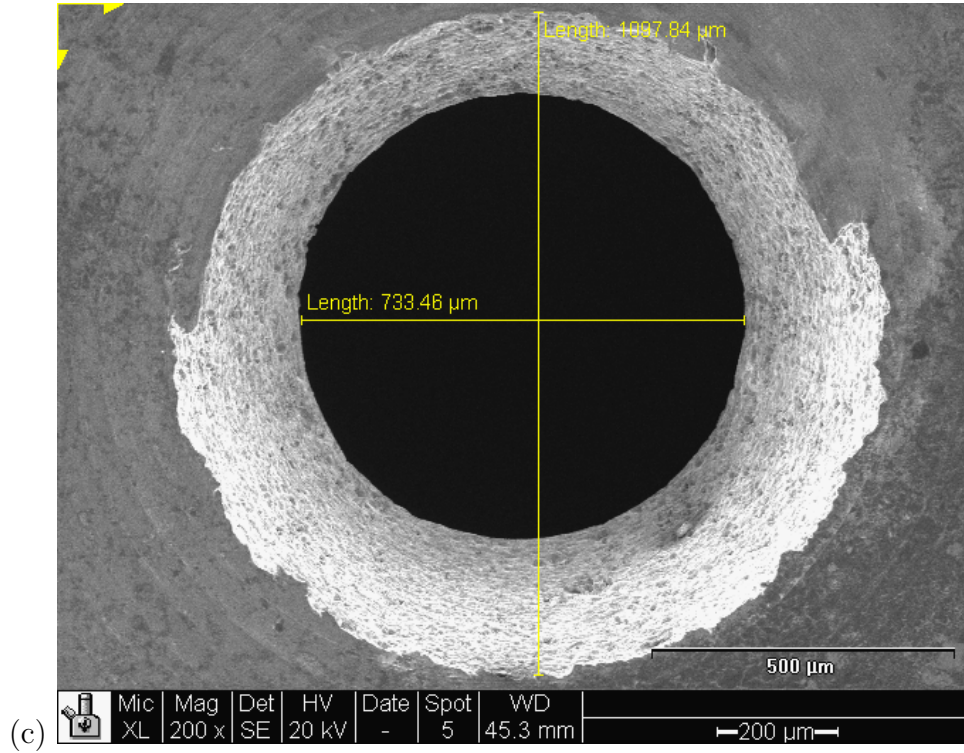


FIGURE 2.7: Realized geometry for ejector motive nozzles SEM images of (a) 64  $\mu\text{m}$  nozzle, (b) 187  $\mu\text{m}$  nozzle, (c) 733  $\mu\text{m}$  nozzle [31]



total pressure. All tests were performed with atmospheric backpressure at the mixer exit.

Realized mass flow rates through nozzles are typically compared to isentropic mass flow rates using the nozzle discharge coefficient,  $C_{\dot{m}} \equiv \dot{m}/\dot{m}_{isen}$ , which is typically near unity for well-designed nozzles with Reynolds numbers around  $10^6$  [85]. The nozzle discharge coefficient for the 187μm nozzle was measured using nitrogen gas, which provided a discharge coefficient of 95% at the design Reynolds number of 25,000, which is consistent with previous micronozzle work that reported similar discharge coefficients above 90% at Reynolds numbers as low as 500 [2, 3]. Displacement boundary layer thickness tends to be negligible at nozzle throat station. Thus, realized mass flow rates compare well to isentropic calculations even at low Reynolds numbers, as shown in [2, 3]. This negligible blockage at the nozzle throat

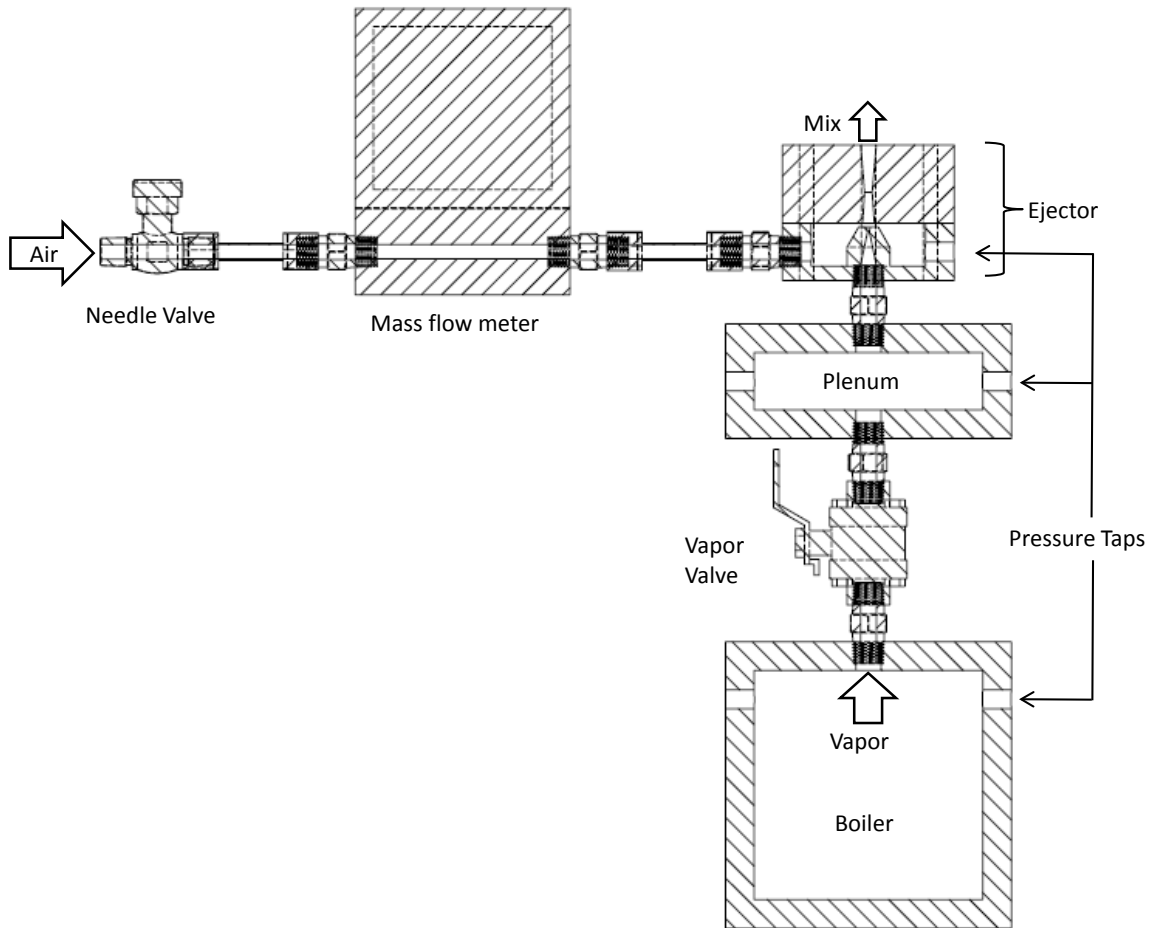


FIGURE 2.8: Experimental test rig. The entrainment ratio is varied by needle valve adjustment. The boiler generates ethanol vapor or accepts pressurized gas, which is throttled to a regulated plenum. The vapor accelerates and expands through the motive nozzle, entraining quiescent air and discharges to atmosphere. Secondary mass flow rates are measured using an MKS Alta-180 mass flow meter, and motive mass flow rates are computed based on measured upstream conditions and realized nozzle geometries, [48], [31]

is in part due to the favorable pressure gradient, which means that the downstream locations have lower static pressure than upstream locations, across the nozzle inlet to throat region, which suppresses boundary layer growth as the flow accelerates [29, 36, 37, 85, 90]. The image processing software, *ImageJ*, was used to compute the nozzle throat area from SEM images. This measured throat area was then used to compute the isentropic mass flow rate. The estimated area from *ImageJ* affected the coefficient of discharge magnitude by a single percentage point or two when compared to the area computed using the approximated circular diameter measured from SEM images. Measured mass flow rates through the nozzle confirm sonic conditions at the nozzle throat. Figure 2.9 (p.59) compares measured mass flow rates to computed isentropic flow rates for the  $187\mu m$  nozzle [48].

## 2.6 Experimental Results and Discussion

The observed mass flow efficiencies of the  $187\mu m$  nozzle deviated less than 5% from a representative one-dimensional isentropic flow model over a range of supply pressures. This deviation, shown in , Figure 2.9 (p.59) may be due to surface roughness, boundary layer growth and corresponding viscous losses. The good agreement between the measured mass flow efficiencies and isentropic flow computation is supported by two-dimensional micronozzle measurements [2, 3], which report comparable mass flow efficiencies for Reynolds numbers as low as 500. Since boundary layer growth is typically suppressed at the nozzle throat due to the favorable pressure gradient, blockage effects are minimal. Boundary layer growth at low Reynolds numbers tends to have the most pronounced effect on nozzle flow near the nozzle exit region, where the boundary layers have been allowed some axial flow length to grow and sometimes merge.

Figure 2.10 (p.60) reports suction draft and ejector efficiency versus entrainment ratio for the design ejector geometry provided in Table 2.1 (p.54) at three length

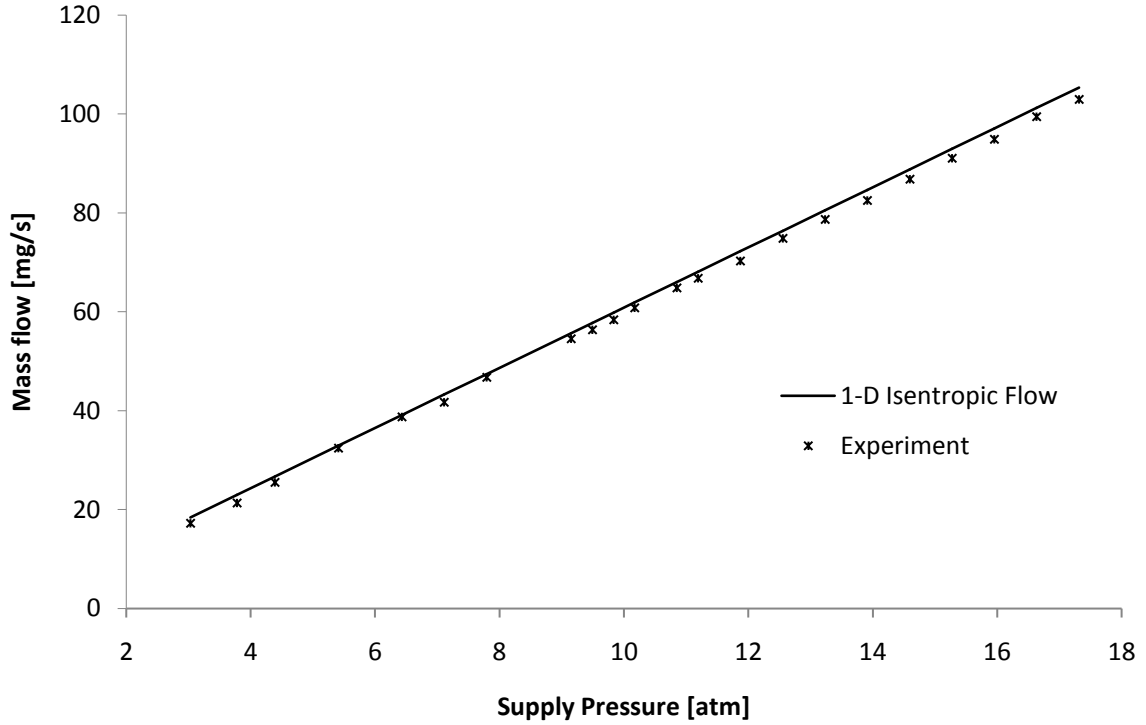


FIGURE 2.9: Nitrogen mass flow experimental results compared to an isentropic flow model for a  $187\mu m$  throat diameter nozzle with a 2.7:1 expansion ratio.

scales, provided Tables 2.2 (p.54) and 2.3 (p.54), in using nitrogen gas as the motive fluid. Figure 2.11 (p.61) reports similar data for ethanol vapor and air. The small nozzle failed during other tests, which is why only two length scales appear in Figure 2.11 (p.61). All of the model data points are computed using the design geometry given in Table 2.1 (p.54), and all experimental parameters are computed using realized geometries and measured state variables at a supply motive total pressure of  $P_{t,m} = 10 atm$ .

Figure 2.10 (p.60) demonstrates good agreement between experimental observation and model prediction for ejector performance and efficiency. Suction inlet losses become significant at higher entrainment ratios, causing a sharp decline in perfor-

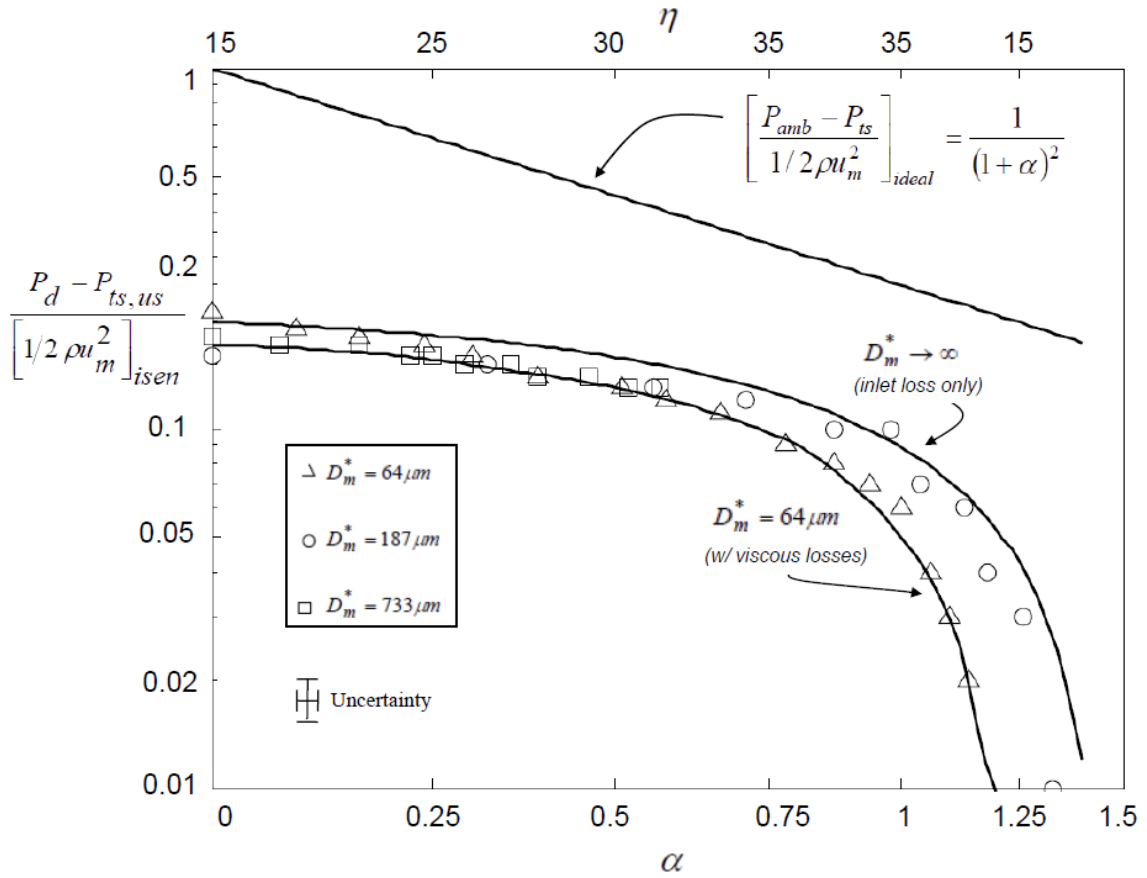


FIGURE 2.10: Model and experimental data for ejector efficiency and suction draft performance versus entrainment ratio for nitrogen gas / air [31]

mance when compared to ideal performance. The complete viscous loss model from equation (1) predicts ejector performance to within measurement error. The experimental data points for suction draft were computed using measured pressures and computed nozzle exit dynamic pressure based on observed pressures and temperatures. Motive nozzle exit velocities were computed using the exit Mach number and realized geometry, further assuming nozzle skin friction losses. The  $64 \mu m$  motive nozzle constructed from aluminum failed during the ethanol tests, perhaps due to the decrease in yield strength at elevated temperatures. The fabrication method for

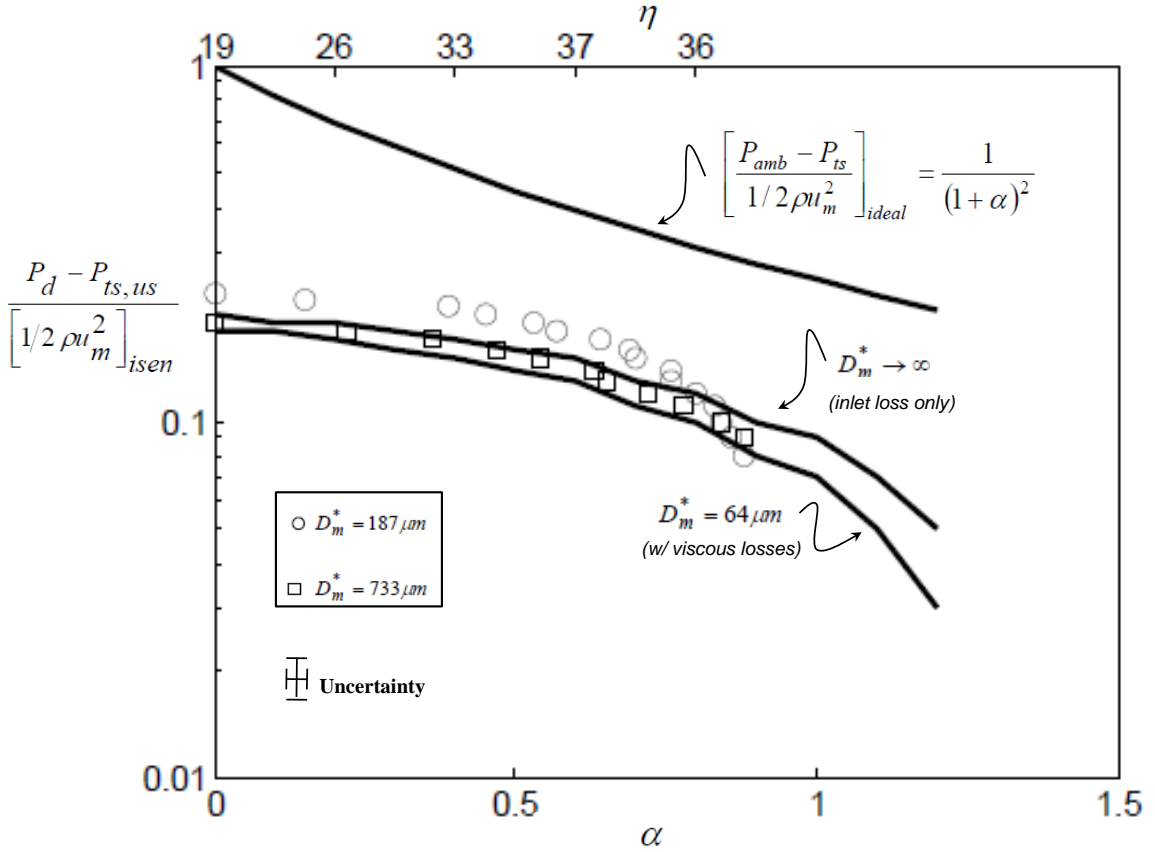


FIGURE 2.11: Model and experimental data for ejector efficiency and suction draft performance versus entrainment ratio for ethanol vapor / air [48]

this nozzle required a thin web in which the nozzle geometry was fabricated since the micro drill bit can only plunge roughly 5 times its diameter of  $50 \mu m$ . This web around the nozzle yielded and blew out during hot tests with ethanol vapor.

The exit momentum for both fluids is similar, as shown in Table 2.4.

The complete loss model from equation (2.2) anticipates a scaling limit for ejector performance at which the maximum power density is achieved, shown in Figure 2.12 (p.62). Below motive nozzle throat diameters of  $10 \mu m$ , the power density

Table 2.4: Comparison of nozzle exit momentum for ethanol vapor and nitrogen gas

| Motive fluid | $P_{t,m}$ | $T_{t,m}$ | $u_{m,e}$ | $\dot{m}_m$ |
|--------------|-----------|-----------|-----------|-------------|
| Ethanol      | 10 atm    | 424 K     | 558 m/s   | 60 mg/s     |
| Nitrogen     | 10 atm    | 300 K     | 560 m/s   | 60 mg/s     |

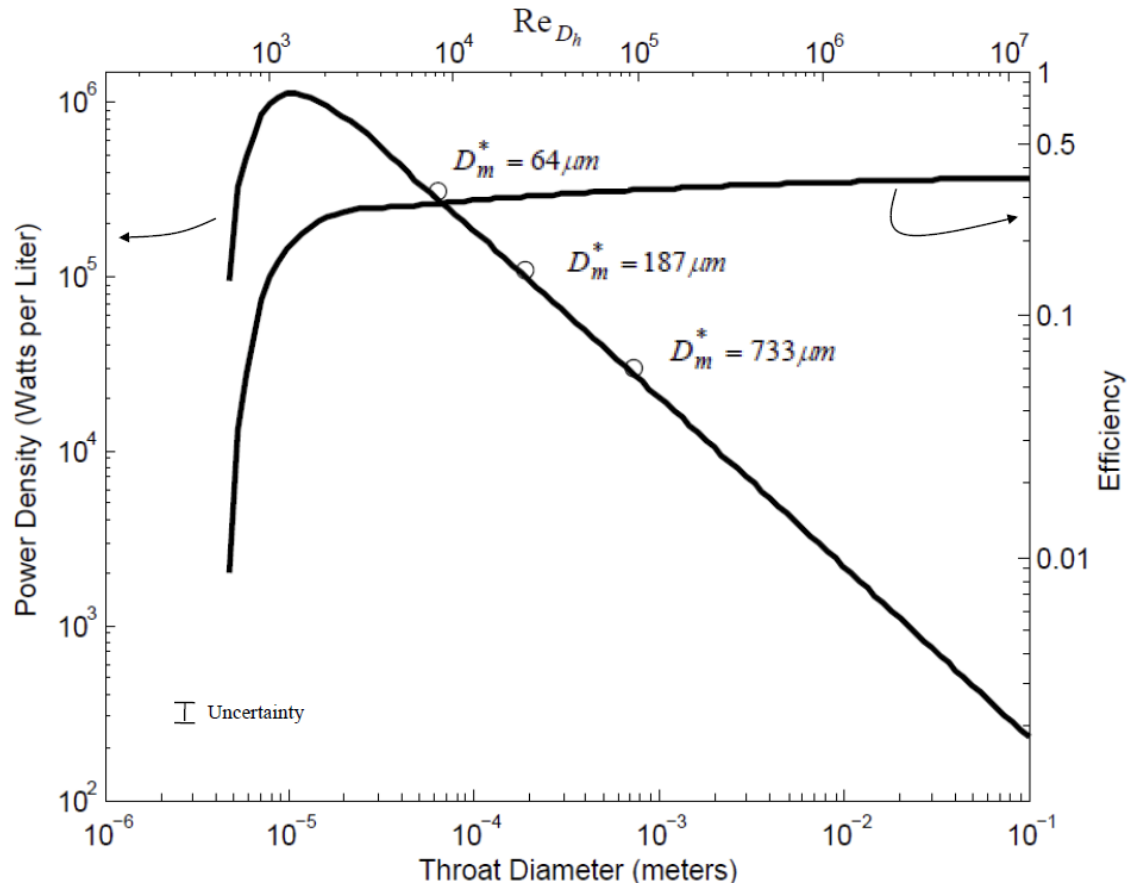


FIGURE 2.12: Model and experimental data for power density and ejector efficiency as a function of nozzle throat diameter for nitrogen gas / air [31]

and ejector performance plummet due to viscous losses. The pronounced viscous losses in the laminar flow regime are predicted to be prohibitive to ejector performance at smaller length scales.

When integrating the ejector into a system such as a microengine, system performance becomes dependent on power density and efficiency. Power density peaks near throat diameters of  $10\mu m$  with a Reynolds number based on throat diameter,  $Re_{D_m^*}$ , near 1,300. Equation (2.2) implies a theoretical peak power density of 1MW/L, which is nearly 3x the observed power density of 308 kW/L for the  $64\mu m$  ejector driven by nitrogen gas. There may exist some applications where size constraints take priority over performance or efficiency. For example, Figure 2.12 (p.62) shows that a  $5\mu m$  throat diameter nozzle will give similar power density to the  $64\mu m$  throat diameter nozzle. For this example, the order of magnitude size reduction also carries with it an order of magnitude reduction in efficiency, as seen in Figure 2.12 (p.62).

## 2.7 Conclusions

An ejector geometry was tested at three length scales with motive nozzle throat widths of  $64\mu m$ ,  $187\mu m$  and  $733\mu m$ . Experimental results agree well with the analytic model derived from first principles, inclusive of secondary flow inlet losses and viscous losses in the motive nozzle and mixing regions. The experimental data suggest that viscous losses have minimal effect on the ejector performance at the tested length scales. The  $64\mu m$  ejector achieved a power density of 308 kW/L during nitrogen gas tests using only a static structure, representing an improvement in the state-of-the-art as compared to microscale turbomachinery with a reported power density of 80 kW/L [15, 21]. The present theoretical model suggests that higher power densities are possible, with a maximum estimated at 1.1 MW/L corresponding to a nozzle throat diameter of  $10\mu m$  with a Reynolds number based on nozzle throat diameter of 1,300 [31].

# 3

## Injector

This chapter provides a brief background on jet injectors and potential applications in Power MEMS devices. It also compares a model derived from first principles inclusive of losses to experimental results for a single-stage jet injector tested at two length scales. Detailed derivations appear in Appendix B (p. 127).

### 3.1 Motivation

Several Power MEMS devices require liquid pumping at the microscale. Micro heat engines [1, 4, 5, 9–11, 13, 15–17, 19, 21–23, 25–27], rockets [1–3, 5, 8, 12, 14, 39, 49–52] and lasers [54–56] all require some form of pressurized liquid transport. For applications which either require or are able to incorporate a boiler or decomposition chamber, vapor driven jet injectors can satisfy liquid pumping requirements. Mechanically driven pumps are often difficult to implement at the microscale [43–46] because of comparatively small rotor-to-stator clearances (typically on the order of a few microns [4, 16, 25]) and high operating speeds [4, 15, 16, 21, 25]. Jet injectors require no moving parts [47, 70, 71, 73] and can thus tolerate comparatively poorer tolerances than high-speed pumping turbomachinery.

## 3.2 Background and Literature Search

### 3.2.1 Power MEMS Applications

#### *Microrocket*

One Power MEMS jet injector application currently being considered is a jet injector-pumped microrocket propulsion system that require only a static structure [49–53]. In these applications, motive vapor can be generated by catalytic decomposition of a propellant, or through regenerative cooling in the rocket nozzle, as shown in Figure 1.25 (p.30).

Micro turbopumps were designed into microrocket systems to deliver pressurized liquid propellants in early microrocket work, [12, 14, 39]. Since they are turbomachines, turbopumps have design constraints similar to micro compressors or turbochargers, [4, 15, 21], in that they require high-tolerance rotating components capable of sustaining high-speed operation required to maintain on-design tip speeds at the microscale, discussed in Chapter 1. Injector-pumped microrocket designs satisfy pumping requirements through use of non-rotating components and thus require only a static structure [49–53].

#### *Microengines: Rankine cycle and combined cycle*

Jet injectors can also find use in Rankine (vapor) cycle engines and engines operating with combined cycles. These applications require delivery of pressurized liquid phase working fluid to a boiler that generates vapor [10, 13, 17, 26, 27, 32, 48], examples of which are shown in Figures 1.21 (p.26) and 1.22 (p.27). A combined cycle variant, shown in Figures 1.23 (p.28) and 1.24 (p.29), has similar requirements since combined cycles are commonly built by having a Brayton (air) cycle ‘top’ a Rankine (vapor) cycle [29, 61, 91]. Jet injectors can satisfy liquid pumping requirements in a Rankine cycle or combined cycle without the use of high-speed pumping

turbomachinery or other mechanically-driven pumps.

### *3.2.2 Macroscale Applications*

Macroscale applications of injectors include the process industry and nuclear power generation [92–94]. Cattadori has proposed using a steam driven injector in advanced light water reactors for high pressure water supply [92]. His work compares different injector designs against a reference application of an injector used as a high pressure safety injection system in a boiling water reactor and argues the use of injectors to satisfy the high pressure core coolant requirements for next generation pressurized water reactors [92].

Ohmori has proposed use of a liquid-core steam injectors that operate using extracted exhaust steam from turbines in advanced boiling water reactors [93]. The injectors supply feedwater to boilers, and they also eliminate the need for heat exchangers to pre-heat the feedwater since injectors themselves exchange heat between vapor and liquid phases. The proposed design maintains overall plant thermal efficiency while removing low-pressure feedwater heaters [93].

Deberne presents simulation results and an empirically driven correlation for a liquid core steam driven injector used in nuclear power generation applications [94]. The correlation includes modeling of the condensation shock that occurs in the mixing region and is shown to be in agreement with experimental results [94]. The work suggests using the assumption that static pressure varies linearly within the combining cone between the inlet and outlet, as opposed to assuming constant static pressure.

### *3.2.3 Early Work and Theory*

Jet injectors first appeared in the mid 1800's and were widely adopted in the field of steam locomotion, where they served as the primary method for delivering feedwater

into boilers for over a century [47, 70, 71, 73]. The eponymous vapor-driven Giffard jet injector was first developed by Henri Giffard in 1859 [70] and quickly found widespread use in steam locomotives, replacing mechanical pumps for the pumping of feedwater into boilers [47, 71, 73]. Unlike their mechanical counterparts, Giffard injectors feature no moving parts. Instead, saturated steam tapped from the very boiler fed by the injector is passed through a series of converging and diverging tubes, where it condenses into, and exchanges momentum with, a liquid secondary flow drawn from a tank, or tender. The resulting warm, high-momentum liquid discharge stream is diffused into a high static pressure and fed into the boiler, at or slightly above boiler pressure. Several patents and works followed Giffard's original work [71, 73, 95]. Kneass provides background of the history, development, theory and practice of steam injectors circa 1900, and he also presents his experimental results for a Sellers-type injector [71].

### 3.3 Objective

The work presented in Chapter 3 demonstrates the feasibility of using vapor-driven jet injectors to either substitute or supplement microscale pumping turbomachinery. Microscale jet injectors can meet the liquid pumping requirements of Power MEMS devices and can serve as a viable substitute for turbopumps [49–53]. Chapter 3 reports on experiments performed on microscale injectors at two length scales with motive nozzle throat diameters of  $187\mu m$  and  $733\mu m$ . A theoretical model is developed from first principles in Appendix B (p.127) that includes viscous losses and blockage due to pronounced boundary layer growth at low Reynolds numbers or small length scales. The model further predicts a minimum injector size with a throat diameter of  $2\mu m$  which corresponds to a maximum achievable power density on the order of  $9.3MW/L$ .

## 3.4 Theory and Modeling

### 3.4.1 Physical Description

The simplest injector consists of three parts: (1) a motive nozzle, where the motive vapor is accelerated to a high speed; (2) a combining cone, where the high-speed motive vapor is mixed with the nearly quiescent suction liquid and the vapor is fully condensed; and (3) a delivery cone, or diffuser, where the resulting high-momentum liquid discharge flow is decelerated to recover the dynamic head as static pressure [47, 70, 71, 73]. Figure 3.1 (p.68) shows an illustration of typical components and flow configuration within an injector. A properly designed injector is able to pump liquid at or above the boiler which supplies motive vapor to the injector.

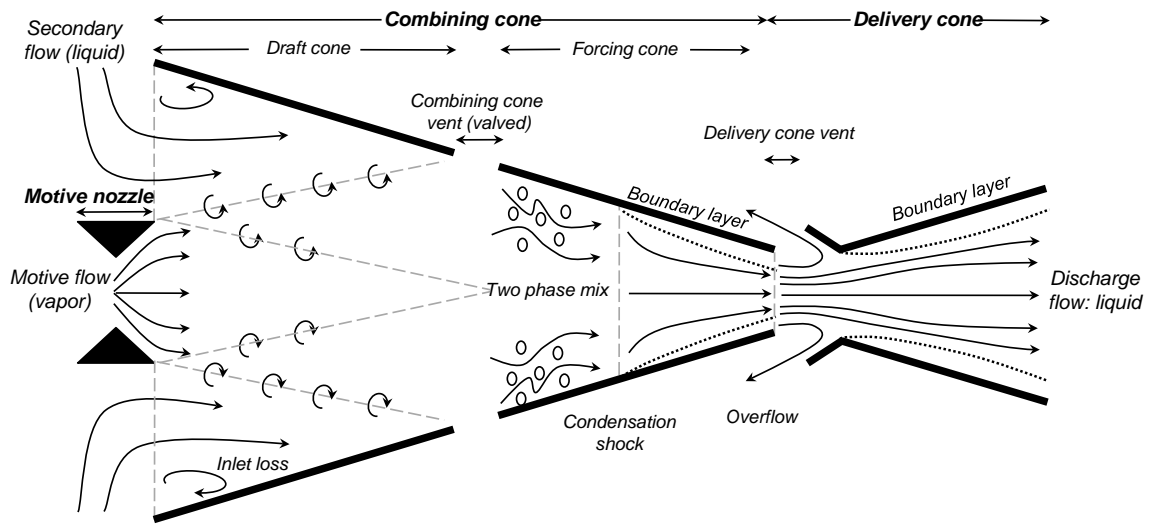


FIGURE 3.1: Schematic of the injector test piece, showing the motive nozzle, combining cone and flow paths

### *Motive nozzle*

The motive nozzle uses a converging-diverging geometry to achieve supersonic velocities. The high-motive fluid velocity supplies momentum to the secondary fluid which ultimately recovers into static pressure [70, 71, 73]. In order to function properly, the motive vapor must fully condense, as the resulting reduction in density assists in ‘lifting’ the secondary fluid into the injector, which is ultimately pressurized through the conversion of the motive vapor velocity into static pressure in the diffuser or delivery cone. Additionally, the expanded motive flow will be unable to flow through combining cone throat since it’s area typically equal to or smaller than the critical flow area in the motive nozzle. High-momentum vapor ultimately enables the pressurization of the secondary fluid, so converging-diverging nozzle geometries are used in order convert the motive total pressure into high velocity.

### *Combining cone*

Inside the combining cone, the motive jet initially entrains the surrounding fluid by viscous interaction. Phase change occurs at the boundary between the vapor and the surrounding liquid, leading to a concurrent reduction in vapor volume (steam at 1 atm and  $100^{\circ}C$  occupies over 1,600 times more volume than water at  $100^{\circ}C$  [96]). A properly designed combining cone will contract in diameter to accommodate this volume change, allowing constant static pressure mixing. Eventually, the motive vapor fully condenses and the vapor core disappears. The condensation process releases latent energy associated with expanding the liquid to vapor, and this energy release is realized as an increase in the velocity of the entrained liquid, allowing the delivery stream to be injected at total pressures equal to, or even greater than, the motive vapor supply pressure [47, 70, 71, 73].

### *Delivery Cone (diffuser)*

The combining cone discharges across a gap, which serves as an overflow vent during the startup process, and into the delivery cone, or diffuser, where the high-velocity stream diffuses and travels into the boiler. A properly-designed delivery cone, with an appropriate compound taper, will diffuse the high-speed liquid discharge stream with minimal pressure loss.

#### *3.4.2 Typical Injector Geometry*

The values presented below for typical injector geometries are adapted from [71, 73] and represent average values taken from several variations of steam injectors seen in practice. These values correspond to those used in the model in Section 3.1 (71) and are represented in Figures 3.2 (p.70).

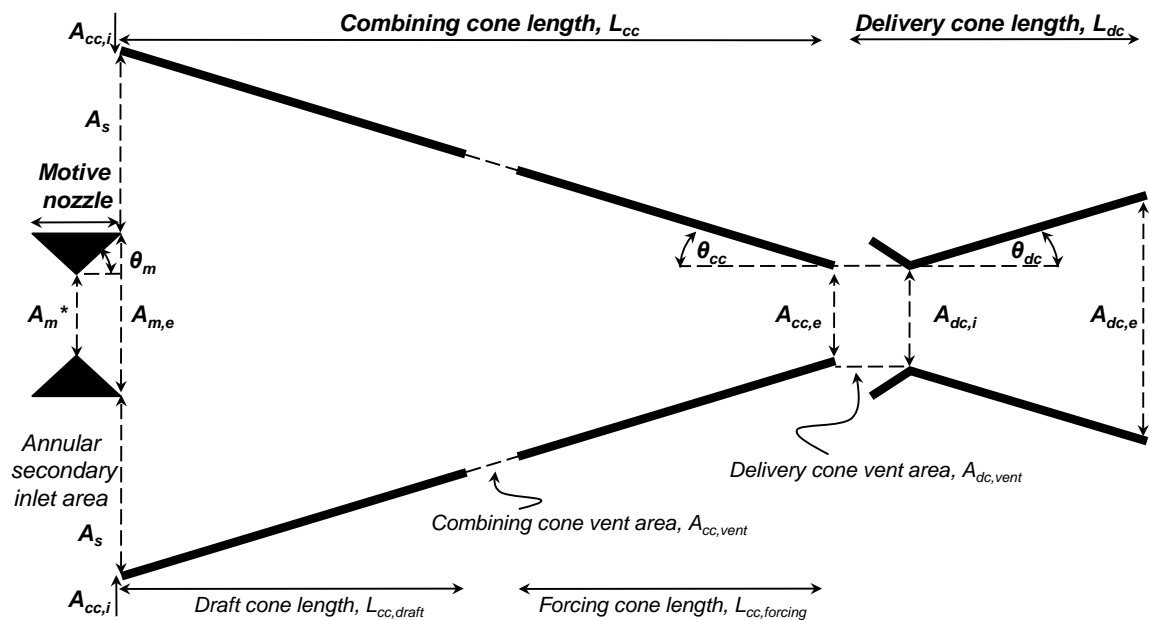


FIGURE 3.2: Injector nomenclature

*Area ratios*

Table 3.1: Typical injector area ratios, adapted from [71, 73]

| <i>Area Ratio</i>      |                  |                |
|------------------------|------------------|----------------|
| <i>Secondary Inlet</i> | $A_s/A_m^*$      | $3.9 \pm 20\%$ |
| <i>Combining Cone</i>  | $A_m^*/A_{cc,e}$ | $1.5 \pm 8\%$  |
| <i>Delivery Cone</i>   | $A_m^*/A_{dc,i}$ | $2.2 \pm 6\%$  |

The most critical area ratio in injector design is the ratio of the motive nozzle throat area to the minimum discharge flow area in mixing region,  $A_m^*/A_d$ . The typical minimum area is the delivery cone throat area,  $A_{dc,i}$ , giving  $A_m^*/A_d \Rightarrow A_m^*/A_{dc,i}$ . For cases when the delivery cone is not installed and the injector operates with only the combining cone, this minimum area is the combining cone throat area,  $A_d \Rightarrow A_{cc,e}$ . As will be shown in Section 3.4.4, this area ratio multiplied by the motive nozzle thrust coefficient,  $C_{F,m}$ , has the greatest impact on injector performance since the other terms are higher order by comparison. For this reason, the range of values seen in practice for this area ratio is small by comparison, as shown in Table 3.1 (71).

Another critical area ratio is the ratio of the secondary flow inlet area to the motive nozzle exit area, or throat area given a fixed nozzle expansion ratio,  $A_s/A_m^*$ . This area ratio controls the entrainment ratio and can be used to restrict secondary fluid flow. The nozzle exit plane's axial position within the combining cone is not as critical to injector performance as some of the other area ratios [73]. However, if the nozzle exit plane position can be adjusted, manufacturing errors which can mildly affect performance through influencing the secondary flow inlet area to motive nozzle throat area,  $A_s/A_m^*$ , may be corrected through adjustment of the nozzle exit plane axial position. However, the ability to adjust this position at the microscale may be overly complex. Thus, any benefits from adjustability may introduce too much complexity and make this feature an impractical design trade.

*Expansion / contraction ratios and half-angles*

Table 3.2: Typical injector expansion/contraction ratios, adapted from [71, 73]

| <i>Expansion/Contraction Ratio</i>              |                     |                |
|---|---------------------|----------------|
| <i>Motive Nozzle, <math>\epsilon</math></i>     | $A_{m,e}/A_m^*$     | $2.5 \pm 10\%$ |
| <i>Combining Cone, <math>\kappa_{cc}</math></i> | $A_{cc,i}/A_{cc,e}$ | $10 \pm \%$    |
| <i>Delivery Cone, <math>\kappa_{dc}</math></i>  | $A_{dc,e}/A_{dc,i}$ | $9 \pm \%$     |

The motive nozzle expansion ratio,  $\epsilon$ , dictates the exit velocity discharging into and ultimately pressurizing the secondary fluid. It also sets the exit plane static pressure of the jet, which is ideally matched to the static pressure of the surroundings [36]. For the injector, this static pressure is set by the total pressure of the secondary fluid,  $P_{t,s}$ , for most cases where the secondary fluid velocity entering the combining cone is negligible. The secondary fluid static pressure,  $P_s$ , can be computed using conservation of mass, momentum and energy in the form of the incompressible Bernoulli equation if the entrainment ratio, or ratio of secondary mass flow to motive mass flow, can be approximated. Ideally, the nozzle will be matched to a certain operating point (or motive total pressure) since it will operate off-design at all other points for a fixed expansion ratio. Multi-staging or adjustable expansion ratios are more complex alternatives that could be used in situations requiring efficient design across multiple operating points.

Typical values for the contraction ratio of the combining cone,  $\kappa_{cc}$ , and expansion ratio of the delivery cone,  $\kappa_{dc}$ , were computed using other typical values for area ratio and length-to-diameter ratio and half-angle listed in [71, 73]. The contraction ratio of the combining cone assists in momentum exchange between the motive and secondary fluids, as well as condensation of the motive fluid. It also suppresses boundary layer losses in the combining cone by imposing a favorable pressure gradient and accelerating flow. The expansion ratio of the delivery cone diffuses kinetic energy of the high-speed jet into static pressure. Since the delivery cone operates with an adverse

pressure gradient, a low expansion angle is used to prevent flow separation from the walls in avoidance of losses [29, 30, 37, 83]. This adverse pressure gradient does not suppress boundary layer growth, which can significantly displace flow area at low Reynolds numbers. Also, efficient diffusers are typically challenging to implement at the microscale in part due to the limitations imposed by using 2-D planar fabrication techniques, which limits some common options used at the macroscale such as 3-D variation of flow passages [16].

Table 3.3: Typical injector half-angles, adapted from [71, 73]

| <i>Half – Angle</i>   |               |           |
|-----------------------|---------------|-----------|
| <i>Motive Nozzle</i>  | $\theta_m$    | 4.5 ± %   |
| <i>Combining Cone</i> | $\theta_{cc}$ | 4.5 ± 80% |
| <i>Delivery Cone</i>  | $\theta_{dc}$ | 3 ± %     |

The low half-angle listed below for the motive nozzle is conservative compared to typical rocket nozzles [36] and can likely be increased without excessive penalty to injector performance. The injector is also fairly insensitive to the combining cone half-angle, provided that adequate mixing occurs. The combining cone half-angle,  $\theta_{cc}$ , is typically around 4.5° but is listed as varying between 2.5° – 8.5° [73]. Compound tapers have been used which feature steps from 6° to 3.75° to 3°. One account notes that a steeper angle of 8.5° performs better at lower motive vapor pressures [73]. For reasons listed in the preceding paragraph regarding diffusers, the delivery cone half-angle  $\theta_{dc}$  requires a more conservative lower value in comparison to the motive nozzle and combining cone in order to prevent separation losses.

#### *Length-to-diameter ratios*

The motive nozzle length-to-diameter ratio does not tend to adversely affect performance within a range of roughly 15° – 40° [3, 36]. However, at low Reynolds numbers, boundary layers will become thicker and displace flow area at larger  $L/D$  values. This blockage materially decreases performance and in some cases prevents normal

Table 3.4: Typical injector length-to-diameter ratios, adapted from [71, 73]

| <i>Length – to – Diameter Ratio</i> |              |               |
|-------------------------------------|--------------|---------------|
| <i>Motive Nozzle</i>                | $L/D_m^*$    | $3.8 \pm \%$  |
| <i>Combining Cone</i>               | $L/D_{cc,e}$ | $15 \pm 80\%$ |
| <i>Delivery Cone</i>                | $L/D_{dc,e}$ | $19 \pm \%$   |

operation. The combining cone length-to-diameter ratio must be great enough to allow complete condensation of the motive vapor and mixing with the secondary fluid in order to accelerate and pump it up to boiler pressures. As long as this condition is met, injector performance is fairly insensitive to variations in  $L/D_{cc,e}$ . The delivery cone length-to-diameter ratio also has potential to affect performance by diffuser separation losses via the expansion half-angle but is otherwise insensitive to variations.

### *Vents*

Typical self-acting injectors feature two vents, a primary vent placed roughly in the middle of the combining cone and a vent placed between the combining cone and delivery cone to assist during startup. The vent areas are sized to be approximately equal to a desired flow area in order to allow the complete escape of vented fluid. In general, smaller vent widths promote improved performance during normal operation but larger vents ease the starting process [71, 73].

Table 3.5: Typical combining cone primary vent geometry, adapted from [71, 73]

| <i>Primary Vent Geometry</i> |                      |                      |
|------------------------------|----------------------|----------------------|
| <i>Area Ratio</i>            | $A_{vent,cc}/A_m^*$  | $\approx 1$          |
| <i>Vent Width</i>            | $w_{vent,cc}/D_m^*$  | $\approx 0.7 - 1.27$ |
| <i>Axial Location</i>        | $X_{vent,cc}/L_{cc}$ | $\approx 0.4 - 0.5$  |

The combining cone central vent is typically located at an axial distance roughly  $0.4 - 0.45 (L/D)_{cc}$ , or  $X_{vent,cc}/L_{cc} \approx 0.5$  from the vapor input side [73]. The vent area should be sized such that the expanded motive vapor can exit freely in the absence of any condensation from secondary fluid. For the case when the vent is located

roughly at the combining cone’s axial midpoint, the width of the vent is typically  $w_{vent,cc}/D_m^* \approx 0.7-1.27$ , where the larger values reduce the chances of backflow. This vent is typically valved such that, during normal operation, the suction generated from condensation of the motive vapor is not lost. A simple check valve can be made using a ball and a seat, such that the ball seals when drawn into its seat due to suction created from condensation, or it can float upwards during venting [73]. This scheme is probably not practicable using MEMS fabrication techniques, but other valves and similar mechanisms have been investigated and fabricated at the microscale in silicon [16]. Larger vent sizes are favorable to ensure that there is no backflow of vapor into secondary liquid supply should interruption occur, but otherwise small gap sizes are favorable [73]. Some designs make use of a two-piece combining cone in order to accomodate a vent, whereby alignment of the upstream draft cone and downstream forcing cone becomes important in effort to avoid sharp steps which incur additional hydrodynamic losses. Instead of using a two-piece combining cone, it is probably preferable to fabricate small channels that allow venting fluid to flow out radially in a series or pair of small channels. This configuration could be implemented using MEMS fabrication techniques, and it is also seen in practice on Penberthy injectors, which feature several radially-drilled holes in the combining cone which serve as the primary overflow vent.

Table 3.6: Typical delivery cone starting vent geometry, adapted from [71, 73]

| <i>Starting Vent Geometry</i> |                                     |
|-------------------------------|-------------------------------------|
| <i>Area Ratio</i>             | $A_{vent,dc}/A_{vent,cc} \approx 1$ |
| <i>Vent Width</i>             | $w_{vent,dc}/D_{cc,e} \approx 1/4$  |

The delivery cone vent located between the combining cone and delivery cone is also referred to as the starting vent or gap [73]. This vent’s primary purpose is to allow for an easy startup process. During startup, the discharge fluid that is not at or above boiler pressure will escape through this vent rather than flowing backwards or

stagnating. Thus, the area of this vent is sized to have the same area as the combining cone throat area,  $A_{vent,dc} = A_{cc,e}$ . This gives a vent width of  $w_{vent,dc}/D_{cc,e} \approx 1/4$ . The axial location of the vent is set by the combining cone length, half-angle and desired starting vent width.

### 3.4.3 Model Approach

The injector model develops from first principles, applying the conservation of mass and momentum across a converging mixing duct and assuming compressible flow through the motive nozzle and incompressible flow through the combining cone for a single stage axial flow configuration shown in

In Figures 3.3 (p.77),  $A_{m,e}$  represents the motive nozzle exit area. It should be noted that in the model the  $e$  subscript has been dropped,  $A_{m,e} \Rightarrow A_{m,e}$ . The secondary flow area,  $A_s$ , is computed by taking the difference between the combining cone inlet area,  $A_{d,i}$ , and motive nozzle exit area,  $A_s = A_{d,i} - A_{m,e}$ . Note that in the model this  $e$  subscript has also been dropped for the combining cone exit area,  $A_{d,e} \Rightarrow A_d$ .

In practice, the axial position of the nozzle exit plane within the combining cone inlet can be used to restrict secondary flow and is typically set to approximately  $0.5D_m^*$  but can range between  $0.1D_m^* - 0.9D_m^*$  [70, 71, 73]. The model includes secondary flow inlet losses and viscous losses through the motive nozzle and combining cone, including flow area restriction due to displacement boundary layer growth. A detailed derivation of this model appears in Appendix B. The conservation of mass, momentum and energy establishes expressions for entrainment ratio and injector pressure ratio. For the design considered below, we assume an arbitrary supply, or tank, total pressure,  $P_{t,s,tank} = P_{t,s,us} = P_{t,s}$  for the secondary fluid.

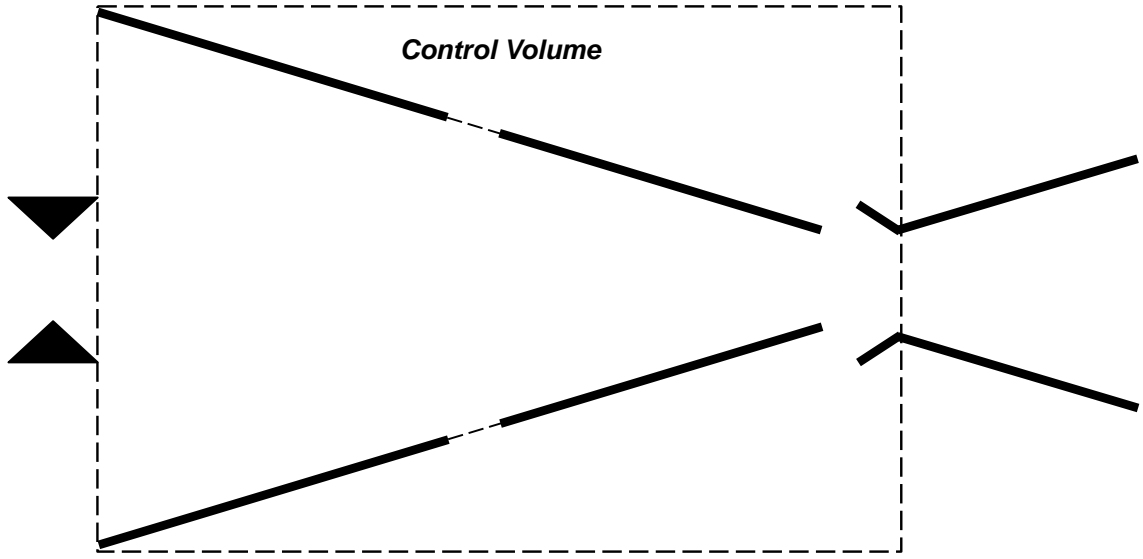


FIGURE 3.3: Schematic detailing the control volume used to develop the injector model

#### 3.4.4 Analytic Model

##### *Inviscid model*

In the absence of viscous losses, the following expression for injector discharge pressure results:

$$\begin{aligned} \frac{P_{t,d} - P_{t,s,us}}{P_{t,m}} &= \frac{C_F A_m^*}{2 A_d} + \frac{1}{2} C_d^2 \left[ \frac{3\kappa - 1}{4} - \epsilon \frac{A_m^*}{A_d} \right] \frac{P_{t,s,us} - P_s}{P_{t,m}} + \dots \\ &+ \left[ \frac{\kappa - 3}{4} \right] \frac{P_{t,s,us} - P_d}{P_{t,m}} \end{aligned} \quad (3.1)$$

Equation (3.1) may also be expressed as

$$\begin{aligned}
\frac{P_{t,d} - P_{t,s}}{P_{t,m}} &= \frac{C_{F,m} A_m^*}{2 A_d} + \dots \\
&+ \frac{1}{2} \frac{\rho_s u_s^2}{P_{t,m}} \left( \frac{A_s}{A_d} - \frac{1}{C_d^2} \right) + \dots \\
&+ \frac{P_d - P_s}{P_{t,m}} \left[ 1 - \frac{1}{4} \left( 1 + \frac{A_s}{A_d} \left( 1 + \frac{A_{m,e}}{A_s} \right) \right) \right]
\end{aligned} \tag{3.2}$$

As this result shows, the discharge dynamic head from an injector's combining cone is proportional to the total pressure of the supplied motive vapor, the thrust coefficient of the motive nozzle, and the ratio of the motive nozzle throat area to the combining cone throat area. Since the thrust coefficient is typically between 1 – 2 [36], this term will be the most significant term in terms of model performance. In principle, any discharge total pressure can be achieved so long as there is adequate thermal capacity in the suction flow to permit complete condensation of the motive vapor. Higher motive total pressures require colder secondary fluids by the conservation of energy for a fixed entrainment ratio.

#### *Minimum entrainment ratio*

We can estimate the minimum entrainment ratio required to achieve condensation of the motive vapor by using the conservation of mass and conservation of energy. Assuming negligible heat transfer to the walls of the combining cone, the conservation of energy across the combining cone gives

$$\dot{Q}_{in} = \dot{Q}_{out} \tag{3.3}$$

where

$$\dot{Q}_{in} = \dot{m}_m h_{vap} + \dot{m}_m c_{p,s} T_{sat} + \dot{m}_m c_{p,m} T_m + \dot{m}_s c_p T_s \tag{3.4}$$

Since most of the motive vapor will be fully condensed, the discharge fluid specific heat will approximately equal to that of the secondary fluid,  $c_{p,d} \approx c_{p,s} = c_{p,liquid}$ . The heat transfer rate leaving the control volume will be, in the absence of heat transfer to the walls,

$$\dot{Q}_{out} = \dot{m}_d c_{p,d} T_d = \dot{m}_m c_{p,s} T_d + \dot{m}_m c_{p,m} T_d + \dot{m}_s c_{p,s} T_d \quad (3.5)$$

Combining equations (3.4) and (3.5) gives

$$\dot{m}_m [h_{vap} + c_{p,m} (T_d - T_{sat}) + c_{p,s} (T_{sat} - T_d)] = \dot{m}_s c_{p,s} (T_d - T_{sat}) \quad (3.6)$$

Since the enthalpy of vaporization,  $h_{vap}$ , is large compared to  $c_{p,m}$  and  $c_{p,s}$ ,

$$h_{vap} \left[ 1 + \frac{c_{p,m} (T_d - T_{sat})}{h_{vap}} + \frac{c_{p,s} (T_{sat} - T_d)}{h_{vap}} \right] \approx h_{vap} \quad (3.7)$$

Thus, equation (3.6) can be approximated as

$$\alpha = \frac{\dot{m}_s}{\dot{m}_m} \approx \frac{h_{vap}}{c_{p,s} (T_d - T_s)} \quad (3.8)$$

Equation (3.9) represents the minimum entrainment ratio required for operation when the discharge pressure equals the saturation temperature at a given boiler pressure,  $T_d = T_{sat}$ . This entrainment ratio implies that no secondary cooling capacity remains and also corresponds to the maximum achievable injector discharge pressure.

$$\alpha_{min} = \frac{\dot{m}_s}{\dot{m}_m} \approx \frac{h_{vap}}{c_{p,s} (T_{sat} - T_s)} \quad (3.9)$$

The saturation temperature at a given pressure can be computed using a form of the Clausius-Clapeyron relation commonly referred to as the Clausius-Clapeyron equation

$$\ln\left(\frac{P'}{P_{STP}}\right) = \frac{h_{vap}}{R} \left(\frac{1}{T_{NBP}} - \frac{1}{T'_{sat}}\right) \quad (3.10)$$

where  $T_{NBP}$  is the ‘normal’ boiling temperature at a standard pressure  $P_{STP}$ .

### *Model with losses*

The onset of scale effects at low Reynolds numbers can be predicted using equation (3.2) if viscous losses are included. As outlined in Appendix B, viscous losses in the motive nozzle, combining cone, and delivery cone can be included to find the modified model, inclusive of losses, below.

Equation (3.1) can be expanded to include losses

$$\begin{aligned} \frac{P_{t,d} - P_{t,s,us}}{P_{t,m}} &= \left(\frac{C_{F,isen}}{2} - \frac{C_{f,m} + C_{f,cc}}{2}\right) \frac{A_m^*}{A_d} + \dots \\ &+ \frac{1}{2}C_d^2 \left[\frac{3\kappa - 1}{4} - \epsilon \frac{A_m^*}{A_d}\right] \frac{P_{t,s,us} - P_s}{P_{t,m}} + \dots \\ &+ \left[\frac{\kappa - 3}{4}\right] \frac{P_{t,s,us} - P_d}{P_{t,m}} \end{aligned} \quad (3.11)$$

$$\begin{aligned} \frac{P_{t,d} - P_{t,s,us}}{P_{t,m}} &= \frac{C_{F,isen}}{2} \frac{A_m^*}{A_d} + \dots \\ &+ \frac{3}{\cos \theta_m} CRe_{D_m^*}^{-m} \left(\frac{L}{D_m^*}\right)^{1-n} + \dots \\ &+ \frac{1/2\rho_m u_{m,e}^2}{P_{t,m}} \epsilon \frac{4CRe_{D_{m,e}}^{-m}}{\cos \theta_{cc}} \left(\frac{L_{cc}}{D_{m,e}}\right)^{1-n} \frac{1}{m+2} + \dots \\ &+ \frac{1}{2}C_d^2 \left[\frac{3\kappa - 1}{4} - \epsilon \frac{A_m^*}{A_d}\right] \frac{P_{t,s,us} - P_s}{P_{t,m}} + \dots \\ &+ \left[\frac{\kappa - 3}{4}\right] \frac{P_{t,s,us} - P_d}{P_{t,m}} \end{aligned} \quad (3.12)$$

Displacement boundary layer blockage can be included by using the effective area ratio,  $A_d/A_{d,eff}$  from equation 1.9. An alternate form of equation 3.12 which explicitly shows blockage terms is given as

$$\begin{aligned} \frac{P_{t,d} - P_{t,s}}{P_{t,m}} &\approx \left( \frac{C_{F,m,isen}}{2} - \frac{C_{f,m} + C_{f,cc} + C_{f,dc}}{2} \right) \frac{A_m^*}{A_d} \frac{A_d}{A_{d,eff}} + \dots \\ &\frac{1}{2} \frac{\rho_s u_s^2}{P_{t,m}} \left( \frac{A_s}{A_d} \frac{A_d}{A_{d,eff}} - \frac{1}{C_d^2} \right) \dots \\ &+ \frac{P_d - P_s}{P_{t,m}} \left[ 1 - \frac{1}{4} \left( 1 + \frac{A_s}{A_d} \frac{A_d}{A_{d,eff}} \left( 1 + \frac{A_{m,e}}{A_s} \right) \right) \right] \end{aligned} \quad (3.13)$$

$$\begin{aligned} \frac{P_{t,d} - P_{t,s}}{P_{t,m}} &\approx \frac{C_{F,m,isen}}{2} \frac{A_m^*}{A_d} \frac{A_d}{A_{d,eff}} + \dots \\ &- \frac{3}{\cos \theta_m} CRe_{D_m^*}^{-m} \left( \frac{L}{D_m^*} \right)^{1-n} + \dots \\ &- \frac{1/2 \rho_m u_{m,e,isen}^2}{\cos \theta_{cc}} 4 CRe_{D_m^*}^{-m} \epsilon_m \left( \frac{L}{D_m^*} \right)^{1-n} \frac{1}{(m+2)} + \dots \\ &+ \frac{1}{2} \frac{\rho_s u_s^2}{P_{t,m}} \left( \frac{A_s}{A_d} \frac{A_d}{A_{d,eff}} - \frac{1}{C_d^2} \right) + \dots \\ &+ \frac{P_d - P_s}{P_{t,m}} \left[ 1 - \frac{1}{4} \left( 1 + \frac{A_s}{A_d} \frac{A_d}{A_{d,eff}} \left( 1 + \frac{A_{m,e}}{A_s} \right) \right) \right] \end{aligned} \quad (3.14)$$

The constants  $C$ ,  $m$  and  $n$  are determined based on flow regime using Table B.1.

### *Magnitude of losses*

Figure 3.4 (p.82) illustrates the magnitudes of the different loss terms in equation (3.12) in comparison to the inviscid model given by equation (3.1) across different Reynolds number based on the motive nozzle throat diameter. The state variables used are listed below in Table 3.7 (p.82). The average geometries provided in Tables 3.1 (p.71), 3.2 (p.72), 3.3 (p.73), 3.4 (p.74) were used.

Table 3.7: Model inputs for loss magnitude plot

| <i>Station</i>            | <i>Input</i>       |
|---------------------------|--------------------|
| Motive total pressure     | $P_{t,m} = 10atm$  |
| Secondary total pressure  | $P_{t,s} = 1.1atm$ |
| Secondary static pressure | $P_s = 1atm$       |
| Discharge static pressure | $P_d = 1atm$       |

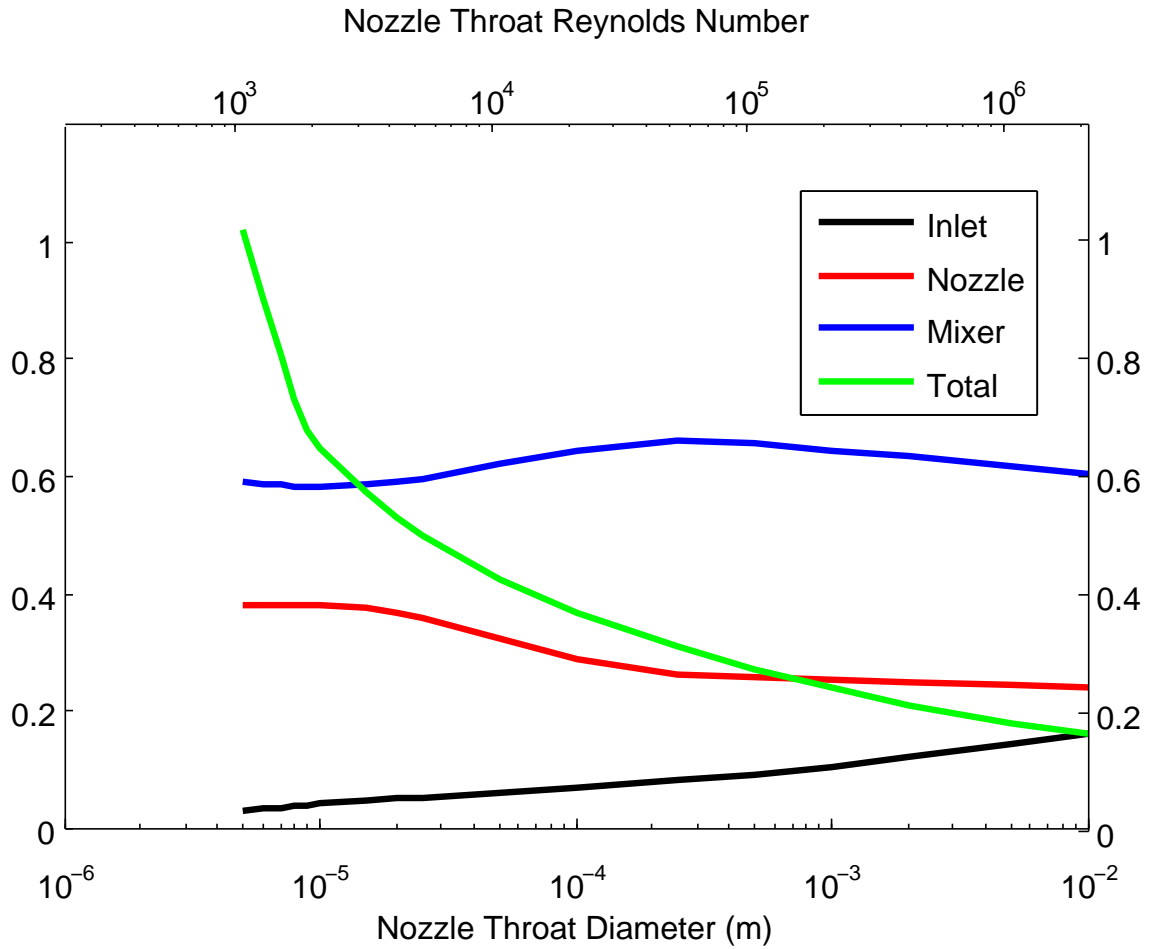


FIGURE 3.4: Magnitude of losses with respect to the inviscid model versus Reynolds number.

In effort to illustrate the relative magnitudes of the terms in equation (3.1), Table 3.8 (p.83) provides the magnitudes of the terms in equation (3.1) for the case of a  $10\mu m$  injector using the inputs and geometries given above.

Table 3.8: Characteristic magnitudes for terms in the injector model for the case of an injector with  $D_m^* = 10\mu m$  and  $Re_{D_m^*} = 2,132$

| <i>Term</i>                   | <i>Magnitude</i> |
|-------------------------------|------------------|
| Thrust coefficient term       | 1.42             |
| Nozzle skin friction          | 0.11             |
| Combining cone skin friction  | 0.17             |
| Secondary inlet loss          | 0.01             |
| Mixing pressure matching term | 0.02             |
| Inviscid model                | 1.43             |
| Loss model                    | 1.15             |

### 3.4.5 Efficiency

Since it is useful to compare injectors to turbopumps, an efficiency measure was chosen that represents the ratio of the power delivered to the suction flow to the power that could be extracted by isentropically expanding the motive vapor through a turbine, which is analogous to the spool efficiency of a turbopump. The injector pumping power,  $\dot{W}_{inj}$  is

$$\dot{W}_{inj} = \dot{m}_s \Delta P_s / \rho_s = \dot{m}_s (P_{t,d} - P_{t,s}) / \rho_s \quad (3.15)$$

If the motive vapor driving the injector were to instead expand isentropically through a turbine to the static pressure of the secondary fluid,  $P_s$ , the turbine power output would be

$$\dot{W}_{turb} = \dot{m}_m c_{p,m} T_{t,m} \left( 1 - (P_s / P_{t,m})^{(\gamma_m - 1) / \gamma_m} \right) - \dot{m}_m (P_{t,d} - P_{t,s}) / \rho_s \quad (3.16)$$

The last term in equation (3.16) results from the conservation of energy and the conservation of mass. Since the injector discharge includes the condensed motive

mass flow, which it pumps at the discharge total pressure,  $P_{t,d}$ , the analogous turbopump is required to pump both the secondary mass flow and the motive mass flow. This second term captures the work required to pump the condensed motive mass flow.

Using equations (3.15) and (3.16), the injector efficiency is defined and expressed as

$$\begin{aligned}\eta_{inj} &\equiv \frac{\dot{W}_{inj}}{\dot{W}_{turb}} \\ &= \alpha \frac{(P_{t,d} - P_{t,s})/\rho_s}{c_{p,m} T_{t,m} (1 - (P_s/P_{t,m})^{(\gamma_m-1)/\gamma_m}) - (P_{t,d} - P_{t,s})/\rho_s}\end{aligned}\quad (3.17)$$

In an injector with a delivery cone or diffuser, losses will be incurred by recovering the kinetic energy of the high speed discharge stream exiting the combining cone into static pressure across an adverse pressure gradient and diffuser of finite length.

#### 3.4.6 Power Density

Injector power density scaling laws may be predicted theoretically for a loss-free device. The injector volume is computed from

$$V = \frac{\pi}{4} D^{*3} [(L/D^*_m)_{nozzle} + (L/D)_{cc+dc} a^{3/2} \epsilon^{3/2}] \quad (3.18)$$

Combined with equation (3.15), equation (3.18) gives a non-dimensional power density of

$$\frac{\dot{W}/V}{1/2\rho u_{m,isen}^3} = \frac{1}{D^*} \alpha \frac{\Delta P}{1/2\rho u_{m,isen}^2} [(L/D^*_m)_{nozzle} \epsilon^{-1} + (L/D)_{cc+dc} a^{3/2} \epsilon^{1/2}]^{-1} \quad (3.19)$$

Therefore, in the absence of viscous losses, and ignoring scale dependence for the length-to-diameter ratios of the nozzle, combining cone, and delivery cone, the power

density of a given injector morphology scales with the inverse of its motive nozzle throat diameter. This trend will hold until viscous losses become overwhelming.

### 3.5 Experimental Approach

Figure 3.5 (p.86) depicts the experimental injector assembly, which consists of the motive nozzle and combining cone. Flow entered the converging combining cone through a radial-to-axial near-right-angle turn with a sharp corner that extended slightly into the secondary flow. For this configuration, Reference [90] recommends  $C_d = 0.8$ . In a complete implementation of the injector, a delivery cone would be installed and displaced from the exit plane of each combining cone by a small gap, which would serve as the primary overflow vent. However, the injector was operated without a delivery cone for all experiments reported here. Table 3.9 (p.85) provides the injector design geometries [50, 53].

Table 3.9: Comparison of design versus realized injector geometry

| Injector Design |     | Small<br>Actual | Medium<br>Actual | Large<br>Actual |
|-----------------|-----|-----------------|------------------|-----------------|
| $D_m^*$         | -   | $63\mu m$       | $187\mu m$       | $733\mu m$      |
| $\epsilon_m$    | 2.5 | 4.2             | 2.7              | 2.2             |
| $A_s/A_d$       | 9.7 | 18.8            | 14.9             | 3.9             |
| $A_m^*/A_d$     | 0.9 | 0.5             | 0.5              | 0.6             |

The motive nozzles were 1-D axisymmetric converging-diverging nozzles with a design expansion ratio of 2.5:1. Electrical discharge machining (EDM) was used to fabricate the nozzles in Figures 3.6 (p.87)(a)-(c) in stainless steel. The combining cones were machined using carbide drill bits from Drill Bit City (Chicago, IL) and a precision ground single-lip cutter. The combining cone was an axisymmetric converging cone with a nominal  $3^\circ$  taper half-angle, an inlet-to-exit area ratio  $\kappa$  of 12, and a nominal length-to-throat-diameter ratio,  $L/D_d$  of 24. Table 3.10 (p.86) provides comparison between the combining cone design and realized geometries [50, 53].

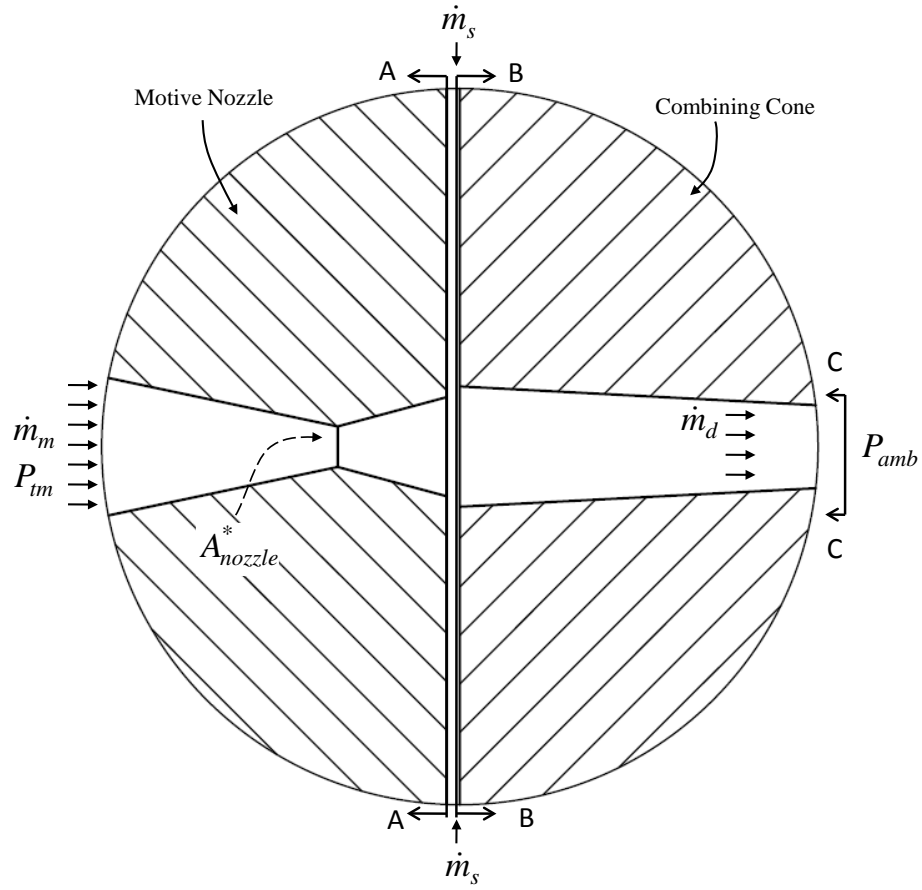


FIGURE 3.5: Injector assembly and flow paths [53]

Table 3.10: Comparison of design versus realized combining cone geometry

| Combining Cone Design |           | Small Actual | Medium Actual | Large Actual |
|-----------------------|-----------|--------------|---------------|--------------|
| $D_d$                 | -         | $89\mu m$    | $258\mu m$    | $990\mu m$   |
| $\kappa$              | 12        | 11.4         | 16.3          | 5.2          |
| $L/D_d$               | 24        | 17.7         | 17.8          | 18.2         |
| $\alpha_d$            | $3^\circ$ | $3.8^\circ$  | $4.9^\circ$   | $2.0^\circ$  |

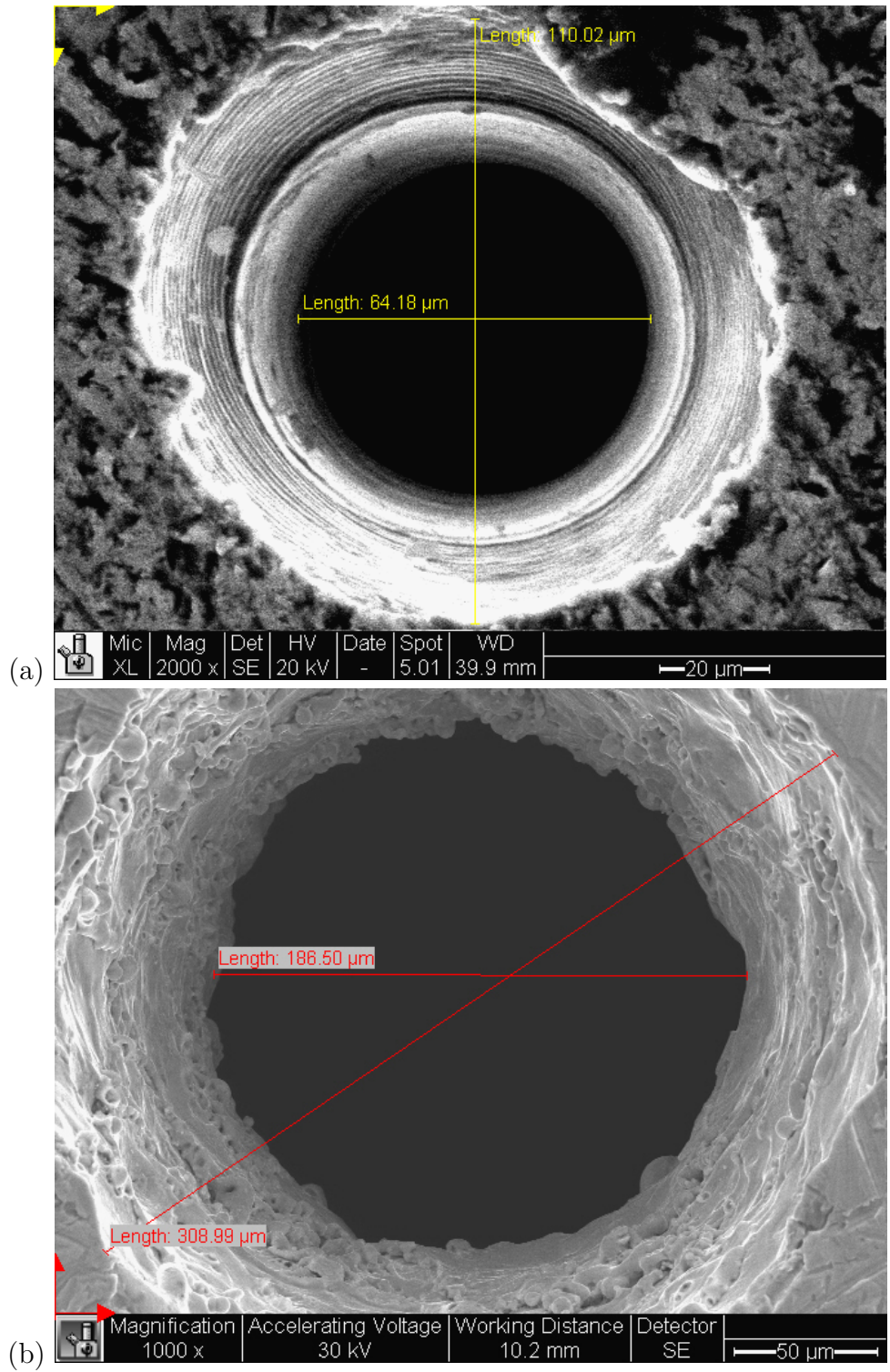
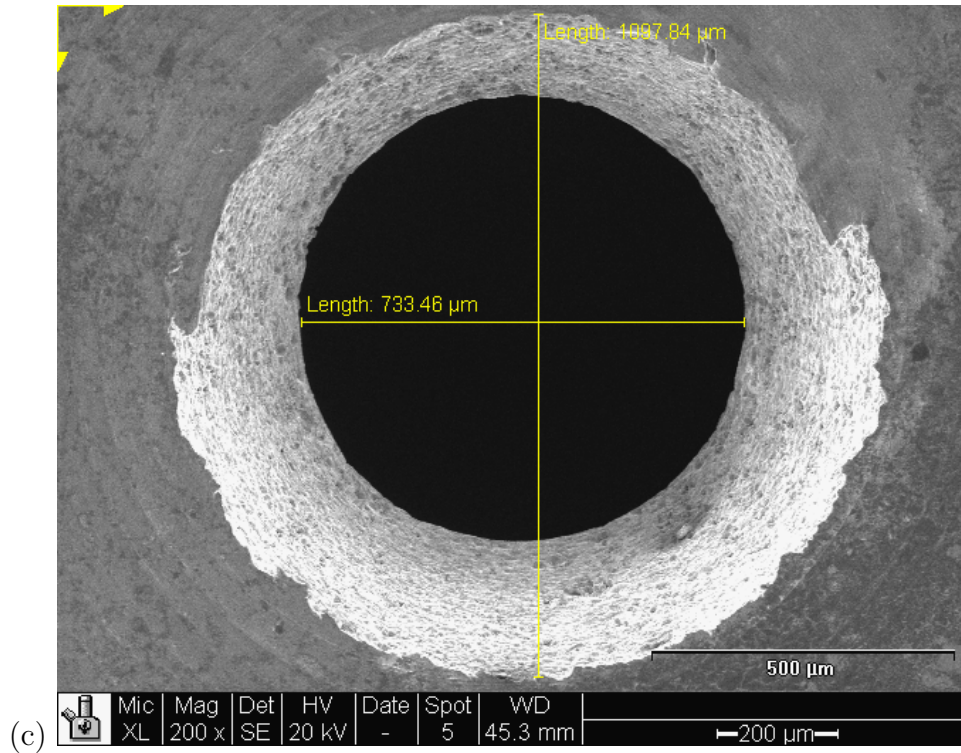


FIGURE 3.6: Realized geometry for ejector motive nozzles SEM images of (a) 64  $\mu\text{m}$  nozzle, (b) 187  $\mu\text{m}$  nozzle, (c) 733  $\mu\text{m}$  nozzle [31]



Injector performance tests were carried out using liquid ethanol and vapor, using the test rig shown in Figure 3.7 (p.89). A stainless steel boiler was heated to the desired temperature using an electric hot plate. An inline  $7\mu\text{m}$  filter placed directly upstream of the motive nozzle was used to avoid clogging the motive nozzle. The motive mass flow rate was computed using actual flow areas and measured state variables, in the same manner discussed in Chapter 2. All tests were performed with atmospheric backpressure. The smallest nozzle failed during tests– the thin web surrounding the nozzle features, required to minimize the plunge length-to-diameter ratio of the tooling, failed at elevated temperatures.

Injector operation was achieved as follows: (1) the boiler was filled cold, sealed, and heated using the hot plate to generate ethanol vapor at the desired supply pressure; (2) the suction inlet stopcock was then opened, allowing the suction liquid

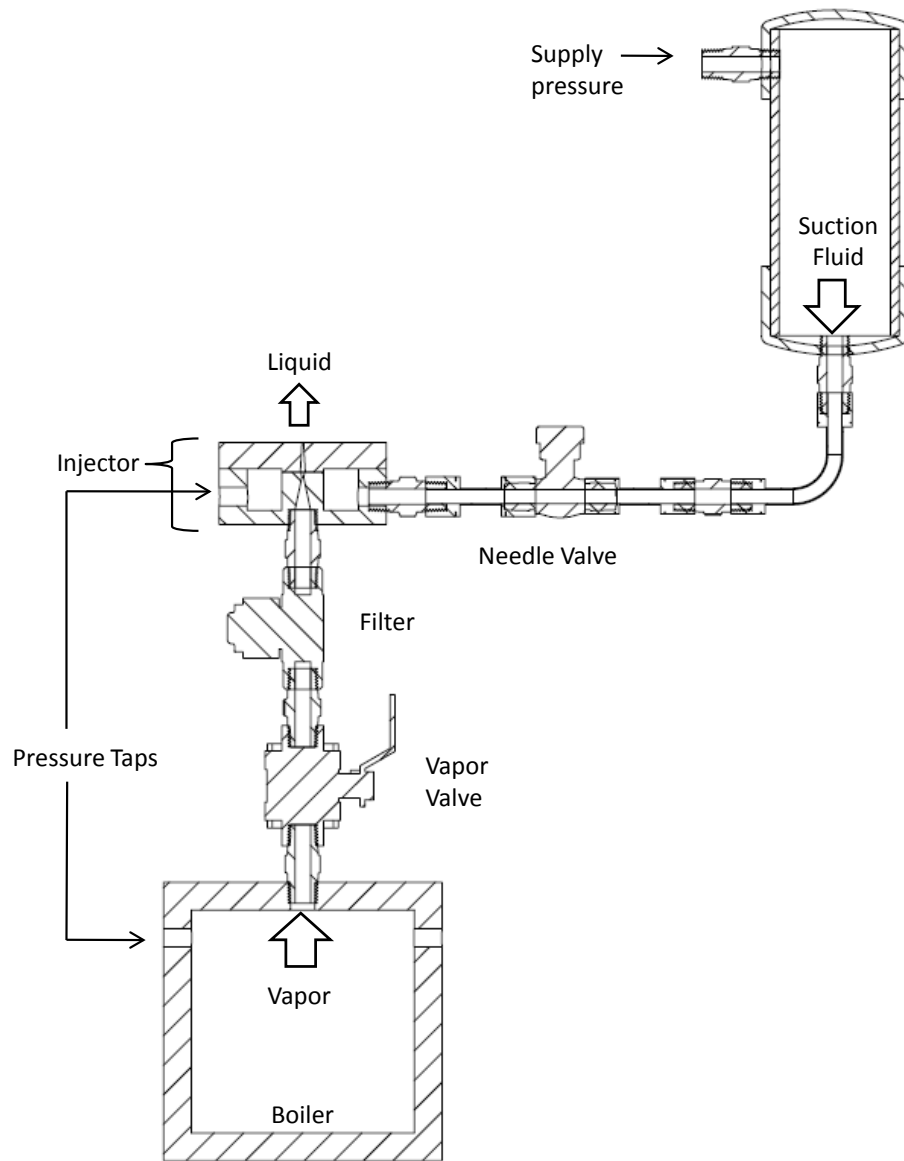


FIGURE 3.7: Experimental test rig. The boiler generates vapor that expands through the motive nozzle, entraining quiescent secondary liquid and discharging to atmosphere. Motive mass flow rates are computed based on measured upstream conditions and realized nozzle geometries, [50, 53]

to flow, priming the injector; (3) the motive vapor stopcock was opened, releasing the motive vapor into the motive nozzle and establishing stable operation.

To avoid overheating the injector, the suction flow was allowed to prime the injector before starting the motive vapor flow. Otherwise, the vapor would heat the combining cone and inhibit condensation, preventing successful operation of the device. It was also observed that an improper starting sequence would cause backflow into the suction supply because the combining cone throat was of similar size to the motive nozzle throat, causing the vapor shock to settle at the combining cone throat rather than the motive nozzle throat. In typical devices, the overflow vent, which is sized to have similar flow area to the motive nozzle throat [73], prevents backflow of vapor into the secondary inlet during startup.

Operation of the injectors was also assisted by allowing the motive nozzle to heat up slightly to avoid condensation within the nozzle. In the absence of pre-heating, the vapor-core flow configuration selected for the tested injectors will tend to have a nozzle wall temperature near the secondary fluid temperature due to the fact that secondary liquid bathes the nozzle structure. The presence of wall temperatures lower than the motive vapor, when coupled with the high heat transfer coefficients associated with small nozzle throat diameters, may facilitate heat transfer from the motive vapor sufficient to cause condensation of the motive nozzle flow, preventing proper device operating. For this reason, it is recommended that liquid-core injectors [93, 94] be considered for future microinjectors.

The stream exit pressure was measured by impinging the discharge stream against a cantilever beam, as shown in Figure 3.8 (p.91). The cantilever beam was fabricated from polypropylene using a laser cutter, which occluded the exit of the combining cone. The discharge dynamic pressure was computed from the observed beam deflection using beam theory [97] under the assumption of a point force applied at the point of impingement.



FIGURE 3.8: Injector test article showing beam used to compute dynamic pressure, [50, 53]

The beam theory results were validated against a finite element analysis performed in Solidworks, wherein a fixed restraint was applied at the bolted end of the beam, as shown in Figure 3.9 (p.92), and the same pressure was applied at the jet stream point of contact, with an area equal to the experimentally measured combining cone throat area. The beam theory and the finite element analysis results agreed to within 1%.

### 3.6 Experimental Results and Discussion

Figure 3.10 (p.93) reports the measured dynamic head at the discharge of the combining cone as a function of the motive supply pressure for a fixed suction liquid supply pressure of 1.3 atm. Ethanol vapor was used as the motive fluid and ethanol liquid, subcooled to  $270K$  with dry ice in an ethanol bath, was used as the suction liquid. All model data points are calculated using the design geometry given in Table 3.9

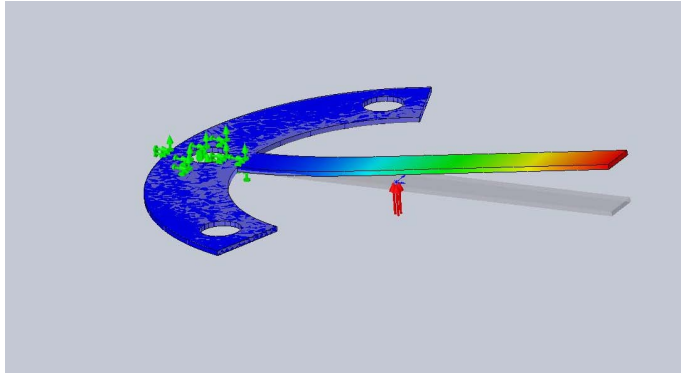


FIGURE 3.9: Injector test article showing beam used to compute dynamic pressure, [50, 53]

(p.85) and all experimental data are measured or computed using realized geometries and measured state variables.

The experimental results demonstrated operation consistent with theoretical predictions. In particular, the injectors delivered liquid at a total pressure in excess of the supply pressure inside of the boiler which drove it, making it self-acting and a suitable substitute for turbopumps or other mechanical pumps in Power MEMS applications, even at the lower uncertainty bound. Equation (3.14) predicts a theoretical peak power density near  $9.3MW/L$  for motive nozzle throat diameters of  $2\mu m$  and throat Reynolds numbers of 250, as shown in Figures 3.11 (p.94).

### 3.7 Conclusions

An ethanol-pumping micro-scale Giffard injector was tested at two length scales. Experimental results for the injector agree with a theoretical model inclusive of suction inlet restrictor losses and viscous losses in the motive nozzle and combining cone. Discharge total pressure rises of up to  $7.5atm$  were delivered from motive supply pressures of  $4.4atm$ , making the injector self-acting.

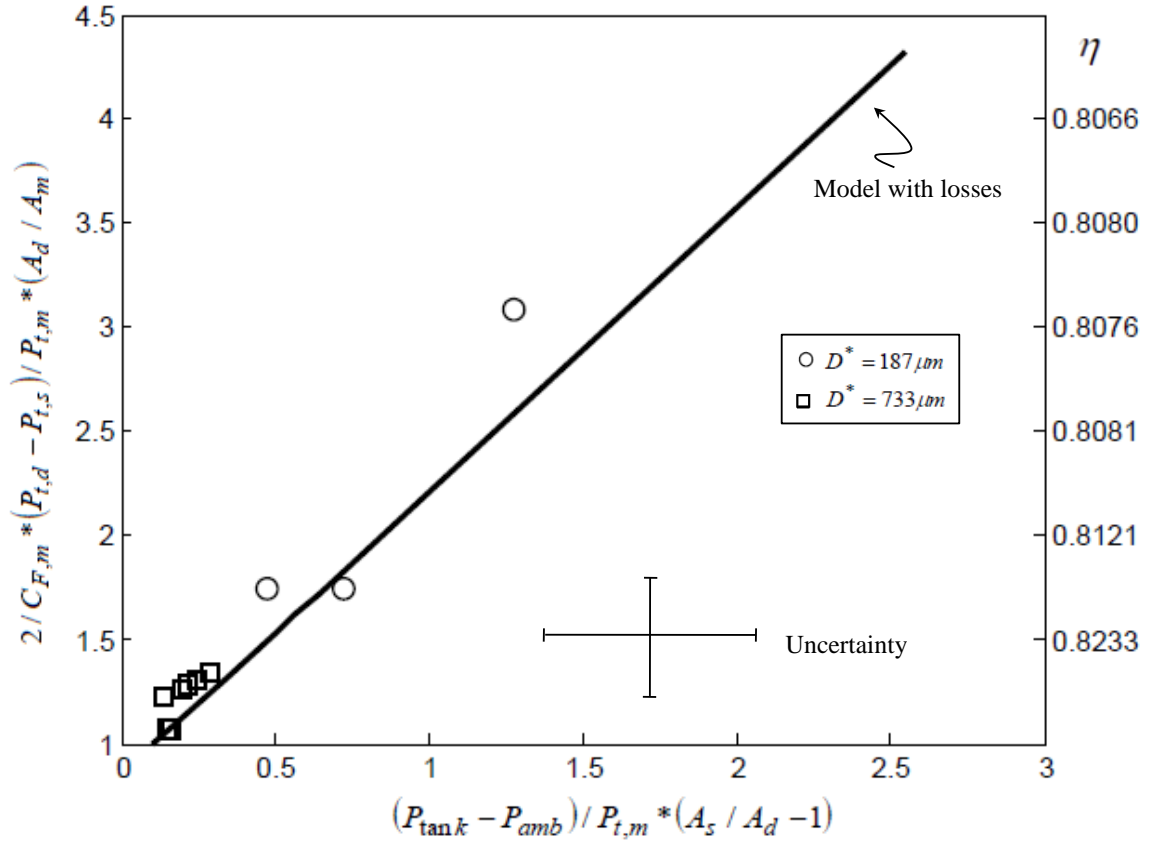


FIGURE 3.10: Nondimensional injector performance across different boiler pressures for ethanol vapor and liquid

The  $187\mu\text{m}$  injector achieved a power density of  $146\text{ kW/L}$  using only a static structure. Microscale turbopumps have achieved a reported power density of  $370\text{ W/L}$  [12]. The theoretical model presented here further suggests that a maximum power density of  $9.3\text{ MW/L}$ , corresponding to a nozzle throat diameter of  $2\mu\text{m}$  and a Reynolds number at the motive nozzle throat of 250, is possible with the present morphology and fluid supply conditions.

It is recommended that liquid-core injectors be considered for future micro jet injectors to avoid condensation of the motive vapor within the motive nozzle due to

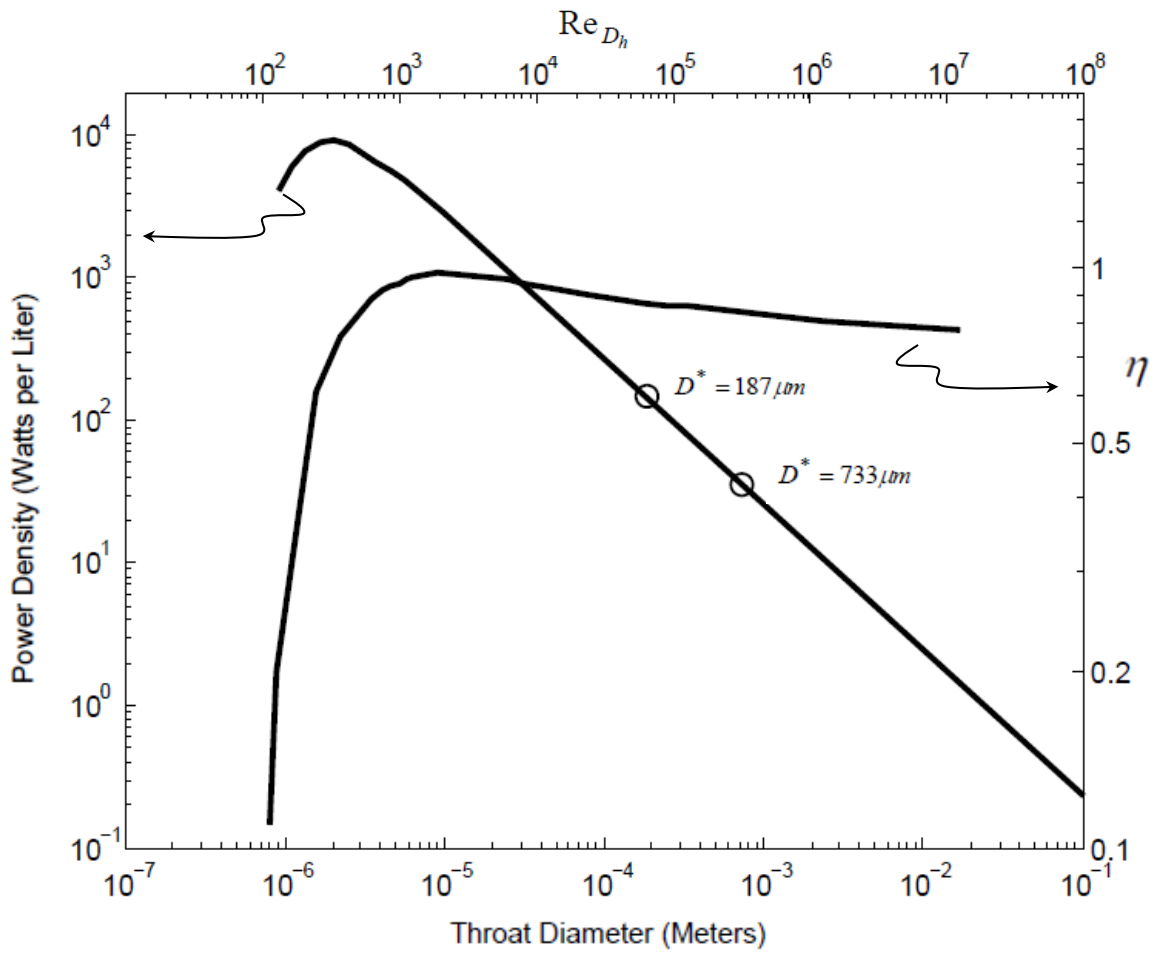


FIGURE 3.11: Injector power density and efficiency as a function of nozzle throat diameter

the comparatively large heat transfer coefficients experienced at small length scales.

## Multi-Stage Ejector

### 4.1 Motivation

This chapter provides a brief background on multi-stage ejectors and presents experimental data for a multi-stage ejector tested at three different length scales.

### 4.2 Background and Literature Search

Prior work has demonstrated that microscale single-stage jet ejectors can meet the gas pumping requirements of Power-MEMS devices [31, 48]. Investigators have also developed multi-staged lobed ejectors for thrust augmentation and heat signature suppression on turbofan and rotary wing aircraft [76]. The findings demonstrate improved efficiency over single-stage systems of the same area ratio, and for three-dimensional lobed mixer geometries, reduced mixing length requirements.

### 4.3 Objective

This chapter reports on experiments performed on microscale two-stage ejectors of similar geometry, which feature three different motive nozzle throat diameters of

$63\mu m$ ,  $187\mu m$  and  $733\mu m$ .

#### 4.4 Experimental Approach

The motive nozzle is a 1-D axisymmetric converging-diverging nozzle. The diverging section for the nozzle produces a design expansion ratio of 2.5:1. Table 4.1 (p.97) identifies the ejector design geometry, and Tables 4.2 (p.97) and Table 4.3 (p.97) compare this design geometry to the manufactured geometries for the nozzle and ejector assembly, respectively. Figure 4.1 (p.96) depicts the ejector assembly, which consists of the motive nozzle, primary and secondary mixers.

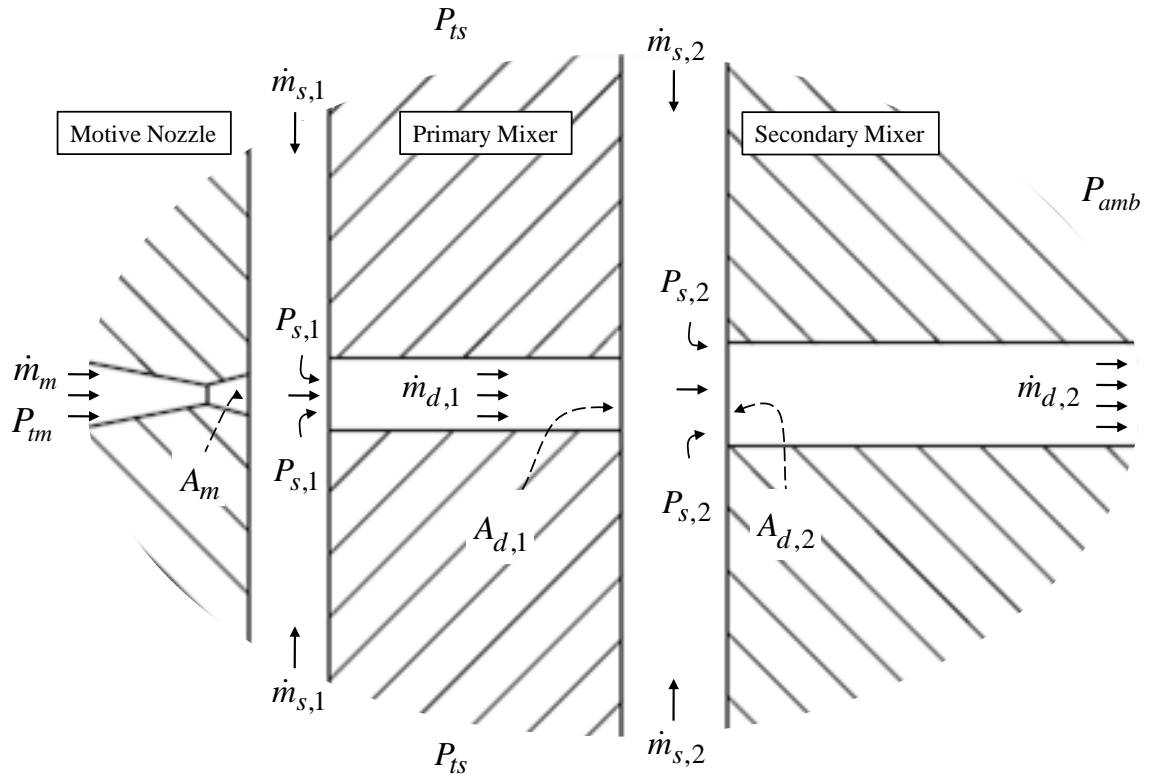


FIGURE 4.1: Schematic and nomenclature for a multi-stage ejector

Table 4.1 provides the ejector design geometries from Reference [98].

Table 4.1: Ejector design geometry

| Expansion ratio $\epsilon_m$ | Expansion angle $\alpha_m$ | Nozzle $L/D$ | Ejector area ratio $a$ | Mixer $L/D$ |
|------------------------------|----------------------------|--------------|------------------------|-------------|
| 2.5                          | 15°                        | 4.3          | 9                      | 4           |

Table 4.2 provides the motive nozzle design versus realized geometries from Reference [98].

Table 4.2: Comparison of design versus realized motive nozzle geometry

| Motive Nozzle | Design throat width $D_m^*$ | Design expansion ratio $\epsilon_m$ | Actual throat width $D_m^*$ | Actual expansion ratio $\epsilon_m$ |
|---------------|-----------------------------|-------------------------------------|-----------------------------|-------------------------------------|
| Small         | 50 $\mu m$                  | 2.5                                 | 64 $\mu m$                  | 4.2                                 |
| Medium        | 168 $\mu m$                 | 2.5                                 | 187 $\mu m$                 | 2.7                                 |
| Large         | 755 $\mu m$                 | 2.5                                 | 733 $\mu m$                 | 2.2                                 |

Table 4.3 provides the ejector design versus realized geometries from Reference [98].

Table 4.3: Comparison of design versus realized ejector geometry

| Motive nozzle exit diameter | Design ejector area ratio | Actual ejector area ratio |
|-----------------------------|---------------------------|---------------------------|
| 129 $\mu m$                 | 9                         | 7.6                       |
| 309 $\mu m$                 | 9                         | 9                         |
| 1097 $\mu m$                | 9                         | 9                         |

Using the notation from Figure 4.1 (p.96), we define the total entrainment ratio as the ratio of the sum of suction mass flows to the motive mass flow.

$$\alpha \equiv \frac{1}{\dot{m}_1} \sum_n \dot{m}_{s,n} \quad (4.1)$$

Using  $A_d = A_m + A_s$  for each stage, we define the total ejector area ratio, which can also be expressed as a product of the stage-wise area ratios.

$$a \equiv \frac{A_{d,2}}{A_{m,1}} = \left(1 + \frac{A_{s,1}}{A_{m,1}}\right) \left(1 + \frac{A_{s,2}}{A_{m,2}}\right) \quad (4.2)$$

For the ejectors tested here,  $A_{s,1}/A_{m,1} = 3.5$ ,  $A_{s,2}/A_{m,2} = 1$ .

## 4.5 Experimental Results and Discussion

Experiments were carried out using a test rig similar to [31, 48], where nitrogen gas was supplied to the motive nozzle at a fixed pressure, and entrainment ratio was varied using a needle valve to throttle the suction fluid, which was measured using an MKS Alta-180 mass flow meter with a 0-20,000 sccm range. The motive fluid mass flow rate was computed using isentropic flow through the motive nozzle, which previous experiments have shown to be within a few percentage points of measured flow rates [3, 48].

Figure 4.2 (p.99) plots suction draft versus entrainment ratio for the three ejectors. The  $63\mu m$  throat ejector's performance suffers because the nozzle is overexpanded.

As seen from Figure 4.2 (p.99), the suction draft of the  $63\mu m$  throat ejector falls off at lower entrainment ratios than the  $187\mu m$  or  $733\mu m$  ejectors. Prior work on single-stage ejectors predicted the onset of scale effects for throat diameters as small as  $10\mu m$  for throat Reynolds numbers near 1,300 and mixer Reynolds numbers near 400 [6]. Other investigations of two-dimensional micronozzle measurements report weak viscous losses for Reynolds numbers near 2,000 [31]. Using the Reynolds number computed at the motive nozzle throat, we can compute the secondary mixer Reynolds number based on geometry and entrainment ratio. Table 4.4 provides values for the throat and secondary mixer Reynolds numbers from Reference [98].

Table 4.4: Throat and secondary mixer Reynolds numbers

| $D^*_m$    | $Re_{D^*_m}$ | $Re_{D,d,2}$  |
|------------|--------------|---------------|
| $63\mu m$  | 8,300        | 1,500-1,600   |
| $187\mu m$ | 24,200       | 4,900-10,700  |
| $733\mu m$ | 94,800       | 21,000-30,000 |

The behavior seen for the  $63\mu m$  ejector results because the nozzle is over expanded, with an expansion ratio of 4.2 from Table 4.2 (97) which reduces the nozzle

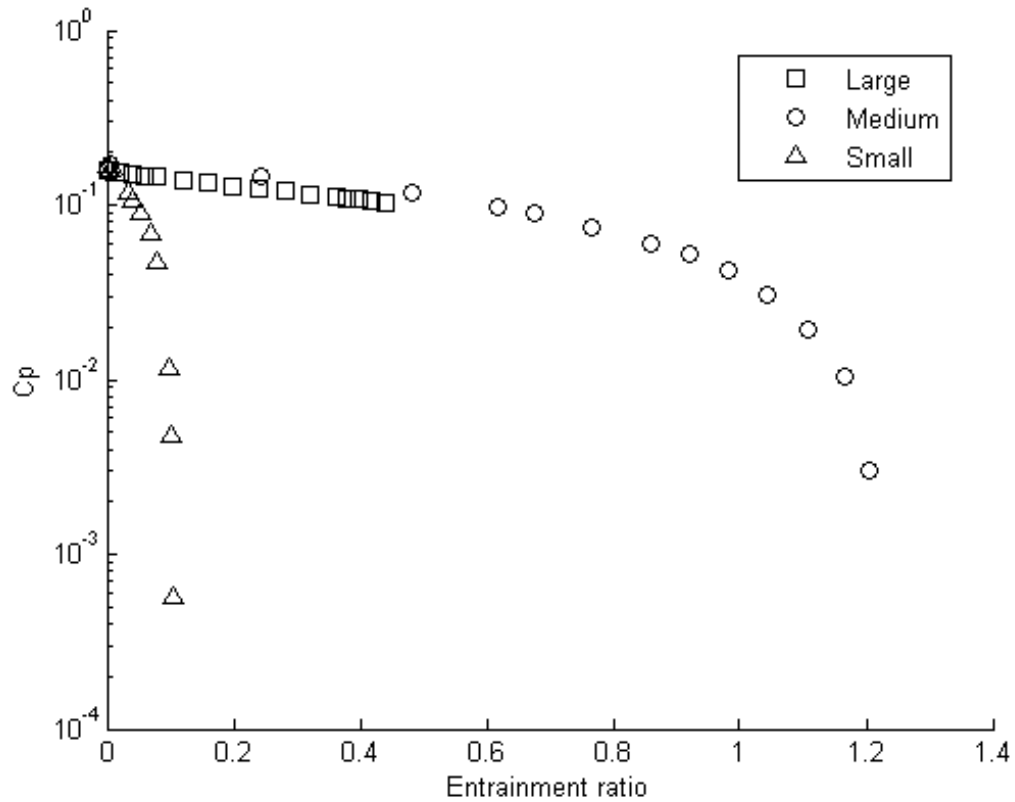


FIGURE 4.2: Schematic and nomenclature for a multi-stage ejector

exit velocity, as seen by invoking the conservation of momentum in the form of the isentropic thrust coefficient. The pressure matching term is computed using the nozzle exit plane static pressure, and the static pressure of the ambient, which for the case of the ejector is taken to be the suction fluid static pressure. When the nozzle exit plane static pressure drops below its surrounding ambient, the exit stream decelerates.

Figure 4.3 (p.100) plots computed thrust coefficients across measured entrainment ratios which correspond to measured suction pressures. We see that the effect of over expansion for the  $63\mu\text{m}$  throat nozzle results in different behavior compared to

the  $187\mu\text{m}$  and  $733\mu\text{m}$  nozzles, both of which have expansion ratios near design in comparison, as shown in Table 4.2 (97).

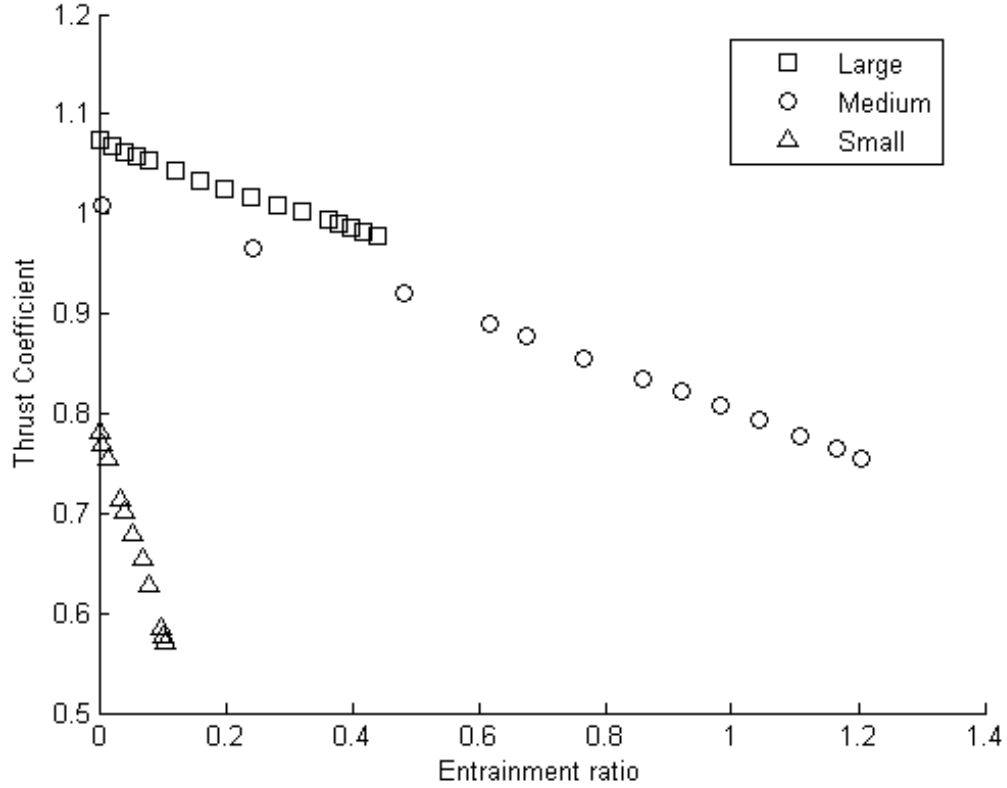


FIGURE 4.3: Computed isentropic thrust coefficients vs. entrainment ratio

Previous work on multi-stage ejectors [76] showed improved efficiency for multi-stage ejectors, which manifests by creating higher suction draft than a single-stage given the same motive total pressure and area ratio. This work employed the same area ratio across both stages for a two-stage ejector also used shorter mixer length-to-diameter ratios,  $L/D \approx 0.5 - 1$ , than conventional ejectors due to the presence of three-dimensional lobes in the mixer. The lobes generate streamwise vorticity, promoting momentum exchange between the higher velocity motive stream and the

lower velocity secondary stream in the shear layers formed when the two streams merge [99, 100].

The current two-stage ejector results presented here do not outperform single-stage ejector results with the same overall area ratio from [31] and similar Reynolds numbers, which is due to the stage-wise area ratios being off-design. The primary and secondary area ratios were different for the test pieces considered here, which may inhibited improvements in performance in comparison to single-stage ejectors.

## 4.6 Conclusions

A multi-stage ejector was tested at three different length scales ( $63\mu m$ ,  $187\mu m$ ,  $733\mu m$ ) using nitrogen gas to motivate and entrain ambient air. The multi-stage ejectors performed similarly to single-stage ejectors of the same overall area ratio. Typically, equal stage-wise area ratios of proper design allow for superior performance compared to single-stage ejectors, but the data presented here for the case of off-design stage-wise area ratios suggests negligible differences in ejector performance. Performance for the  $63\mu m$  ejector suffered due to over expansion of the motive nozzle.

Future work will investigate the lower scale limits of multi-stage ejectors. For applications when volume or weight constrains design, the use of lobed mixers can provide a reduction in ejector volume [76], which can be implemented using standard two-dimensional etching techniques or micro-machining.

## Conclusions

### 5.1 Summary of Results and Conclusions

Experimental results for the single-stage ejector and injector agree well with the theoretical model inclusive of losses.

#### *5.1.1 Single-Stage Ejector*

The experimental results for the single-stage ejector achieve a power density of 308  $kW/L$  show improvement in the state of the art as compared to microscale turbochargers which have demonstrated power densities near 80  $W/L$  [15].

#### *5.1.2 Injector*

The experimental results for the injector achieve a power density of 146  $kW/L$  show improvement in the state of the art as compared to microscale turbopumps which have demonstrated power densities near 370  $W/L$  [12].

## 5.2 Implications

The models in agreement with experimental results predict behavior for microscale jet ejectors and jet injectors. Performance can be predicted to allow for implementation on Power MEMS devices requiring fluid pumping. The model predicts the onset of severe viscous losses and further predicts performance beyond the onset of severe viscous losses. These cases may be of interest to designers working with austere packaging constraints.

### *5.2.1 Single-Stage Ejector*

The single-stage ejector model predicts maximum power densities on the order of 1.1  $MW/L$  for Reynolds numbers, based on the nozzle hydraulic diameter, of roughly 1,300.

### *5.2.2 Injector*

The injector model predicts maximum power densities on the order of 9.3  $MW/L$  for Reynolds numbers, based on the nozzle hydraulic diameter, of roughly 250.

## 5.3 Suggestions for Future Work

### *5.3.1 Applications*

Jet ejectors should be considered for use to supplement gas bearings for microengine applications, especially during the start-up sequence. They are a simple way to pump gases, or liquids, without moving parts and can be easily fabricated using proven MEMS techniques.

Jet injectors show promise in replacing turbopumps for vapor cycles in microengines or for use in microrockets. Although inefficient by comparison, jet injectors do not require high-tolerances for high-speed rotating components as required in turbopumps. When injectors were first developed in the mid-1800's, existing mechanical

pumps suffered from somewhat similar fabrication challenges as the MEMS rotating pumps of today. Jet injectors have great potential to improve, enable and reduce to practice several classes of Power MEMS devices.

### *5.3.2 Modeling*

One of the limitations of the injector model is that it uses boundary layer equations that assume a constant static pressure. In the presence of an adverse pressure gradient, laminar boundary layers tend to separate with ease. This occurrence creates losses, especially at the microscale, where the diffuser geometries are typically short, and flow passages cannot vary three-dimensionally to accommodate pressure gradients, as they do in conventional turbomachines and rocket nozzles. The lower scale limit for proper delivery cone operations will be dependent on approaching the separation limit, which will be a function of the Reynolds number and the pressure gradient. It is recommended for future investigation. The use of features which generate stream-wise vorticity may also enable a reduction in microscale ejector and injector volumes with a commensurate reduction in viscous losses due to less wetted area and the avoidance of developed flow.

### *5.3.3 Other Flow Configurations*

One interesting flow configuration is an axial hole through a plate or surface, much like the nozzles shown here, except that the flow would make a right angle turn and flow out radially, sandwiched between another flat plate. This flow configuration may not be practical for some applications due to the turning losses, and possibly developed flow if the L/D of the lid is adequate, but it may offer an easy way to implement a jet pump using only 2-D planar features. As the jet expands out radially from the center port, the area ratio is constantly changing, and the secondary mass flow rate into the jet can be controlled by the entrance ports through the top lid into

the stream. This changing area may also act as an effective microscale diffuser in some cases.

# Appendix A

## Single-Stage Ejector: Detailed Model

This section outlines the general model used to predict jet ejector performance. It provides a description of the different flow geometries for jet pumps and defines stations and areas. Next, the model develops from first principles by applying the conservation of mass, momentum and energy. The model assumes compressible flow through the motive nozzle [31] and incompressible flow through the secondary inlet and mixing regions for a single stage axial flow configuration [31, 76]. The fluid densities are assumed to be approximately the same in the mixing region by an approximate Munk and Prim principle [37, 76]. The model predicts performance during both on- and off-design operation.

### A.1 Geometry

This section defines the nomenclature and presents example flow paths for jet ejectors and jet pumps. This section proceeds generally but highlights some differences in geometry between jet ejectors and jet injectors.

Figure A.1 (p.107) shows the flows paths for a jet ejector.

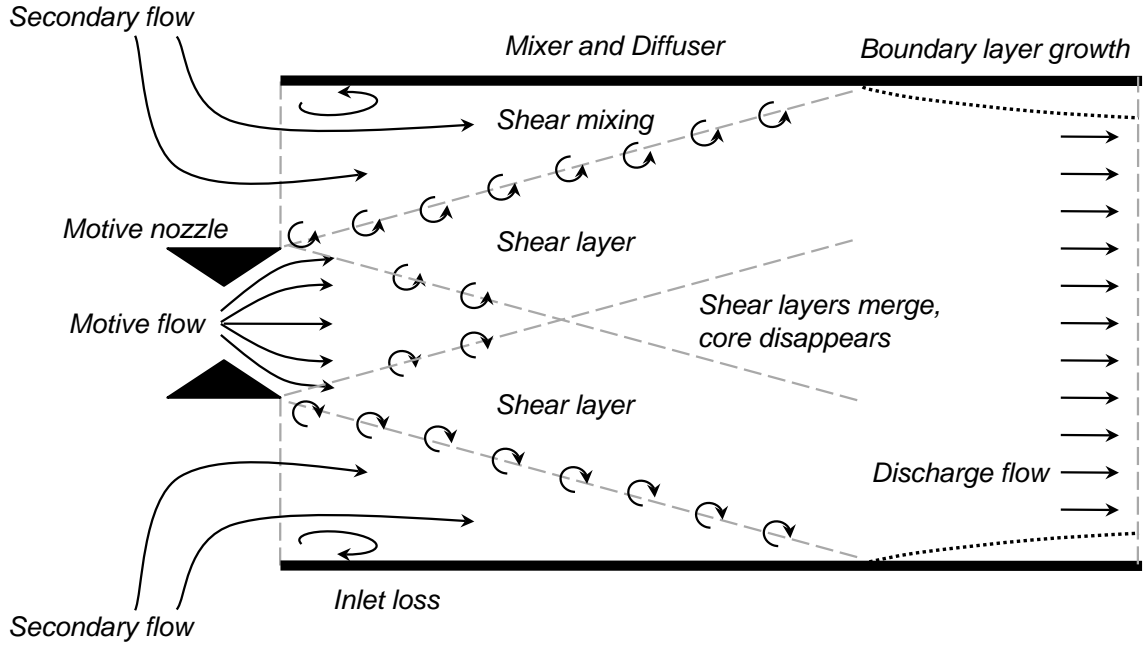


FIGURE A.1: Jet ejector assembly and flow paths

Figure A.2 (p.108) shows the flow paths and nomenclature for a jet pump with a mixing area that is larger than the motive nozzle throat, typically found in jet ejectors, and in this case the mixing region has constant area.

For a constant area duct,

$$A_d = A_{d,i} = A_{d,e} = A_m + A_s \quad (\text{A.1})$$

We can define the ratio of  $A_s/A_m \equiv a$ , such that

$$\frac{A_d}{A_m} = 1 + a \quad (\text{A.2})$$

For the case where the mixer area converges or diverges, it is useful to define an average area ratio for the mixer (or combining cone or delivery cone for the injector case)

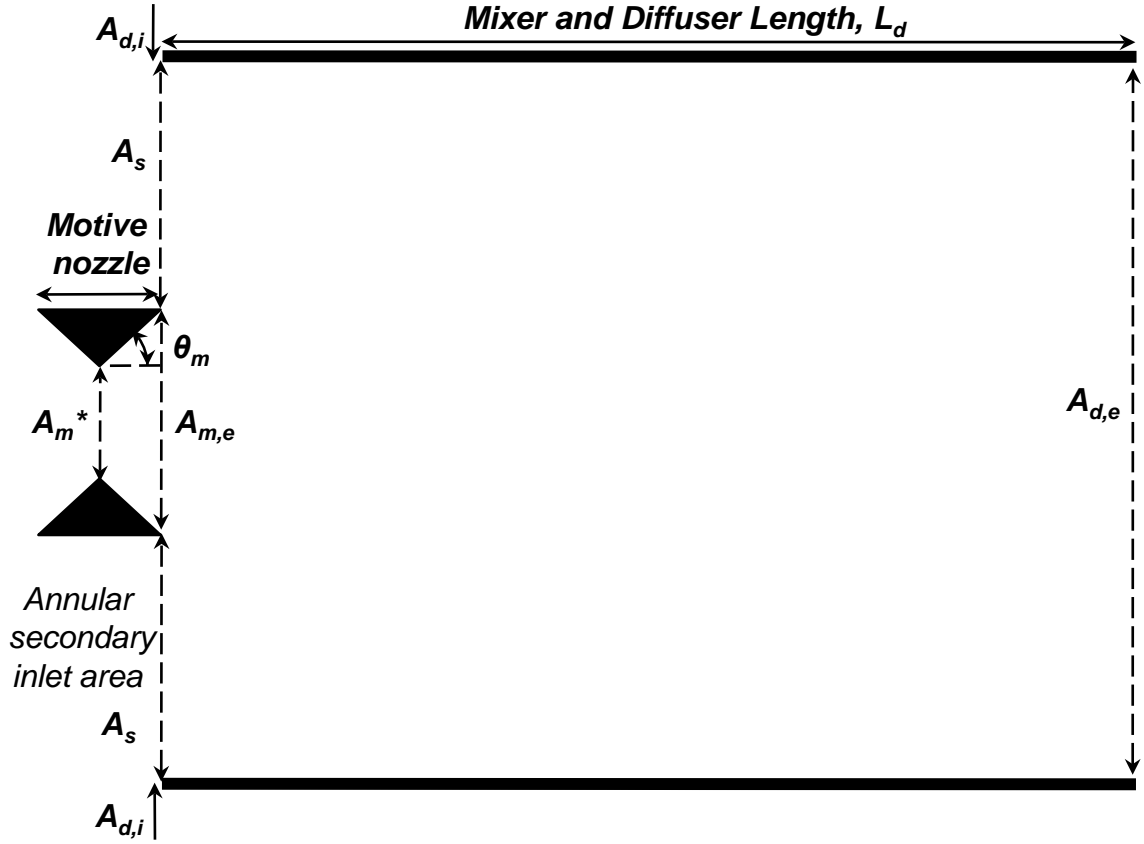


FIGURE A.2: Jet ejector nomenclature

$$\bar{A}_d = 1/2 (A_{d,in} + A_{d,ex}) \quad (\text{A.3})$$

Using equation (A.3), the inlet mixer area  $A_{d,inlet}$  can be expanded and  $\bar{A}_d$  becomes

$$\begin{aligned} \bar{A}_d &= 1/2 (A_m + A_s + A_{d,e}) \\ &= 1/2 (A_m + A_s + A_d) \end{aligned} \quad (\text{A.4})$$

Note that the  $e$  subscript has been dropped,  $A_{d,e} \rightarrow A_d$ .

The contraction ratio of the mixer is expressed as

$$\kappa \equiv \frac{A_{d,i}}{A_{d,e}} = \frac{A_m + A_s}{A_d} \quad (\text{A.5})$$

Again, note that the  $e$  subscript has been dropped,  $A_{d,e} \rightarrow A_d$ .

Equation (B.2) can now be expressed in terms of  $\kappa$

$$\begin{aligned} \bar{A}_d &= 1/2 (A_m + A_s + A_{d,e}) \\ &= \left( \frac{\kappa + 1}{2} \right) A_d \end{aligned} \quad (\text{A.6})$$

## A.2 Conservation of Mass

Consider the case of a single-stage axial flow jet ejector. The control volume is shown below for a constant area mixing region in Figure A.3 (p.110).

The total mass flow rate exiting the mixing region is equal to the sum of the motive and secondary mass flow rates

$$\dot{m}_d = \dot{m}_m + \dot{m}_s \quad (\text{A.7})$$

where

$$\dot{m} = \rho u A \quad (\text{A.8})$$

The mass flux is

$$m'' = \frac{\dot{m}}{A} = \rho u \quad (\text{A.9})$$

The entrainment ratio is defined as the ratio of the secondary mass flow rate to the motive mass flow rate,

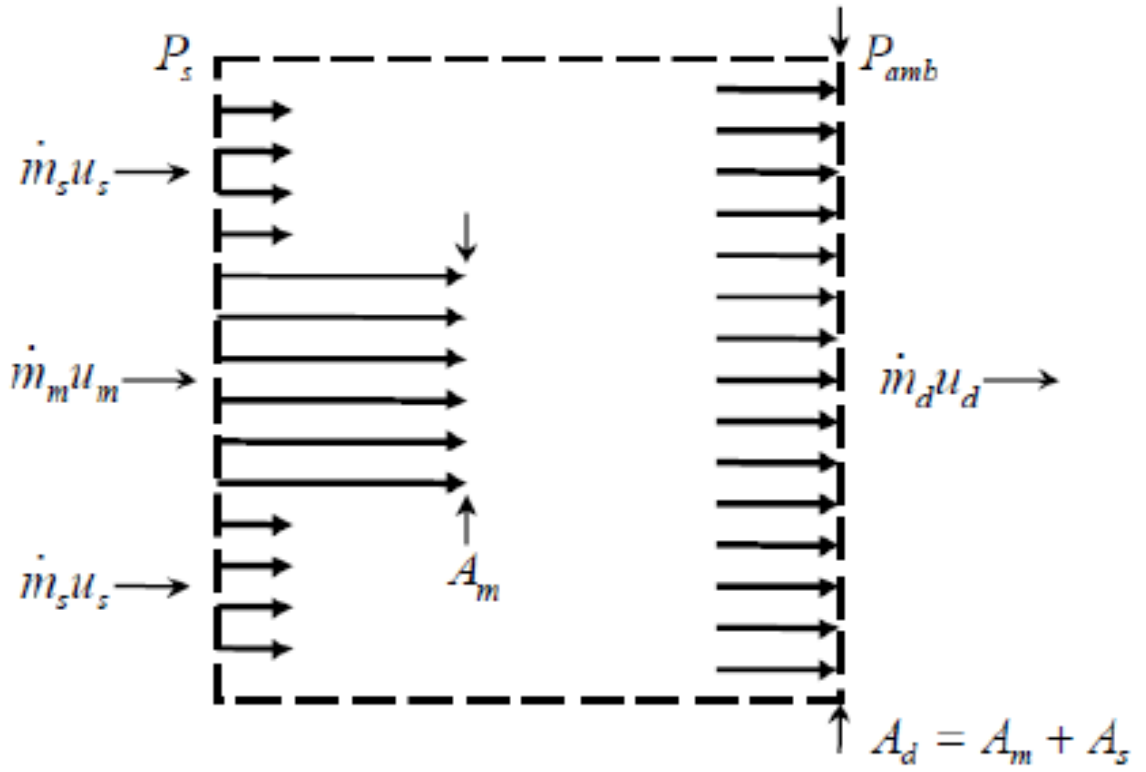


FIGURE A.3: Constant area control volume detailing nomenclature [31]

$$\alpha \equiv \frac{\dot{m}_s}{\dot{m}_m} \quad (\text{A.10})$$

From equation (A.7), the ratio of the discharge mass flow rate to motive mass flow rate is expressed in terms of the entrainment ratio

$$\frac{\dot{m}_d}{\dot{m}_m} = 1 + \alpha \quad (\text{A.11})$$

### A.3 Conservation of Axial Momentum

The conservation of axial momentum in the mixing region captures the inertial contributions from the motive and suction flows inclusive of their respective losses, which will first be represented by place holding terms that are later expanded. A control volume is used with control surfaces on the inlet and exit stations. The model allows for a difference in static pressure between the inlet and exit stations for both the motive nozzle and mixing region.

Apply the conservation of axial momentum across the mixing region to initially produce

$$\dot{m}_d u_d = \dot{m}_m u_m + \dot{m}_s u_s + P_s(A_s + A_m) - P_d(A_d) \quad (\text{A.12})$$

The conservation of axial momentum in the mixing region can be expressed as the sum realized discharge velocity times mass flow summed with loss terms

$$\dot{m}_d u_{d,ideal} = \dot{m}_d u_d + (P_d - P_s)A_d + F_{drag,d} \quad (\text{A.13})$$

Expanding the motive mass flow term,

$$\dot{m}_d u_d = \dot{m}_m u_{m,isen} + (P_m - P_s)A_m - F_{drag,m} + \dot{m}_s u_s + (P_s - P_d)A_d - F_{drag,d} \quad (\text{A.14})$$

where  $F_{drag,d}$  represents drag on the mixing region walls. Next, equation (A.14) is rearranged and expressed in terms of area ratio and entrainment ratio.

$$(P_d - P_s)A_d = \dot{m}_m u_{m,isen} + \dot{m}_s u_s - \dot{m}_d u_d + (P_m - P_s)A_m - F_{drag,m} - F_{drag,d} \quad (\text{A.15})$$

$$(P_d - P_s) \frac{A_d}{A_m} = \frac{\dot{m}_m}{A_m} u_{m,isen} + \frac{\dot{m}_s}{A_m} u_s - \frac{\dot{m}_d}{A_m} u_d + (P_m - P_s) - \frac{F_{drag,m}}{A_m} - \frac{F_{drag,d}}{A_m} \quad (\text{A.16})$$

Recall from the conservation of mass that  $\dot{m} = \rho u A$ ,  $\frac{\dot{m}}{A} = \rho u$ , and  $\frac{\dot{m}}{\rho u} = A$ .

$$(P_d - P_s) \frac{A_d}{A_m} = \rho_m u_{m,e,isen}^2 + \frac{A_s}{A_m} \rho_s u_s^2 - \frac{A_d}{A_m} \rho_d u_d^2 + (P_m - P_s) - \frac{F_{drag,m}}{A_m} - \frac{F_{drag,d}}{A_m} \quad (\text{A.17})$$

Substitute the area ratio terms in terms of the defined area ratio, and multiply (A.17) by  $\frac{1}{2}$  to get

$$(P_d - P_s) \frac{(1+a)}{2} = \frac{1}{2} \rho_m u_{m,e,isen}^2 + \frac{1}{2} a \rho_s u_s^2 - \frac{1}{2} (1+a) \rho_d u_d^2 - \left[ \frac{1}{2} (P_s - P_m) + \frac{\frac{1}{2} F_{drag,m}}{A_m} + \frac{\frac{1}{2} F_{drag,d}}{A_m} \right] \quad (\text{A.18})$$

Divide through by  $\frac{1}{2} \rho_m u_{m,e,isen}^2$ ,

$$\frac{(P_d - P_s)}{\frac{1}{2} \rho_m u_{m,e,isen}^2} \frac{(1+a)}{2} = 1 + a \frac{\rho_s u_s^2}{\rho_m u_{m,e,isen}^2} - (1+a) \frac{\rho_d u_d^2}{\rho_m u_{m,e,isen}^2} - \left[ \frac{\frac{1}{2} (P_s - P_m)}{\frac{1}{2} \rho_m u_{m,e,isen}^2} + \frac{\frac{1}{2} F_{drag,m}/A_m}{\frac{1}{2} \rho_m u_{m,e,isen}^2} + \frac{\frac{1}{2} F_{drag,d}/A_m}{\frac{1}{2} \rho_m u_{m,e,isen}^2} \right] \quad (\text{A.19})$$

Divide through by  $\frac{(1+a)}{2}$

$$\frac{(P_d - P_s)}{\frac{1}{2} \rho_m u_{m,e,isen}^2} = \frac{2}{(1+a)} \left[ 1 + a \frac{\rho_s u_s^2}{\rho_m u_{m,e,isen}^2} - (1+a) \frac{\rho_d u_d^2}{\rho_m u_{m,e,isen}^2} \right] - \frac{1}{(1+a)} \left[ \frac{(P_s - P_m)}{\frac{1}{2} \rho_m u_{m,e,isen}^2} + \frac{F_{drag,m}/A_m}{\frac{1}{2} \rho_m u_{m,e,isen}^2} + \frac{F_{drag,d}/A_m}{\frac{1}{2} \rho_m u_{m,e,isen}^2} \right] \quad (\text{A.20})$$

Using the conservation of mass,

$$\frac{\rho_s}{\rho_m} \frac{u_s^2}{u_{m,e,isen}^2} = \frac{\dot{m}_s^2}{\dot{m}_m^2} \frac{A_m^2}{A_s^2} \frac{\rho_m}{\rho_s} = \frac{\alpha^2}{a^2} \frac{\rho_m}{\rho_s} \quad (\text{A.21})$$

and

$$\frac{\rho_d}{\rho_m} \frac{u_d^2}{u_{m,e,isen}^2} = \frac{\dot{m}_d^2}{\dot{m}_m^2} \frac{A_m^2}{A_d^2} \frac{\rho_m}{\rho_d} = \frac{(1+\alpha)^2}{(1+a)^2} \frac{\rho_m}{\rho_d} \quad (\text{A.22})$$

Substituting these expressions, we get

$$\begin{aligned}
\frac{(P_d - P_s)}{\frac{1}{2}\rho_m u_{m,e,isen}^2} &= \frac{2}{(1+a)} \left[ 1 + a \frac{\alpha^2 \rho_m}{a^2 \rho_s} - (1+a) \frac{(1+\alpha)^2 \rho_m}{(1+a)^2 \rho_d} \right] \\
&\quad - \frac{1}{(1+a)} \left[ \frac{(P_s - P_m)}{\frac{1}{2}\rho_m u_{m,e,isen}^2} + \frac{F_{drag,m}/A_m}{\frac{1}{2}\rho_m u_{m,e,isen}^2} + \frac{F_{drag,d}/A_m}{\frac{1}{2}\rho_m u_{m,e,isen}^2} \right] \\
&= \frac{2a}{(1+a)} \left[ \frac{1}{a} + \frac{\alpha^2 \rho_m}{a^2 \rho_s} - \frac{(1+a)(1+\alpha)^2 \rho_m}{a(1+a)^2 \rho_d} \right] \\
&\quad - \frac{1}{(1+a)} \left[ \frac{(P_s - P_m)}{\frac{1}{2}\rho_m u_{m,e,isen}^2} + \frac{F_{drag,m}/A_m}{\frac{1}{2}\rho_m u_{m,e,isen}^2} + \frac{F_{drag,d}/A_m}{\frac{1}{2}\rho_m u_{m,e,isen}^2} \right] \\
&= \frac{2a}{(1+a)^2} \left[ \frac{(1+a)}{a} + \frac{(1+a)\frac{1}{a}\alpha^2 \frac{\rho_m}{\rho_s}}{a} - \frac{(1+\alpha)^2 \frac{\rho_m}{\rho_d}}{a} \right] \\
&\quad - \frac{1}{(1+a)} \left[ \frac{(P_s - P_m)}{\frac{1}{2}\rho_m u_{m,e,isen}^2} + \frac{F_{drag,m}/A_m}{\frac{1}{2}\rho_m u_{m,e,isen}^2} + \frac{F_{drag,d}/A_m}{\frac{1}{2}\rho_m u_{m,e,isen}^2} \right] \\
&= \frac{2a}{(1+a)^2} \left[ \frac{1+a + \frac{1}{a}\alpha^2 \frac{\rho_m}{\rho_s} + \alpha^2 \frac{\rho_m}{\rho_s} - \frac{\rho_m}{\rho_s} - 2\alpha \frac{\rho_m}{\rho_s} - \alpha^2 \frac{\rho_m}{\rho_s}}{a} \right] \\
&\quad - \frac{1}{(1+a)} \left[ \frac{(P_s - P_m)}{\frac{1}{2}\rho_m u_{m,e,isen}^2} + \frac{F_{drag,m}/A_m}{\frac{1}{2}\rho_m u_{m,e,isen}^2} + \frac{F_{drag,d}/A_m}{\frac{1}{2}\rho_m u_{m,e,isen}^2} \right]
\end{aligned} \tag{A.23}$$

Here we can invoke the similarity principle, allowing the densities to cancel [37, 76].

$$\begin{aligned}
\frac{(P_d - P_s)}{\frac{1}{2}\rho_m u_{m,e,isen}^2} &= \frac{2a}{(1+a)^2} \left[ \frac{1 + a + \frac{1}{a}\alpha^2 + \alpha^2 - 1 - 2\alpha - \alpha^2}{a} \right] \\
&\quad - \frac{1}{(1+a)} \left[ \frac{(P_s - P_m)}{\frac{1}{2}\rho_m u_{m,e,isen}^2} + \frac{F_{drag,m}/A_m}{\frac{1}{2}\rho_m u_{m,e,isen}^2} + \frac{F_{drag,d}/A_m}{\frac{1}{2}\rho_m u_{m,e,isen}^2} \right] \\
&= \frac{2a}{(1+a)^2} \left[ \frac{a - 2\alpha + \frac{1}{a}\alpha^2}{a} \right] \\
&\quad - \frac{1}{(1+a)} \left[ \frac{(P_s - P_m)}{\frac{1}{2}\rho_m u_{m,e,isen}^2} + \frac{F_{drag,m}/A_m}{\frac{1}{2}\rho_m u_{m,e,isen}^2} + \frac{F_{drag,d}/A_m}{\frac{1}{2}\rho_m u_{m,e,isen}^2} \right] \\
\frac{(P_d - P_s)}{\frac{1}{2}\rho_m u_{m,e,isen}^2} &= \frac{2a}{(1+a)^2} \left[ 1 - 2\frac{\alpha}{a} + \frac{\alpha^2}{a^2} \right] \\
&\quad - \frac{1}{(1+a)} \left[ \frac{(P_s - P_m)}{\frac{1}{2}\rho_m u_{m,e,isen}^2} + \frac{F_{drag,m}/A_m}{\frac{1}{2}\rho_m u_{m,e,isen}^2} + \frac{F_{drag,d}/A_m}{\frac{1}{2}\rho_m u_{m,e,isen}^2} \right]
\end{aligned} \tag{A.24}$$

Next, we will expand the inertial terms for the motive and secondary fluids and then return to the discharge fluid.

### A.3.1 Motive Fluid: Compressible Flow with Viscous Losses

The motive flow is treated as compressible, using isentropic flow to compute ideal behavior [85]. Loss terms are then expressed and computed to account for nozzle skin friction due to boundary layers.

#### *Isentropic flow*

For isentropic flow, the ratio of the total pressure,  $P_t$ , to the static pressure  $P$  is given as a function of the Mach number,  $M$  by

$$\frac{P_t}{P} = \left( 1 + \frac{\gamma - 1}{2} M^2 \right)^{\frac{\gamma}{\gamma - 1}} \tag{A.25}$$

Similarly, the ratio of the total temperature,  $T_t$ , to the static temperature  $T$  is given by

$$\frac{T_t}{T} = \left(1 + \frac{\gamma - 1}{2} M^2\right) \quad (\text{A.26})$$

The Mach number is defined as the ratio of the velocity,  $u$  to the speed of sound,  $a_o$

$$M \equiv \frac{u}{a_o} = \frac{u}{\sqrt{\gamma RT}} \quad (\text{A.27})$$

Using these relations, we can expand the motive inertial term, starting with

$$\dot{m}_m u_m = \dot{m}_m u_{m,isen} - (P_s - P_m) A_m - F_{drag,m} \quad (\text{A.28})$$

where the isentropic velocity is computed using isentropic flow relations [85].

### *Thrust coefficient*

Equation (A.28) can also be expressed in terms of the thrust coefficient, which can be used to characterize rocket nozzle performance [36] and is defined as

$$\begin{aligned} C_F &\equiv \frac{F_{thrust}}{F_{thrust,opt}} \\ &= \frac{\dot{m}_m u_{m,e,isen} - (P_s - P_m) A_{m,e} - F_{drag,m}}{\dot{m}_m u_{m,e,isen}} \end{aligned} \quad (\text{A.29})$$

The realized thrust,  $F_{thrust}$  is

$$F_{thrust} = \dot{m}_m u_{m,e,isen} - (P_{amb} - P_{m,e}) A_{m,e} - F_{drag,m} \quad (\text{A.30})$$

The optimal thrust,  $F_{thrust,opt}$  occurs when the nozzle exit static pressure matches the surrounding ambient static pressure, giving

$$F_{thrust,opt} = \dot{m}_m u_{m,e,isen} \quad (\text{A.31})$$

Equation A.29 can be expanded in terms of the nozzle throat diameter and total pressure using the conservation of mass applied at the nozzle throat and isentropic flow equations to give

$$\begin{aligned} C_F &= \frac{F_{thrust}}{P_{t,m} A_m^*} \\ &= \frac{\dot{m}_m u_{m,e,isen} - (P_s - P_m) A_{m,e} - F_{drag,m}}{P_{t,m} A_m^*} \end{aligned} \quad (\text{A.32})$$

The isentropic thrust coefficient,  $C_{F,isen}$  is absent of nozzle wall drag and is

$$C_{F,isen} = \frac{\dot{m}_m u_{m,e,isen} - (P_s - P_m) A_{m,e}}{P_{t,m} A_m^*} \quad (\text{A.33})$$

From equation (A.32), we can express the nozzle wall drag,  $F_{drag,m}$ , in terms of the realized thrust coefficient,  $C_F$ , as

$$F_{drag,m} = C_F P_{t,m} A_m^* - \dot{m}_m u_{m,e,isen} + (P_s - P_m) A_{m,e} \quad (\text{A.34})$$

Next, we express the nozzle wall drag using the skin friction coefficient,  $C_f$ .

### *Nozzle skin friction*

Typical rocket nozzles operate in the turbulent flow regime and experience negligible skin friction coefficient variation along the axial length of the nozzle, and boundary layer effects cause on the order of a 1% decrease in performance [36]. However, as the nozzle length scale decreases, scale effects become significant for low Reynolds numbers, as in the case of micronozzles. For this case, the local skin friction coefficient must be computed as the assumption of constant-valued skin friction may no longer

be valid. This modeling modification enables the prediction of viscous losses or scale effects on performance at small length scales.

The skin friction coefficient is defined as [34, 35]

$$C_f \equiv \frac{\tau_w}{1/2\rho u_{avg}^2} \quad (\text{A.35})$$

where  $\tau_w$  represents the wall shear stress. The skin friction coefficient is related to the Darcy friction factor,  $f$  by

$$C_f = \frac{f}{4} \quad (\text{A.36})$$

Expressions relating  $f$  to Reynolds number based on flow regime (laminar entry, laminar developed, turbulent developed) are provided in [34, 35] and can be generally expressed as a function of the local Reynolds number and local length-to-diameter ratio, and  $C$ ,  $m$ , and  $n$ , which are constants whose values depend on flow regime and appear in Table A.1 [34, 35].

$$C_f = C \text{Re}_{D_h}^{-m} \left( \frac{L}{D_h} \right)^{-n} \quad (\text{A.37})$$

The axial viscous drag force resulting from viscous fluid interaction with the motive nozzle wall may be determined by integrating the local values of the local skin friction coefficient, local dynamic pressure, and local wetted area along the axial length of the nozzle.

$$F_{drag,m} = \int_{x=0}^{x=L} C_f(x) \frac{1}{2} \rho u^2(x) dA_{wet} \quad (\text{A.38})$$

From the definition of the Reynolds number, we can express the local Reynolds number, which varies with axial position, in terms of the nozzle throat Reynolds

number, which is constant for a fixed mass flux evaluated at the nozzle throat.

$$\text{Re}_{D_h} \equiv \frac{\rho u D_h}{\mu} = \frac{m'' D_h}{\mu} = \frac{D_m^*}{D(x)} \frac{4}{\pi} \frac{\dot{m}}{D_m^* \mu} = \left( \frac{A(x)}{A^*} \right)^{-\frac{1}{2}} \frac{4}{\pi} \frac{\dot{m}}{D_m^* \mu} \quad (\text{A.39})$$

The skin friction coefficient is now expressed using (A.39) and gives

$$C_f = C \text{Re}_{D^*}^{-m} \left( \frac{L}{D_m^*} \right)^{-n} \left( \frac{A(x)}{A_m^*} \right)^{-\frac{m}{2}} \quad (\text{A.40})$$

where the local area ratio can be expressed as a function of the local Mach number using isentropic flow relations,

$$\frac{A(x)}{A_m^*} = M^{-1}(x) \left( \frac{2}{\gamma + 1} \right)^{\frac{1}{2} \frac{\gamma + 1}{\gamma - 1}} \left( 1 + \frac{\gamma - 1}{2} M^2(x) \right)^{\frac{1}{2} \frac{\gamma + 1}{\gamma - 1}} \quad (\text{A.41})$$

Next, we expand the local dynamic pressure term using isentropic flow relations and the ideal gas law to find

$$\frac{1}{2} \rho u^2(x) = \frac{1}{2} \frac{\rho u^2(x)}{P} \frac{P}{P_{t,m}} P_{t,m} \quad (\text{A.42})$$

$$\frac{1}{2} \rho u^2(x) = \frac{1}{2} \gamma M^2(x) \left( 1 + \frac{\gamma - 1}{2} M^2(x) \right)^{-\frac{\gamma}{\gamma - 1}} P_{t,m} \quad (\text{A.43})$$

Finally, we must express the local wetted area of the nozzle by using expressions for the wetted perimeter and axial length

$$dA_{\text{wetted}} = \text{perimeter}(x) dx \quad (\text{A.44})$$

where the wetted perimeter can be expressed as

$$\text{perimeter}(x) = \frac{\pi D(x)}{\cos \theta} = \frac{\pi D_m^*}{\cos \theta} \frac{D(x)}{D_m^*} \quad (\text{A.45})$$

The ratio of the local diameter to the throat diameter is expressed in terms of areas, which are related to local Mach number from (A.41), such that

$$\frac{D(x)}{D_m^*} = \left( \frac{A(x)}{A_m^*} \right)^{1/2} \quad (\text{A.46})$$

The axial length can be expressed in terms of the motive nozzle throat diameter and length-to-diameter ratio, which appears in (A.37)

$$dx = D_m^* * \frac{L}{D_m^*} \frac{dx}{L} \quad (\text{A.47})$$

Equation (A.44) becomes

$$dA_{wetted} = \frac{\pi D_m^{*2}}{\cos \theta} \left( \frac{A(x)}{A_m^*} \right)^{1/2} \frac{L}{D_m^*} \frac{dx}{L} \quad (\text{A.48})$$

Using equations (A.40)-(A.43) and (A.48), we expand equation (A.38) to

$$F_{drag,m} = \frac{1}{\cos \theta} P_{t,m} A_m^* C R e_{D_m^*}^{-m} \left( \frac{L}{D_m^*} \right)^{1-n} 2\gamma \left( \frac{\gamma+1}{2} \right)^{-\frac{m+1}{4} \frac{\gamma+1}{\gamma-1}} \int_{x/L=0}^{x/L=1} f(M) \frac{dx}{L} \quad (\text{A.49})$$

where

$$f(M) = \frac{M(x)^{\frac{3-m}{2}}}{\left( 1 + \frac{\gamma-1}{2} M(x)^2 \right)^{\frac{(3-m)\gamma-(m+1)}{4(\gamma-1)}}} \quad (\text{A.50})$$

The constants  $C$ ,  $m$  and  $n$  depend on flow regime. Table (A.1) summarizes values for these constants [34, 35] and provides typical values for the terms they influence in equation (A.49).

Table A.1: Typical values for computation of motive nozzle hydrodynamic loss

| Flow regime       | $C$   | $m$  | $n$  | $2\gamma \left(\frac{\gamma+1}{2}\right)^{-\frac{m+1}{4} \frac{\gamma+1}{\gamma-1}}$ |                | $\int_{x/L=0}^{x/L=1} f(M) \frac{dx}{L}$ |                |
|-------------------|-------|------|------|--|----------------|--|----------------|
|                   |       |      |      | $\gamma = 1.1$   | $\gamma = 1.4$ | $\gamma = 1.1$                           | $\gamma = 1.4$ |
| Turbulent         | 0.046 | 0.2  | 0    | 1.57   | 2.02           | 0.5                                      | 0.9            |
| Laminar entry     | 3.72  | 0.67 | 0.33 | 1.4  | 1.77           | 1.3                                      | 1.3            |
| Laminar developed | 16    | 1    | 0    | 1.32   | 2.04           | 2.1                                      | 1.7            |

Finally, the drag force on the motive nozzle walls can be nondimensionalized by dividing through by the dynamic pressure at the motive nozzle exit. To be conservative, the laminar developed flow regime constant values are used to evaluate the integrals in Table A.1, giving values of 2.04 and 1.7, which are later approximated to be 4 in equation ([? ]). The remaining constants  $C$ ,  $m$  and  $n$  affecting the skin friction coefficient terms are determined based on flow regime using Table A.1

$$\begin{aligned}
 C_{f,m} &= \frac{F_{drag,m}}{1/2\rho u_{m,e,isen}^2} \\
 &\approx \frac{1/\epsilon_m \left(1 + \frac{\gamma-1}{2} M_{e,m}^2\right)^{\frac{\gamma}{\gamma-1}}}{\cos \theta \frac{\gamma}{2} M_{e,m}^2} CRe_{D_m^*}^{-m} \left(\frac{L}{D_m^*}\right)^{1-n} \quad (2.04)(1.7) \quad (A.51) \\
 &\approx \frac{4/\epsilon_m \left(1 + \frac{\gamma-1}{2} M_{e,m}^2\right)^{\frac{\gamma}{\gamma-1}}}{\cos \theta \frac{\gamma}{2} M_{e,m}^2} CRe_{D_m^*}^{-m} \left(\frac{L}{D_m^*}\right)^{1-n}
 \end{aligned}$$

The drag force may also be non-dimensionalized into a form similar to the thrust coefficient,  $C_F$ , by instead dividing through by the motive total pressure,  $P_{t,m}$  and nozzle throat area,  $A_m^*$ , giving

$$\begin{aligned}
 C_{F,lost} &= \frac{F_{drag,m}}{P_{t,m} A_m^*} \\
 &\approx \frac{1}{\cos \theta_m} CRe_{D_m^*}^{-m} \left(\frac{L}{D_m^*}\right)^{1-n} \quad (2.04)(1.7) \quad (A.52) \\
 &\approx \frac{4}{\cos \theta_m} CRe_{D_m^*}^{-m} \left(\frac{L}{D_m^*}\right)^{1-n}
 \end{aligned}$$

### A.3.2 Secondary Fluid: Inlet Losses

If losses occur across the suction inlet, then the downstream total pressure will not equal the upstream total pressure. Since the upstream total pressure can be conveniently measured, it's more convenient to express ejector performance using the upstream pressure. However, we must use the downstream velocity due to the control volume analysis selected, drawn in Figure A.3 (p.110), so we need to express the downstream velocity in terms of upstream values. Using Bernoulli and the conservation of mass,

$$P_{ts,ds} = P_s + \frac{1}{2}\rho u_{s,ds}^2 \quad \text{and} \quad \dot{m}_{s,ds} = \rho u_{s,ds} A_{s,ds}$$

$$P_{ts,us} = P_s + \frac{1}{2}\rho u_{s,us}^2 \quad \text{and} \quad \dot{m}_{s,us} = \rho u_{s,us} A_{s,us}$$

Since mass is conserved across the inlet,

$$\dot{m}_{s,us} = \dot{m}_{s,ds}$$

$$\rho u_{s,us} A_{s,us} = \rho u_{s,ds} A_{s,ds}$$

$$u_{s,ds} = u_{s,us} \left( \frac{A_{s,us}}{A_{s,ds}} \right) \tag{A.53}$$

From Bernoulli on the upstream flow,

$$u_{s,us} = \sqrt{\frac{2}{\rho} (P_{ts,us} - P_s)} \tag{A.54}$$

Substituting (A.54) into (A.53) gives

$$u_{s,ds} = \left( \frac{A_{s,us}}{A_{s,ds}} \right) \sqrt{\frac{2}{\rho} (P_{ts,us} - P_s)} \tag{A.55}$$

Using the conservation of mass,

$$\frac{\dot{m}_{s,ds}}{\rho A_{s,ds}} = \left( \frac{A_{s,us}}{A_{s,ds}} \right) \sqrt{\frac{2}{\rho} (P_{ts,us} - P_s)}$$

$$\dot{m}_{s,ds} = A_{s,ds} \left( \frac{A_{s,us}}{A_{s,ds}} \right) \sqrt{2\rho (P_{ts,us} - P_s)} \quad (\text{A.56})$$

Define the ratio of the upstream to downstream areas as

$$C_d \equiv \left( \frac{A_{s,us}}{A_{s,ds}} \right) \quad (\text{A.57})$$

and

$$\dot{m}_{s,ds} = C_d A_{s,ds} \sqrt{2\rho (P_{ts,us} - P_s)} \quad (\text{A.58})$$

This discharge coefficient captures losses associated with flow restriction across the secondary inlet. Typical values based on geometry are provided in Reference [83, 90]. For a sharp-edged inlet a value of  $C_d = 0.5$  is recommended. For re-entrant flow, when the sharp-edged inlet protrudes into the flow, a value of  $C_d = 0.8$  is recommended.

Equation (A.58) is commonly presented as

$$\dot{m}_s = C_d A_s \sqrt{2\Delta P \rho} \quad (\text{A.59})$$

The difference in upstream and downstream total pressures can be found by using the Bernoulli equation to express static pressure in terms of downstream total pressure and dynamic pressure and substituting into equation (A.58)

$$P_s = P_{ts,ds} - \frac{1}{2} \rho u_{s,ds}^2$$

$$\dot{m}_s^2 = C_d^2 A_{s,ds}^2 2\rho \left( P_{ts,us} - P_{ts,ds} - \frac{1}{2} \rho u_{s,ds}^2 \right) \quad (\text{A.60})$$

$$P_{ts,us} - P_{ts,ds} = \frac{1}{C_d^2} \frac{1}{2\rho} \rho u_{s,ds}^2 - \frac{1}{2} \rho u_{s,ds}^2 \quad (\text{A.61})$$

$$P_{ts,us} - P_{ts,ds} = \frac{1}{2} \rho u_{s,ds}^2 \left( \frac{1}{C_d^2} - 1 \right) \quad (\text{A.62})$$

From equation (A.61), we see that in the absence of losses, the upstream and downstream total pressures are equal when  $C_d^2 = 1$ . Normalizing equation (A.62) by the motive dynamic pressure,

$$\frac{P_{ts,us} - P_{ts,ds}}{\frac{1}{2}\rho u_{m,e,isen}^2} = \left( \frac{1}{C_d^2} - 1 \right) \frac{\alpha^2}{a^2} \quad (\text{A.63})$$

Substitute equation (A.63) into equation (A.24) to give

$$\begin{aligned} \frac{P_d - P_{ts,us}}{\frac{1}{2}\rho u_{m,e,isen}^2} &= \frac{2a}{(1+a)^2} \left[ 1 - 2\frac{\alpha}{a} - \left( \frac{1}{C_d^2} \frac{(1+a)^2}{2a} - 1 \right) \frac{\alpha^2}{a^2} \right] \\ &- \frac{1}{(1+a)} \left[ \frac{(P_s - P_m)}{\frac{1}{2}\rho_m u_{m,e,isen}^2} + \frac{F_{drag,m}/A_m}{\frac{1}{2}\rho_m u_{m,e,isen}^2} + \frac{F_{drag,d}/A_m}{\frac{1}{2}\rho_m u_{m,e,isen}^2} \right] \end{aligned} \quad (\text{A.64})$$

### A.3.3 Discharge Fluid: Mixer Skin Friction

The loss modeling concludes by accounting for the wall drag in the mixing region. The drag on the mixing region wall is computed using an approach similar to the motive nozzle drag computation. However, the subsonic core velocity in the mixer is assumed to vary with downstream length to a lesser extent than the core flow in the motive nozzle. This assumption allows for the use of an average velocity and eliminates the need to compute local values for velocity within the mixer. The computation proceeds as follows.

The viscous drag force due to the presence of walls in the mixer is expressed as

$$F_{drag,d} = \int_{x=0}^{x=L} C_f \frac{1}{2} \rho u_d^2(x) dA_{wet} \quad (\text{A.65})$$

The wetted area for an arbitrary mixer is

$$\begin{aligned}
dA_{wetted} &= \text{perimeter}(x)dx \\
&= \frac{\pi D(x)}{\cos \theta} dx \\
&= \frac{\pi D_d}{\cos \theta} \frac{D(x)}{D_d} dx \\
&= \frac{\pi D_d}{\cos \theta} \left( \frac{D(x)}{D_d} \right) \left( D_d \frac{L}{D_d} \frac{dx}{L} \right) \\
&= \frac{\pi D_d^2}{\cos \theta} \left( \frac{D(x)}{D_d} \right) \left( \frac{L}{D_d} \right) \frac{dx}{L} \\
&= \frac{\pi D_d^2}{\cos \theta} \left( \frac{A(x)}{A_d} \right)^{1/2} \left( \frac{L}{D_d} \right) \frac{dx}{L}
\end{aligned} \tag{A.66}$$

For a constant area mixer,

$$dA_{wetted} = \pi D_d^2 \left( \frac{L}{D_d} \right) \frac{dx}{L} \tag{A.67}$$

Similar to equation (A.37), the local skin friction coefficient,  $C_f$ , can be expressed as a function of the local Reynolds number and local length-to-diameter ratio, and  $C$ ,  $m$ , and  $n$  are constants whose values depend on flow regime and appear in Table A.1.

$$C_f = C \text{Re}_{D_h}^{-m} \left( \frac{L}{D_h} \right)^{-n} \tag{A.68}$$

Using the Reynolds number definition, the ejector area ratio,  $a$ , the entrainment ratio,  $\alpha$  and the motive nozzle expansion ratio,  $\epsilon_m$ , the discharge flow Reynolds number in the mixer can be expressed as

$$\begin{aligned}
Re_{D_d} &\equiv \frac{\rho u_d D_d}{\mu} \\
&= \frac{m_d'' D_d}{\mu} \frac{m_m^{*''}}{m_m^{*''}} \frac{D_m^*}{D_m} \frac{D_m}{D_m^*} \\
&= \frac{m_m^{*''} D_m^*}{\mu} \frac{m_d''}{m_m^{*''}} \frac{D_d}{D_m} \frac{D_m}{D_m^*} \\
&= Re_{D_m^*} \frac{m_d''}{m_m^{*''}} \left( \frac{A_d}{A_m} \right)^{1/3} \left( \frac{A_m}{A_m^*} \right)^{1/2} \\
&= Re_{D_m^*} \frac{1 + \alpha}{1 + a} (1 + a)^{1/2} (\epsilon_m)^{-1/2} \\
&= Re_{D_m^*} (1 + \alpha) \left( \frac{1/\epsilon_m}{1 + a} \right)^{1/2}
\end{aligned} \tag{A.69}$$

Assuming that changes in the core flow velocity along the mixer length are negligible, equation (A.65) is expressed in terms of the average skin friction coefficient and average discharge flow velocity

$$F_{drag,d} \approx \int_{x=0}^{x=L} \bar{C}_{f,d} \frac{1}{2} \rho \bar{u}_d^2 dA_{wet} \tag{A.70}$$

Equation A.70 is integrated across the axial length of the mixer using average flow values and the results from (A.67),(A.68) and (A.69) and non-dimensionalized by  $1/2\rho u_{m,e,isen}^2$

$$\frac{F_{drag,d}}{1/2\rho u_{m,e,isen}^2} \approx 4C Re_{D_d}^{-m} \left( \frac{L_d}{D_d} \right)^{1-n} \frac{(1 + \alpha)^2}{1 + a} \tag{A.71}$$

The constants  $C$ ,  $m$  and  $n$  are determined based on flow regime using Table A.1.

Using the definition of the skin friction coefficient, equation (A.71) can also be expressed as

$$C_{f,d} \approx 4C \left( \frac{L_d}{D_d} \right) \frac{(1 + \alpha)^2}{1 + a} \quad (\text{A.72})$$

#### A.4 General Model with Losses

The general loss model that computes the performance as a function of entrainment ratio and area ratio is

$$\begin{aligned} \frac{P_d - P_{t,us}}{1/2\rho u_{m,e,isen}^2} &\approx \frac{2a}{(1+a)^2} \left[ 1 - 2\frac{\alpha}{a} - \frac{1}{2} \left( a + 1/a \right) \frac{\alpha^2}{a^2} \right] - \left( \frac{1}{C_d^2} - 1 \right) \frac{\alpha^2}{a^2} \dots \\ &- \frac{4/\epsilon_m}{\cos \theta} \frac{\left( 1 + \frac{\gamma-1}{2} M_{e,m}^2 \right)^{\frac{\gamma}{\gamma-1}}}{\frac{\gamma}{2} M_{e,m}^2} CRe_{D_m^*}^{-m} \left( \frac{L}{D_m^*} \right)^{1-n} \dots \\ &- 4 \frac{(1+\alpha)^2}{(1+a)^2} CRe_{D_d}^{-m} \left( \frac{L_d}{D_d} \right)^{1-n} \dots \\ &- \frac{1}{1+a} \frac{P_s - P_m}{1/2\rho u_{m,e,isen}^2} \end{aligned} \quad (\text{A.73})$$

The constants  $C$ ,  $m$  and  $n$  are determined based on flow regime using Table A.1.

# Appendix B

## Injector: Detailed Model

This section outlines the general model used to predict jet injector performance. It provides a recap of the different flow geometries for jet pumps presented in Appendix A and defines stations and areas. Next, the model develops from first principles by applying the conservation of mass and momentum. The model assumes compressible flow through the motive nozzle [31] and incompressible flow through the secondary inlet and mixing regions for a single stage axial flow configuration [31, 76]. The fluid densities are assumed to be approximately the same in the mixing region by an approximate Munk and Prim principle [37, 76]. The model predicts performance during both on- and off-design operation. For the injector, boundary layer growth is modeled in the combining cone. Since the fluid density for a liquid is of order  $10^3$  compared to 1 for a gas, by the conservation of mass, blockages in flow area will be more pronounced for liquids. The model approximates displacement thickness in the combining cone using boundary layer equations for a flat plate with no pressure gradient.

## B.1 Geometry

This section defines the nomenclature and presents example flow paths for jet ejectors and jet pumps. This section proceeds generally but highlights some differences in geometry between jet ejectors and jet injectors.

Figure B.1 (p.128) shows the flows paths for a jet ejector.

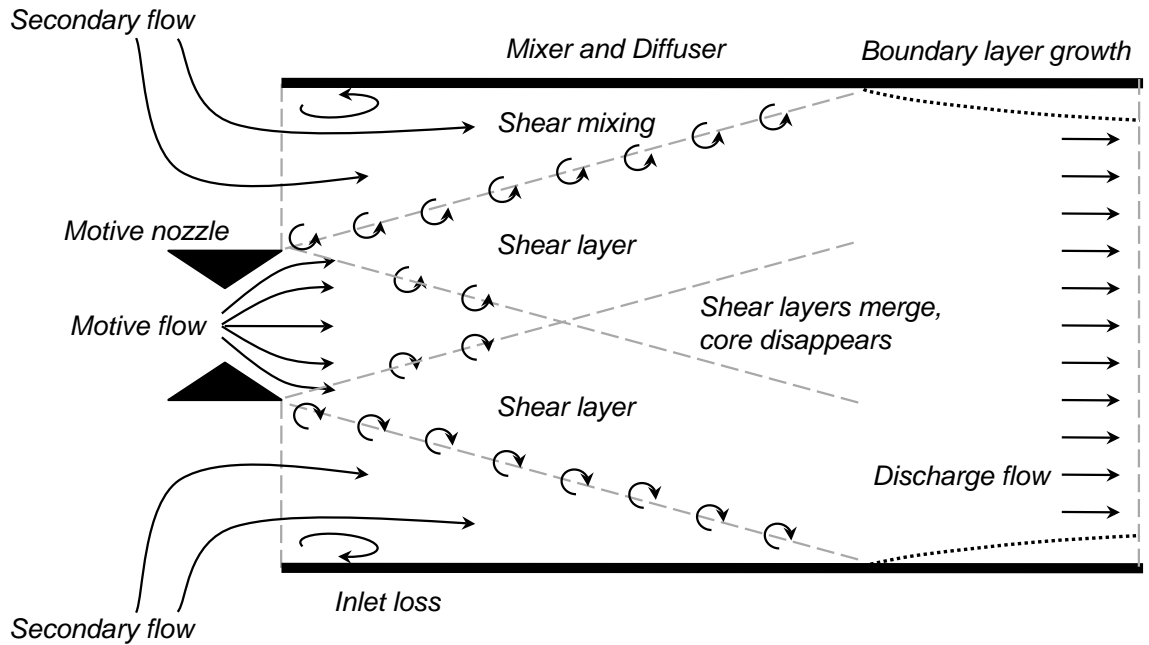


FIGURE B.1: Jet ejector assembly and flow paths

Figure A.3 (p.110) shows the control volume and nomenclature for a jet ejector. The jet ejector typically features a mixing area that is larger than the motive nozzle throat, as opposed to the jet injector, which has a mixing region throat that is approximately equal to or smaller than the motive nozzle throat. Figure B.2 (p.129) shows the flow paths and nomenclature for a jet pump with a mixing area that is approximately equal or smaller in area compared to the motive nozzle throat.

The converging portion, referred to here as the combining cone, is followed by

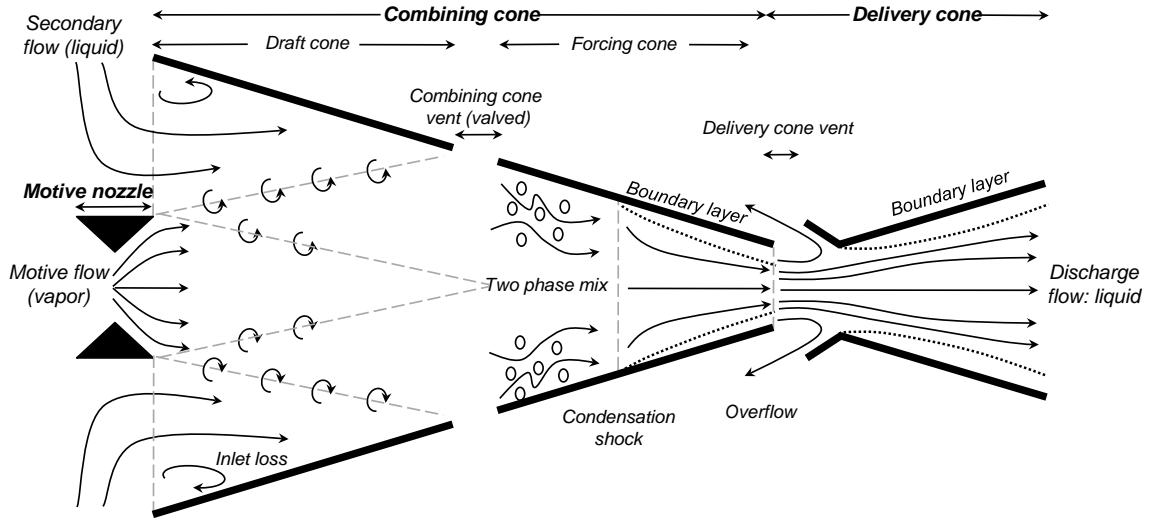


FIGURE B.2: Jet injector assembly and flow paths

a diffuser, which is commonly called a delivery cone. Figure B.3 (p.130) provides the nomenclature for a jet injector. Figure B.4 (p.131),  $A_m$  represents the motive nozzle exit area. It should be noted that in the model the  $e$  subscript has been dropped,  $A_{m,e} \Rightarrow A_m$ . The secondary flow area,  $A_s$ , is computed by taking the difference between the combining cone inlet area,  $A_{d,i}$ , and motive nozzle exit area,  $A_s = A_{d,i} - A_m$ . Note that in the model this  $e$  subscript has also been dropped for the combining cone exit area,  $A_{d,e} \Rightarrow A_d$ .

For the case of the jet injector where the mixer area converges or diverges, it is useful to define an average area ratio for combining cone or delivery cone as

$$\bar{A}_d = 1/2 (A_{d,in} + A_{d,ex}) \quad (\text{B.1})$$

Using equation (B.1), the inlet mixer area  $A_{d,inlet}$  can be expanded and  $\bar{A}_d$  becomes

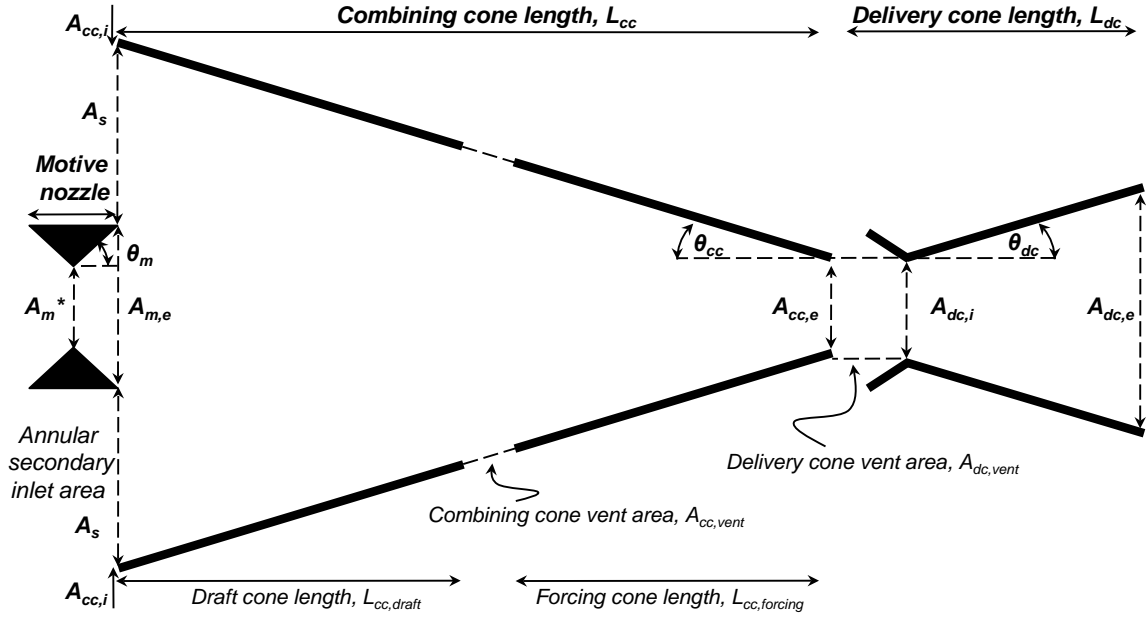


FIGURE B.3: Injector nomenclature

$$\begin{aligned}\bar{A}_d &= 1/2 (A_m + A_s + A_{d,e}) \\ &= 1/2 (A_m + A_s + A_d)\end{aligned}\tag{B.2}$$

Note that the  $e$  subscript has been dropped,  $A_{d,e} \rightarrow A_d$ .

The contraction ratio of the mixer is expressed as

$$\kappa \equiv \frac{A_{d,i}}{A_{d,e}} = \frac{A_m + A_s}{A_d}\tag{B.3}$$

Again, note that the  $e$  subscript has been dropped,  $A_{d,e} \rightarrow A_d$ .

Equation (B.2) can now be expressed in terms of  $\kappa$

$$\begin{aligned}\bar{A}_d &= 1/2 (A_m + A_s + A_{d,e}) \\ &= \left(\frac{\kappa + 1}{2}\right) A_d\end{aligned}\tag{B.4}$$

## B.2 Conservation of Mass

Consider the case of a single-stage axial flow jet pump. The control volume is shown below for a typical injector geometry in Figure B.4 (p.131).

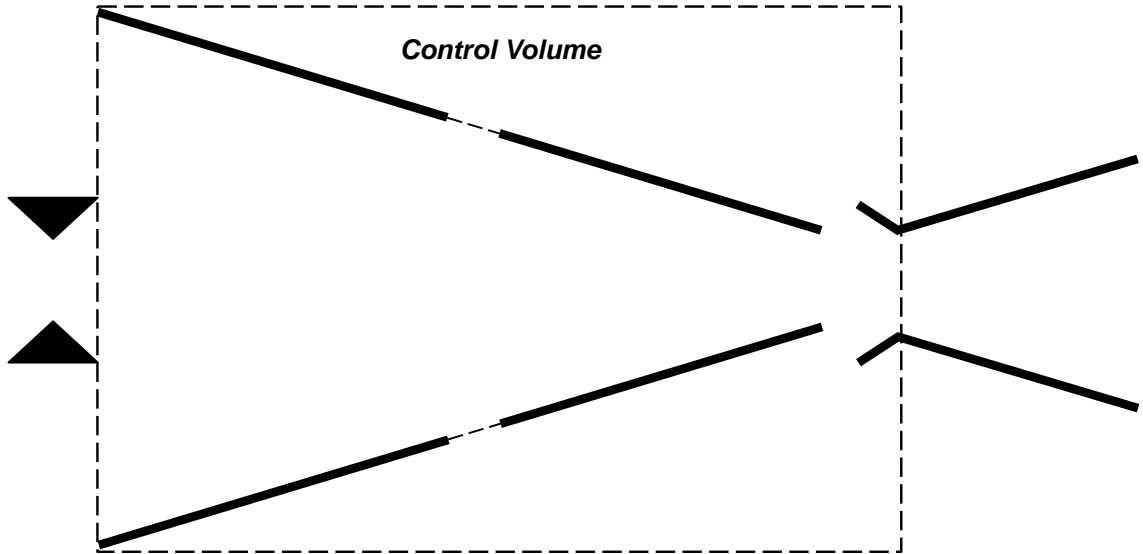


FIGURE B.4: Schematic detailing the control volume used to develop the injector model

The total mass flow rate exiting the mixing region is equal to the sum of the motive and secondary mass flow rates

$$\dot{m}_d = \dot{m}_m + \dot{m}_s \quad (\text{B.5})$$

where

$$\dot{m} = \rho u A \quad (\text{B.6})$$

The mass flux is

$$m'' = \frac{\dot{m}}{A} = \rho u \quad (\text{B.7})$$

The entrainment ratio is defined as the ratio of the secondary mass flow rate to the motive mass flow rate,

$$\alpha \equiv \frac{\dot{m}_s}{\dot{m}_m} \quad (\text{B.8})$$

From equation (B.5) , the ratio of the discharge mass flow rate to motive mass flow rate is expressed in terms of the entrainment ratio

$$\frac{\dot{m}_d}{\dot{m}_m} = 1 + \alpha \quad (\text{B.9})$$

### *B.2.1 Conservation of Mass and Energy: Minimum Entrainment Ratio*

We can estimate the minimum entrainment ratio required to achieve condensation of the motive vapor by using the conservation of mass and conservation of energy. Assuming negligible heat transfer to the walls of the combining cone, the conservation of energy across the combining cone gives

$$\dot{Q}_{in} = \dot{Q}_{out} \quad (\text{B.10})$$

where

$$\dot{Q}_{in} = \dot{m}_m h_{vap} + \dot{m}_m c_{p,s} T_{sat} + \dot{m}_m c_{p,m} T_m + \dot{m}_s c_p T_s \quad (\text{B.11})$$

Since most of the motive vapor will be fully condensed, the discharge fluid specific heat will approximately equal to that of the secondary fluid,  $c_{p,d} \approx c_{p,s} = c_{p,liquid}$ . The heat transfer rate leaving the control volume will be, in the absence of heat transfer to the walls,

$$\dot{Q}_{out} = \dot{m}_d c_{p,d} T_d = \dot{m}_m c_{p,s} T_d + \dot{m}_m c_{p,m} T_d + \dot{m}_s c_{p,s} T_d \quad (\text{B.12})$$

Combining equations (B.11) and (B.12) gives

$$\dot{m}_m [h_{vap} + c_{p,m} (T_d - T_{sat}) + c_{p,s} (T_{sat} - T_d)] = \dot{m}_s c_{p,s} (T_d - T_{sat}) \quad (\text{B.13})$$

Since the enthalpy of vaporization,  $h_{vap}$ , is large compared to  $c_{p,m}$  and  $c_{p,s}$ ,

$$h_{vap} \left[ 1 + \frac{c_{p,m} (T_d - T_{sat})}{h_{vap}} + \frac{c_{p,s} (T_{sat} - T_d)}{h_{vap}} \right] \approx h_{vap} \quad (\text{B.14})$$

Thus, equation (B.13) can be approximated as

$$\alpha = \frac{\dot{m}_s}{\dot{m}_m} \approx \frac{h_{vap}}{c_{p,s} (T_d - T_s)} \quad (\text{B.15})$$

Equation (B.16) represents the minimum entrainment ratio required for operation when the discharge pressure equals the saturation temperature at a given boiler pressure,  $T_d = T_{sat}$ . This entrainment ratio implies that no secondary cooling capacity remains and also corresponds to the maximum achievable injector discharge pressure.

$$\alpha_{min} = \frac{\dot{m}_s}{\dot{m}_m} \approx \frac{h_{vap}}{c_{p,s} (T_{sat} - T_s)} \quad (\text{B.16})$$

### B.3 Conservation of Axial Momentum

The conservation of axial momentum in the mixing region captures the inertial contributions from the motive and suction flows inclusive of their respective losses, which will first be represented by place holding terms that are later expanded. A control volume is used with control surfaces on the inlet and exit stations. The model allows

for a difference in static pressure between the inlet and exit stations for both the motive nozzle and mixing region.

Apply the conservation of axial momentum across the mixing region to initially produce

$$\dot{m}_d u_d = \dot{m}_m u_{m,e} + \dot{m}_s u_s + P_s(A_s + A_m) - P_d(A_d) - \beta(A_s + A_m - A_d) + (P_{m,e} - P_s)A_{m,e} \quad (\text{B.17})$$

where  $\beta$  represents the average static pressure in the combining cone

$$\beta = \frac{1}{2}(P_d + P_s) \quad (\text{B.18})$$

Using the geometric definitions from equation (B.4), where the average combining cone area,  $\bar{A}_d$ , is expressed in terms of the contraction ratio,  $\kappa$ , equation (B.17) is rearranged to give

$$\begin{aligned} \dot{m}_d u_d &= \dot{m}_m u_{m,e} + \dot{m}_s u_s + (P_s - P_d)\bar{A}_d + (P_{m,e} - P_s)A_{m,e} \\ &= \dot{m}_m u_{m,e} + \dot{m}_s u_s + (P_s - P_d) \left( \frac{\kappa + 1}{2} \right) A_d + (P_{m,e} - P_s)A_{m,e} \end{aligned} \quad (\text{B.19})$$

The left-hand side of equation (B.19) can be rearranged using the conservation of mass as

$$\dot{m}_d u_d = 2 \left( \frac{1}{2} \rho u_d^2 \right) A_d \quad (\text{B.20})$$

Using the conservation of energy in the form of the Bernoulli equation, equation (B.20) becomes

$$\dot{m}_d u_d = 2(P_{t,d} - P_d) A_d \quad (\text{B.21})$$

Using this result, equation (B.19) can be expressed as

$$\begin{aligned}
2(P_{t,d} - P_d) A_d &= \dot{m}_m u_{m,e} + \dot{m}_s u_s + (P_s - P_d) \bar{A}_d + (P_{m,e} - P_s) A_{m,e} \\
&= \dot{m}_m u_{m,e} + \dot{m}_s u_s + (P_s - P_d) \left( \frac{\kappa + 1}{2} \right) A_d + (P_{m,e} - P_s) A_{m,e}
\end{aligned} \tag{B.22}$$

Next, we will expand the secondary fluid term,  $\dot{m}_s u_s$ , and its associated inlet losses.

### B.3.1 Secondary Fluid: Inlet Losses

If losses occur across the suction inlet, then the downstream total pressure will not equal the upstream total pressure. Since the upstream total pressure can be conveniently measured, it's more convenient to use the upstream pressure. However, we must use the downstream velocity due to the control volume analysis selected, so we need to express the downstream velocity in terms of upstream values. Starting with the conservation of mass,

$$\dot{m}_s u_s = 2 \left( \frac{1}{2} \rho_s u_{s,ds}^2 \right) A_s \tag{B.23}$$

We can express the secondary flow inlet area,  $A_s$ , in terms of the mixing region minimum area,  $A_d$ , and the motive nozzle exit area,  $A_{m,e}$

$$\begin{aligned}
A_s &= A_s + A_{m,e} - A_{m,e} \\
&= \kappa A_d - \epsilon \frac{A_m^*}{A_d} A_d \\
&= \left( \kappa - \epsilon \frac{A_m^*}{A_d} \right) A_d
\end{aligned} \tag{B.24}$$

Using the Bernoulli equation and the conservation of mass,

$$P_{ts,ds} = P_s + \frac{1}{2}\rho u_{s,ds}^2 \quad \text{and} \quad \dot{m}_{s,ds} = \rho u_{s,ds} A_{s,ds}$$

$$P_{ts,us} = P_s + \frac{1}{2}\rho u_{s,us}^2 \quad \text{and} \quad \dot{m}_{s,us} = \rho u_{s,us} A_{s,us}$$

We can express downstream total pressure,  $P_{t,s,ds}$ , in terms of the upstream total pressure,  $P_{t,s,us}$ , and the inlet total pressure loss,  $\Delta P_t$ , as

$$P_{t,s,ds} = P_{t,s,us} - \Delta P_t \quad (\text{B.25})$$

From the derivation presented in Appendix A, we have equation (A.58) as it is commonly presented

$$\begin{aligned} \dot{m}_s &= C_d A_s \sqrt{2\Delta P_t \rho} \\ &= C_d A_s \sqrt{2(P_{t,s,us} - P_s)\rho} \end{aligned} \quad (\text{B.26})$$

The conservation of mass is used to rearrange equation (B.26) as

$$\begin{aligned} \dot{m}_s &= C_d A_s \sqrt{2\Delta P_t \rho} \\ (\rho u_{s,ds} A_s)^2 &= C_d^2 A_s^2 2(P_{t,s,us} - P_s)\rho \\ \dot{m}_s u_s &= C_d^2 (P_{t,s,us} - P_s) \end{aligned} \quad (\text{B.27})$$

This discharge coefficient,  $C_d$  captures losses associated with flow restriction across the secondary inlet. Typical values based on geometry are provided in Reference [83, 90]. For a sharp-edged inlet a value of  $C_d = 0.5$  is recommended. For re-entrant flow, when the sharp-edged inlet protrudes into the flow, a value of  $C_d = 0.8$  is recommended.

Equation (B.27) can be substituted into equation (B.19) to give

$$\begin{aligned}
2(P_{t,d} - P_d)A_d = & \dot{m}_m u_{m,e} + C_d^2(P_{t,s,us} - P_s) \left( \kappa - \epsilon \frac{A_m^*}{A_d} \right) A_d + \dots \\
& + (P_s - P_d) \left( \frac{\kappa + 1}{2} \right) A_d + (P_{m,e} - P_s) A_{m,e}
\end{aligned} \tag{B.28}$$

Dividing through by  $2A_d$  gives

$$\begin{aligned}
(P_{t,d} - P_d) = & \dot{m}_m u_{m,e} \frac{1}{2A_d} + \frac{1}{2} C_d^2 (P_{t,s,us} - P_s) \left( \kappa - \epsilon \frac{A_m^*}{A_d} \right) + \dots \\
& + (P_s - P_d) \left( \frac{\kappa + 1}{4} \right) + \frac{1}{2} (P_{m,e} - P_s) \frac{A_{m,e}}{A_d}
\end{aligned} \tag{B.29}$$

Using the expansion ratio,  $\epsilon$ , equation (B.29) becomes

$$\begin{aligned}
(P_{t,d} - P_d) = & \dot{m}_m u_{m,e} \frac{1}{2A_d} + \frac{1}{2} C_d^2 (P_{t,s,us} - P_s) \left( \kappa - \epsilon \frac{A_m^*}{A_d} \right) + \dots \\
& + (P_s - P_d) \left( \frac{\kappa + 1}{4} \right) + \frac{1}{2} (P_{m,e} - P_s) \epsilon \frac{A_m^*}{A_d}
\end{aligned} \tag{B.30}$$

Next, we can subtract  $P_{t,s,us}$  and add  $P_d$  to both sides to give

$$\begin{aligned}
(P_{t,d} - P_{t,s,us}) = & \dot{m}_m u_{m,e} \frac{1}{2A_d} + \frac{1}{2} C_d^2 (P_{t,s,us} - P_s) \left( \kappa - \epsilon \frac{A_m^*}{A_d} \right) + \dots \\
& + (P_s - P_d) \left( \frac{\kappa + 1}{4} \right) + \frac{1}{2} (P_{m,e} - P_s) \epsilon \frac{A_m^*}{A_d} - P_{t,s,us} + P_d
\end{aligned} \tag{B.31}$$

From the Bernoulli equation, we know that

$$(P_s - P_d) \left( \frac{\kappa + 1}{4} \right) = (P_{t,s,us} - P_d - \frac{1}{2} \rho u_s^2) \left( \frac{\kappa + 1}{4} \right) \tag{B.32}$$

From equation (B.27)

$$\dot{m}_s u_s = \frac{1}{2} \rho u_s^2 = C_d^2 (P_{t,s,us} - P_s) \quad (\text{B.33})$$

Substituting equation (B.33) into equation (B.31) gives

$$\begin{aligned} P_{t,d} - P_{t,s,us} &= \dot{m}_m u_{m,e} \frac{1}{2A_d} + \frac{1}{2} C_d^2 (P_{t,s,us} - P_s) \left( \kappa - \epsilon \frac{A_m^*}{A_d} \right) + \dots \\ &+ \left[ P_{t,s,us} - P_d - \frac{1}{2} C_d^2 (P_{t,s,us} - P_s) \right] \left( \frac{\kappa + 1}{4} \right) + \dots \\ &+ \frac{1}{2} (P_{m,e} - P_s) \epsilon \frac{A_m^*}{A_d} - P_{t,s,us} + P_d \end{aligned} \quad (\text{B.34})$$

Collecting terms and rearranging,

$$\begin{aligned} P_{t,d} - P_{t,s,us} &= \dot{m}_m u_{m,e} \frac{1}{2A_d} + \frac{1}{2} C_d^2 (P_{t,s,us} - P_s) \left( \frac{3}{4} \kappa - \frac{1}{4} - \epsilon \frac{A_m^*}{A_d} \right) + \dots \\ &+ (P_{t,s,us} - P_d) \left( \frac{\kappa + 1}{4} \right) - P_{t,s,us} + P_d + \dots \\ &+ \frac{1}{2} (P_{m,e} - P_s) \epsilon \frac{A_m^*}{A_d} \end{aligned} \quad (\text{B.35})$$

$$\begin{aligned} P_{t,d} - P_{t,s,us} &= \dot{m}_m u_{m,e} \frac{1}{2A_d} + \frac{1}{2} C_d^2 \left[ \frac{3\kappa - 1}{4} - \epsilon \frac{A_m^*}{A_d} \right] (P_{t,s,us} - P_s) + \dots \\ &+ \left[ \frac{\kappa + 1}{4} - 1 \right] (P_{t,s,us} - P_d) + \dots \\ &+ \frac{1}{2} (P_{m,e} - P_s) \epsilon \frac{A_m^*}{A_d} \end{aligned} \quad (\text{B.36})$$

$$\begin{aligned}
P_{t,d} - P_{t,s,us} &= \dot{m}_m u_{m,\epsilon} \frac{1}{2A_d} + \frac{1}{2} C_d^2 \left[ \frac{3\kappa - 1}{4} - \epsilon \frac{A_m^*}{A_d} \right] (P_{t,s,us} - P_s) + \dots \\
&+ \left[ \frac{\kappa - 3}{4} \right] (P_{t,s,us} - P_d) + \dots \\
&+ \frac{1}{2} (P_{m,e} - P_s) \epsilon \frac{A_m^*}{A_d}
\end{aligned} \tag{B.37}$$

Next, we will express the motive mass flow rate and velocity assuming compressible flow with losses and conclude with expressing injector performance in terms of the motive nozzle thrust coefficient,  $C_F$ .

### B.3.2 Motive Fluid: Compressible Flow with Viscous Losses

The motive flow is treated as compressible, using isentropic flow to compute ideal behavior [85]. Loss terms are then expressed and computed to account for nozzle skin friction due to boundary layers.

#### *Thrust coefficient*

We can express equation (B.37) in terms of the motive nozzle thrust coefficient,  $C_F$ , which is defined as

$$\begin{aligned}
C_F &= \frac{F_{thrust}}{P_{t,m} A_m^*} \\
&= \frac{\dot{m}_m u_{m,e,isen} - (P_s - P_{m,e}) A_{m,e} - F_{drag,m}}{P_{t,m} A_m^*}
\end{aligned} \tag{B.38}$$

The optimal thrust,  $F_{thrust,opt}$  occurs when the nozzle exit static pressure matches the surrounding ambient static pressure, giving

$$F_{thrust,opt} = \dot{m}_m u_{m,e,isen} \tag{B.39}$$

The optimal thrust coefficient,  $C_{F,opt}$ , can be defined as

$$C_{F,opt} = \frac{\dot{m}_m u_{m,e,isen} - F_{drag,m}}{P_{t,m} A_m^*} \quad (\text{B.40})$$

The isentropic thrust coefficient,  $C_{F,isen}$  is absent of nozzle wall drag and is

$$C_{F,isen} = \frac{\dot{m}_m u_{m,e,isen} - (P_s - P_m) A_{m,e}}{P_{t,m} A_m^*} \quad (\text{B.41})$$

We begin by dividing equation (B.37) by the motive total pressure,  $P_{t,m}$ ,

$$\begin{aligned} \frac{P_{t,d} - P_{t,s,us}}{P_{t,m}} &= \dot{m}_m u_{m,e} \frac{1}{2A_d} + \frac{1}{2} C_d^2 \left[ \frac{3\kappa - 1}{4} - \epsilon \frac{A_m^*}{A_d} \right] \frac{P_{t,s,us} - P_s}{P_{t,m}} + \dots \\ &+ \left[ \frac{\kappa - 3}{4} \right] \frac{P_{t,s,us} - P_d}{P_{t,m}} + \dots \\ &+ \frac{1}{2} \frac{P_{m,e} - P_s}{P_{t,m}} \epsilon \frac{A_m^*}{A_d} \end{aligned} \quad (\text{B.42})$$

Equation (B.42) is then expressed in terms of the thrust coefficient as

$$\begin{aligned} \frac{P_{t,d} - P_{t,s,us}}{P_{t,m}} &= \frac{C_F A_m^*}{2 A_d} + \frac{1}{2} C_d^2 \left[ \frac{3\kappa - 1}{4} - \epsilon \frac{A_m^*}{A_d} \right] \frac{P_{t,s,us} - P_s}{P_{t,m}} + \dots \\ &+ \left[ \frac{\kappa - 3}{4} \right] \frac{P_{t,s,us} - P_d}{P_{t,m}} \end{aligned} \quad (\text{B.43})$$

If we assume that  $P_s \approx P_d$ , then equation (B.43) becomes

$$\frac{P_{t,d} - P_{t,s,us}}{P_{t,m}} = \frac{C_F A_m^*}{2 A_d} + \frac{1}{2} C_d^2 \left[ (\kappa - 1) - \epsilon \frac{A_m^*}{A_d} \right] \frac{P_{t,s,us} - P_s}{P_{t,m}} \quad (\text{B.44})$$

If we assume that the nozzle exit pressure is matched to the surrounding ambient pressure, or  $P_s \approx P_{m,e}$ , then equation (B.43) becomes

$$\begin{aligned} \frac{P_{t,d} - P_{t,s,us}}{P_{t,m}} &= \frac{C_{F,opt}}{2} \frac{A_m^*}{A_d} + \frac{1}{2} C_d^2 \left[ \frac{3\kappa - 1}{4} - \epsilon \frac{A_m^*}{A_d} \right] \left[ \frac{P_{t,s,us}}{P_{t,m}} - \frac{P_{m,e}}{P_{t,m}} \right] + \dots \\ &+ \left[ \frac{\kappa - 3}{4} \right] \frac{P_{t,s,us} - P_d}{P_{t,m}} \end{aligned} \quad (\text{B.45})$$

Equation (B.45) can be solved to find  $A_m^*/A_d$

$$\frac{A_m^*}{A_d} = \frac{\frac{P_{t,d} - P_{t,s,us}}{P_{t,m}} - \frac{1}{2} C_d^2 \frac{3\kappa - 1}{4} - \left[ \frac{P_{t,s,us}}{P_{t,m}} - \frac{P_{m,e}}{P_{t,m}} \right] - \left[ \frac{\kappa - 3}{4} \right] \frac{P_{t,s,us} - P_d}{P_{t,m}}}{\frac{C_{F,opt}}{2} - \frac{1}{2} C_d^2 \epsilon \left[ \frac{P_{t,s,us}}{P_{t,m}} - \frac{P_{m,e}}{P_{t,m}} \right]} \quad (\text{B.46})$$

From equation (A.32), we can express the nozzle wall drag,  $F_{drag,m}$ , in terms of the realized thrust coefficient,  $C_F$ , as

$$F_{drag,m} = C_F P_{t,m} A_m^* - \dot{m}_m u_{m,e,isen} + (P_s - P_m) A_{m,e} \quad (\text{B.47})$$

Next, we express the nozzle wall drag using the skin friction coefficient,  $C_f$ .

#### *Nozzle skin friction*

Typical rocket nozzles operate in the turbulent flow regime and experience negligible skin friction coefficient variation along the axial length of the nozzle, and boundary layer effects cause on the order of a 1% decrease in performance [36]. However, as the nozzle length scale decreases, scale effects become significant for low Reynolds numbers, as in the case of micronozzles. For this case, the local skin friction coefficient must be computed as the assumption of constant-valued skin friction may no longer be valid. This modeling modification enables the prediction of viscous losses or scale effects on performance at small length scales.

The skin friction coefficient is defined as [34, 35]

$$C_f \equiv \frac{\tau_w}{1/2\rho u_{avg}^2} \quad (\text{B.48})$$

where  $\tau_w$  represents the wall shear stress. The skin friction coefficient is related to the Darcy friction factor,  $f$  by

$$C_f = \frac{f}{4} \quad (\text{B.49})$$

Expressions relating  $f$  to Reynolds number based on flow regime (laminar entry, laminar developed, turbulent developed) are provided in [34, 35] and can be generally expressed as a function of the local Reynolds number and local length-to-diameter ratio, and  $C$ ,  $m$ , and  $n$ , which are constants whose values depend on flow regime and appear in Table A.1 [34, 35].

$$C_f = C \text{Re}_{D_h}^{-m} \left( \frac{L}{D_h} \right)^{-n} \quad (\text{B.50})$$

The axial viscous drag force resulting from viscous fluid interaction with the motive nozzle wall may be determined by integrating the local values of the local skin friction coefficient, local dynamic pressure, and local wetted area along the axial length of the nozzle.

$$F_{drag,m} = \int_{x=0}^{x=L} C_f(x) \frac{1}{2} \rho u^2(x) dA_{wet} \quad (\text{B.51})$$

From the definition of the Reynolds number, we can express the local Reynolds number, which varies with axial position, in terms of the nozzle throat Reynolds number, which is constant for a fixed mass flux evaluated at the nozzle throat.

$$\text{Re}_{D_h} \equiv \frac{\rho u D_h}{\mu} = \frac{m'' D_h}{\mu} = \frac{D_m^*}{D(x)} \frac{4}{\pi} \frac{\dot{m}}{D_m^* \mu} = \left( \frac{A(x)}{A^*} \right)^{-\frac{1}{2}} \frac{4}{\pi} \frac{\dot{m}}{D_m^* \mu} \quad (\text{B.52})$$

The skin friction coefficient is now expressed using (B.52) and gives

$$C_f = C \text{Re}_{D^*}^{-m} \left( \frac{L}{D_m^*} \right)^{-n} \left( \frac{A(x)}{A_m^*} \right)^{-\frac{m}{2}} \quad (\text{B.53})$$

where the local area ratio can be expressed as a function of the local Mach number using isentropic flow relations,

$$\frac{A(x)}{A_m^*} = M^{-1}(x) \left( \frac{2}{\gamma + 1} \right)^{\frac{1}{2} \frac{\gamma+1}{\gamma-1}} \left( 1 + \frac{\gamma-1}{2} M^2(x) \right)^{\frac{1}{2} \frac{\gamma+1}{\gamma-1}} \quad (\text{B.54})$$

Next, we expand the local dynamic pressure term using isentropic flow relations and the ideal gas law to find

$$\frac{1}{2} \rho u^2(x) = \frac{1}{2} \frac{\rho u^2(x)}{P} \frac{P}{P_{t,m}} P_{t,m} \quad (\text{B.55})$$

$$\frac{1}{2} \rho u^2(x) = \frac{1}{2} \gamma M^2(x) \left( 1 + \frac{\gamma-1}{2} M^2(x) \right)^{-\frac{\gamma}{\gamma-1}} P_{t,m} \quad (\text{B.56})$$

Finally, we must express the local wetted area of the nozzle by using expressions for the wetted perimeter and axial length

$$dA_{\text{wetted}} = \text{perimeter}(x) dx \quad (\text{B.57})$$

where the wetted perimeter can be expressed as

$$\text{perimeter}(x) = \frac{\pi D(x)}{\cos \theta} = \frac{\pi D_m^* D(x)}{\cos \theta D_m^*} \quad (\text{B.58})$$

The ratio of the local diameter to the throat diameter is expressed in terms of areas, which are related to local Mach number from (B.54), such that

$$\frac{D(x)}{D_m^*} = \left( \frac{A(x)}{A_m^*} \right)^{1/2} \quad (\text{B.59})$$

The axial length can be expressed in terms of the motive nozzle throat diameter and length-to-diameter ratio, which appears in (B.50)

$$dx = D_m^* * \frac{L}{D_m^*} \frac{dx}{L} \quad (\text{B.60})$$

Equation (B.57) becomes

$$dA_{wetted} = \frac{\pi D_m^{*2}}{\cos \theta} \left( \frac{A(x)}{A_m^*} \right)^{1/2} \frac{L}{D_m^*} \frac{dx}{L} \quad (\text{B.61})$$

Using equations (B.53)-(B.56) and (B.61), we expand equation (B.51) to

$$F_{drag,m} = \frac{1}{\cos \theta} P_{t,m} A_m^* C R e_{D_m^*}^{-m} \left( \frac{L}{D_m^*} \right)^{1-n} 2\gamma \left( \frac{\gamma+1}{2} \right)^{-\frac{m+1}{4} \frac{\gamma+1}{\gamma-1}} \int_{x/L=0}^{x/L=1} f(M) \frac{dx}{L} \quad (\text{B.62})$$

where

$$f(M) = \frac{M(x)^{\frac{3-m}{2}}}{\left( 1 + \frac{\gamma-1}{2} M(x)^2 \right)^{\frac{(3-m)\gamma-(m+1)}{4(\gamma-1)}}} \quad (\text{B.63})$$

The constants  $C$ ,  $m$  and  $n$  depend on flow regime. Table (B.1) summarizes values for these constants [34, 35] and provides typical values for the terms they influence in equation (B.62).

Finally, the drag force on the motive nozzle walls can be nondimensionalized by dividing through by the motive total pressure,  $P_{t,m}$  and nozzle throat area,  $A_m^*$ . To be conservative, the laminar developed flow regime constant values are used to evaluate

Table B.1: Typical values for computation of motive nozzle hydrodynamic loss

| Flow regime       | $C$   | $m$  | $n$  | $2\gamma \left(\frac{\gamma+1}{2}\right)^{-\frac{m+1}{4} \frac{\gamma+1}{\gamma-1}}$ |                | $\int_{x/L=0}^{x/L=1} f(M) \frac{dx}{L}$ |                |
|-------------------|-------|------|------|--|----------------|--|----------------|
|                   |       |      |      | $\gamma = 1.1$   | $\gamma = 1.4$ | $\gamma = 1.1$                           | $\gamma = 1.4$ |
| Turbulent         | 0.046 | 0.2  | 0    | 1.57   | 2.02           | 0.5                                      | 0.9            |
| Laminar entry     | 3.72  | 0.67 | 0.33 | 1.4  | 1.77           | 1.3                                      | 1.3            |
| Laminar developed | 16    | 1    | 0    | 1.32   | 2.04           | 2.1                                      | 1.7            |

the integrals in Table B.1, giving values of 1.32 and 2.1, which are approximated to be 3. The remaining constants  $C$ ,  $m$  and  $n$  affecting the skin friction coefficient terms are determined based on flow regime using Table B.1

$$\begin{aligned}
 C_{f,m} &= \frac{F_{drag,m}}{P_{t,m} A_m^*} \\
 &\approx \frac{1}{\cos \theta_m} C Re_{D_m^*}^{-m} \left(\frac{L}{D_m^*}\right)^{1-n} \quad (1.32)(2.1) \quad (B.64) \\
 &\approx \frac{3}{\cos \theta_m} C Re_{D_m^*}^{-m} \left(\frac{L}{D_m^*}\right)^{1-n}
 \end{aligned}$$

### B.3.3 Discharge Fluid: Mixer Skin Friction and Blockage

#### Combining cone skin friction

For this portion, losses from skin friction in the combining cone are considered, and skin friction in the delivery cone is neglected. Reference [73] provides that delivery cone losses typically account for around 10% of the total losses in miniature steam injectors. Since the secondary fluid receives approximately all of its momentum from the motive fluid, we can model the drag force between the motive fluid and secondary fluid within the combining cone and assume it to be equal to the drag from the combining cone wall on the secondary fluid because momentum is conserved. Thus, the combining cone skin friction coefficient,  $C_{f,cc}$ , is computed based on the motive nozzle exit conditions and geometry. At the entrance to the combining cone, we assume that the motive vapor flow area is approximately equal to the nozzle exit

area, or  $A_{m,e} \approx A_{cc,i}$ , and we also assume that the the combining cone exit area is small compared to the combining cone inlet area, or  $A_{cc,e} \ll A_{cc,i}$ . The motive fluid dynamic pressure is as constant, and the Reynolds number based on the motive nozzle exit is used. The drag force is integrated across the length of the combining cone. The computation proceeds as follows.

The viscous drag force due to the presence of walls in the mixer is expressed as

$$F_{drag,d} = \int_{x=0}^{x=L} C_f \frac{1}{2} \rho u_d^2(x) dA_{wet} \quad (\text{B.65})$$

The wetted area for an arbitrary mixer is

$$\begin{aligned} dA_{wetted} &= \textit{perimeter}(x) dx \\ &= \frac{\pi D(x)}{\cos \theta} dx \\ &= \frac{\pi D_d}{\cos \theta} \frac{D(x)}{D_d} dx \\ &= \frac{\pi D_d}{\cos \theta} \left( \frac{D(x)}{D_d} \right) \left( D_d \frac{L}{D_d} \frac{dx}{L} \right) \\ &= \frac{\pi D_d^2}{\cos \theta} \left( \frac{D(x)}{D_d} \right) \left( \frac{L}{D_d} \right) \frac{dx}{L} \\ &= \frac{\pi D_d^2}{\cos \theta} \left( \frac{A(x)}{A_d} \right)^{1/2} \left( \frac{L}{D_d} \right) \frac{dx}{L} \end{aligned} \quad (\text{B.66})$$

Similar to equation (B.50), the local skin friction coefficient,  $C_f$ , can be expressed as a function of the local Reynolds number and local length-to-diameter ratio, and  $C$ ,  $m$ , and  $n$  are constants whose values depend on flow regime and appear in Table B.1.

$$C_f = C \text{Re}_{D_h}^{-m} \left( \frac{L}{D_h} \right)^{-n} \quad (\text{B.67})$$

The Reynolds number is taken at the motive nozzle exit and is

$$\text{Re}_{D_{m,e}} \equiv \frac{m''_{m,e} D_{m,e}}{\mu} \quad (\text{B.68})$$

Assuming that changes in the average core flow velocity along the mixer length are negligible, equation (B.65) is expressed in terms of the average skin friction coefficient and average discharge flow velocity

$$F_{drag,d} \approx \int_{x=0}^{x=L} \bar{C}_{f,d} \frac{1}{2} \rho \bar{u}_{m,e}^2 dA_{wet} \quad (\text{B.69})$$

Equation B.69 is integrated across the axial length of the combining cone using average flow values and becomes

$$F_{drag,cc} \approx \frac{1}{2} \rho_m u_{m,e}^2 \frac{A_{m,e}}{\cos \theta_{cc}} 4C \text{Re}_{D_{m,e}}^{-m} \left( \frac{L_{cc}}{D_{m,e}} \right)^{1-n} \int_{x/L=0}^{x/L=1} \left( 1 - \frac{x}{L} \right)^{m+1} \frac{dx}{L} \quad (\text{B.70})$$

The constants  $C$ ,  $m$  and  $n$  are determined based on flow regime using Table B.1.

Equation B.69 can be non-dimensionalized by the motive total pressure,  $P_{t,m}$ , and motive nozzle throat area,  $A_m^*$ , to give the combining cone skin friction coefficient

$$C_{f,cc} \approx \frac{1/2 \rho_m u_{m,e}^2}{P_{t,m}} \epsilon \frac{4C \text{Re}_{D_{m,e}}^{-m}}{\cos \theta_{cc}} \left( \frac{L_{cc}}{D_{m,e}} \right)^{1-n} \frac{1}{m+2} \quad (\text{B.71})$$

### *Combining cone blockage*

Blockage due to boundary layers can alter device performance by changing the area ratios of flow passages, especially near the exit regions of flow passages where the boundary layers become thickest in comparison to the entry regions or nozzle throats. Boundary layer thickness,  $\delta$ , is a function of Reynolds number, as seen in Figure 1.5

(p.9). Boundary layer thickness can be generally expressed in terms of Reynolds number as

$$\left(\frac{\delta}{L}\right) = CRe_{D_h}^{-m} \left(\frac{L}{D_h}\right)^{-n} \quad (\text{B.72})$$

Table B.2: Boundary layer flow regime constants

| <i>Boundary Layer</i> | <i>C</i> | <i>m</i> | <i>n</i> |
|-----------------------|----------|----------|----------|
| Turbulent             | 0.037    | 1/5      | 1/5      |
| Laminar               | 5        | 1/2      | 1/2      |

Boundary layer displacement thickness,  $\delta^*$ , quantifies the flow area blockage from boundary layer growth. Displacement thickness is approximately equal to a certain fraction of the general boundary layer thickness,  $\delta$ , based on flow regime. Greitzer recommends use of the following values [37]

$$\begin{aligned} \delta_{turbulent}^* &= \delta/8 \\ \delta_{laminar}^* &= \delta/3 \end{aligned} \quad (\text{B.73})$$

For flow geometries with circular cross-sectional areas, the effective flow area,  $A_{eff}$ , can be expressed in terms of the displacement thickness,  $\delta^*$ , and the diameter,  $D$ , as

$$A_{eff} = \frac{\pi}{4} D^2 \left[ 1 - \left( 1 - 2\frac{\delta^*}{D} \right)^2 \right] \quad (\text{B.74})$$

The ratio of geometric flow area to effective flow area,  $A/A_{eff}$ , can be approximated using equation (B.74) as

$$\frac{A}{A_{eff}} \approx 1 + 4\frac{\delta^*}{D} \quad (\text{B.75})$$

## B.4 General Model with Losses

Equation (B.43) can be expanded to include losses

$$\begin{aligned}
\frac{P_{t,d} - P_{t,s,us}}{P_{t,m}} &= \left( \frac{C_{F,isen}}{2} - \frac{C_{f,m} + C_{f,cc}}{2} \right) \frac{A_m^*}{A_d} + \dots \\
&+ \frac{1}{2} C_d^2 \left[ \frac{3\kappa - 1}{4} - \epsilon \frac{A_m^*}{A_d} \right] \frac{P_{t,s,us} - P_s}{P_{t,m}} + \dots \\
&+ \left[ \frac{\kappa - 3}{4} \right] \frac{P_{t,s,us} - P_d}{P_{t,m}}
\end{aligned} \tag{B.76}$$

$$\begin{aligned}
\frac{P_{t,d} - P_{t,s,us}}{P_{t,m}} &= \frac{C_{F,isen}}{2} \frac{A_m^*}{A_d} + \dots \\
&+ \frac{3}{\cos \theta_m} C R e_{D_m^*}^{-m} \left( \frac{L}{D_m^*} \right)^{1-n} + \dots \\
&+ \frac{1/2 \rho_m u_{m,e}^2}{P_{t,m}} \epsilon \frac{4 C R e_{D_{m,e}}^{-m}}{\cos \theta_{cc}} \left( \frac{L_{cc}}{D_{m,e}} \right)^{1-n} \frac{1}{m+2} + \dots \\
&+ \frac{1}{2} C_d^2 \left[ \frac{3\kappa - 1}{4} - \epsilon \frac{A_m^*}{A_d} \right] \frac{P_{t,s,us} - P_s}{P_{t,m}} + \dots \\
&+ \left[ \frac{\kappa - 3}{4} \right] \frac{P_{t,s,us} - P_d}{P_{t,m}}
\end{aligned} \tag{B.77}$$

Displacement boundary layer blockage can be included by using the effective area ratio,  $A_d/A_{d,eff}$  from equation (B.75). An alternate form of equation B.77 which explicitly shows blockage terms is given as

$$\begin{aligned}
\frac{P_{t,d} - P_{t,s}}{P_{t,m}} &\approx \frac{C_{F,m,isen} A_m^* A_d}{2 A_d A_{d,eff}} + \dots \\
&- \frac{3}{\cos \theta_m} C R e_{D_m^*}^{-m} \left( \frac{L}{D_m^*} \right)^{1-n} + \dots \\
&- \frac{1/2 \rho_m u_{m,e,isen}^2}{\cos \theta_{cc}} 4 C R e_{D_m^*}^{-m} \epsilon_m \left( \frac{L}{D_m^*} \right)^{1-n} \frac{1}{(m+2)} + \dots \quad (\text{B.78}) \\
&+ \frac{1}{2} \frac{\rho_s u_s^2}{P_{t,m}} \left( \frac{A_s}{A_d} \frac{A_d}{A_{d,eff}} - \frac{1}{C_d^2} \right) + \dots \\
&+ \frac{P_d - P_s}{P_{t,m}} \left[ 1 - \frac{1}{4} \left( 1 + \frac{A_s}{A_d} \frac{A_d}{A_{d,eff}} \left( 1 + \frac{A_{m,e}}{A_s} \right) \right) \right]
\end{aligned}$$

The constants  $C$ ,  $m$  and  $n$  are determined based on flow regime using Table B.1.

# Appendix C

## Nozzle Skin Friction Integral Tables

### C.1 Newton-Cotes Numerical Integration

This appendix provides tabulated values for the integral used to compute the nozzle wall drag,  $\int_{x/L=0}^{x/L=1} f(M) \frac{dx}{L}$ , for different values of  $\gamma$  for an axisymmetric 1-D nozzle expanding at a half-angle of  $\theta = 15^\circ$ . The function  $f(M)$  is numerically integrated using the Newton-Cotes ‘trapezoid rule’. The drag force from the nozzle wall is derived in Appendix A and is given by

$$F_{drag,m} = \frac{1}{\cos \theta} P_{t,m} A_m^* C Re_{D_m^*}^{-m} \left( \frac{L}{D_m^*} \right)^{1-n} 2^\gamma \left( \frac{\gamma+1}{2} \right)^{-\frac{m+1}{4} \frac{\gamma+1}{\gamma-1}} \int_{x/L=0}^{x/L=1} f(M) \frac{dx}{L} \quad (\text{C.1})$$

where

$$f(M) = \frac{M(x)^{\frac{3-m}{2}}}{\left( 1 + \frac{\gamma-1}{2} M(x)^2 \right)^{\frac{(3-m)\gamma-(m+1)}{4(\gamma-1)}}} \quad (\text{C.2})$$

The constants  $C$ ,  $m$  and  $n$  depend on flow regime and appear in Table 1.1 [34, 35]

and are also provided below.

Table C.1: Skin friction flow regime constants

| <i>Skin Friction</i> | <i>C</i> | <i>m</i> | <i>n</i> |
|----------------------|----------|----------|----------|
| Turbulent            | 0.046    | 1/5      | 0        |
| Laminar entry        | 3.72     | 2/3      | 1/3      |
| Laminar developed    | 16       | 1        | 0        |

## C.2 Tables for $\gamma = 1.1$

Table C.2: Nozzle integrals and parameters for  $\gamma = 1.1$

| $\gamma = 1.1$ |           | $\theta$  |           |       | $f(M)$  |       | $\int_{x/L=0}^{x/L=1} f(M) \frac{dx}{L}$ |      |      |      |      |      |      |
|----------------|-----------|-----------|-----------|-------|---------|-------|--|------|------|------|------|------|------|
| $M$            | $P_t/P_e$ | $A_e/A^*$ | $D_e/D^*$ | 15°   | 20°     | 30°   | 45°                                      | $m$  | $m$  |      |      |      |      |
|                |           |           |           |       | $L/D^*$ |       |  |      |      |      |      |      |      |
| 1.00           | 1.71      | 1.00      | 1.00      | 0.00  | 0.00    | 0.00  | 0.00                                     | 0.80 | 0.67 | 1.00 | 0.20 | 0.67 | 1.00 |
| 1.20           | 2.15      | 1.04      | 1.02      | 0.02  | 0.02    | 0.02  | 0.03                                     | 0.93 | 1.06 | 1.16 | 0.86 | 0.98 | 1.07 |
| 1.40           | 2.80      | 1.14      | 1.07      | 0.07  | 0.07    | 0.08  | 0.10                                     | 1.03 | 1.20 | 1.34 | 0.95 | 1.09 | 1.20 |
| 1.60           | 3.76      | 1.33      | 1.15      | 0.16  | 0.16    | 0.18  | 0.21                                     | 1.10 | 1.32 | 1.51 | 1.01 | 1.18 | 1.32 |
| 1.80           | 5.22      | 1.61      | 1.27      | 0.28  | 0.29    | 0.31  | 0.38                                     | 1.12 | 1.42 | 1.67 | 1.06 | 1.26 | 1.44 |
| 2.00           | 7.43      | 2.03      | 1.43      | 0.44  | 0.45    | 0.49  | 0.60                                     | 1.12 | 1.49 | 1.83 | 1.08 | 1.33 | 1.55 |
| 2.20           | 10.85     | 2.65      | 1.63      | 0.65  | 0.67    | 0.73  | 0.89                                     | 1.09 | 1.54 | 1.97 | 1.09 | 1.39 | 1.66 |
| 2.40           | 16.18     | 3.56      | 1.89      | 0.92  | 0.94    | 1.02  | 1.25                                     | 1.04 | 1.57 | 2.11 | 1.08 | 1.44 | 1.78 |
| 2.60           | 24.60     | 4.90      | 2.21      | 1.26  | 1.29    | 1.40  | 1.72                                     | 0.97 | 1.58 | 2.25 | 1.06 | 1.48 | 1.88 |
| 2.80           | 38.02     | 6.90      | 2.63      | 1.68  | 1.73    | 1.88  | 2.30                                     | 0.89 | 1.58 | 2.37 | 1.03 | 1.50 | 1.99 |
| 3.00           | 59.57     | 9.88      | 3.14      | 2.22  | 2.28    | 2.47  | 3.03                                     | 0.81 | 1.56 | 2.49 | 0.99 | 1.52 | 2.10 |
| 3.20           | 94.42     | 14.38     | 3.79      | 2.89  | 2.97    | 3.22  | 3.95                                     | 0.73 | 1.53 | 2.60 | 0.94 | 1.53 | 2.20 |
| 3.40           | 151.07    | 21.19     | 4.60      | 3.73  | 3.83    | 4.16  | 5.10                                     | 0.65 | 1.49 | 2.71 | 0.88 | 1.52 | 2.30 |
| 3.60           | 243.52    | 31.57     | 5.62      | 4.78  | 4.92    | 5.33  | 6.53                                     | 0.57 | 1.45 | 2.80 | 0.82 | 1.51 | 2.40 |
| 3.80           | 394.79    | 47.43     | 6.89      | 6.09  | 6.26    | 6.80  | 8.33                                     | 0.50 | 1.40 | 2.90 | 0.76 | 1.49 | 2.50 |
| 4.00           | 642.68    | 71.75     | 8.47      | 7.73  | 7.95    | 8.63  | 10.56                                    | 0.44 | 1.34 | 2.98 | 0.70 | 1.47 | 2.59 |
| 4.20           | 1049.10   | 109.09    | 10.44     | 9.78  | 10.05   | 10.91 | 13.36                                    | 0.38 | 1.29 | 3.06 | 0.64 | 1.43 | 2.68 |
| 4.40           | 1715.05   | 166.47    | 12.90     | 12.32 | 12.67   | 13.74 | 16.83                                    | 0.33 | 1.23 | 3.14 | 0.58 | 1.40 | 2.77 |
| 4.60           | 2804.78   | 254.64    | 15.96     | 15.49 | 15.92   | 17.27 | 21.15                                    | 0.28 | 1.17 | 3.21 | 0.52 | 1.36 | 2.85 |
| 4.80           | 4584.21   | 390.05    | 19.75     | 19.41 | 19.95   | 21.65 | 26.52                                    | 0.25 | 1.11 | 3.27 | 0.47 | 1.31 | 2.93 |
| 5.00           | 7481.83   | 597.67    | 24.45     | 24.27 | 24.95   | 27.07 | 33.16                                    | 0.21 | 1.05 | 3.33 | 0.42 | 1.27 | 3.00 |

### C.3 Tables for $\gamma = 1.2$

Table C.3: Nozzle integrals and parameters for  $\gamma = 1.2$

| $\gamma = 1.2$ |           | $\theta$  |           |         | $f(M)$ |      | $f_{x/L=0}^{x/L=1} f(M) \frac{dx}{L}$ |      |      |      |      |
|----------------|-----------|-----------|-----------|---------|--------|------|---------------------------------------|------|------|------|------|
|                |           | 15°       | 20°       | 30°     | 45°    | $m$  | $m$                                   | $m$  |      |      |      |
| $M$            | $P_t/P_e$ | $A_e/A^*$ | $D_e/D^*$ | $L/D^*$ |        |      |                                       |      |      |      |      |
| 1.00           | 1.77      | 1.00      | 1.00      | 0.00    | 0.00   | 0.77 | 0.87                                  | 1.00 | 0.20 | 0.67 | 1.00 |
| 1.20           | 2.24      | 1.03      | 1.02      | 0.02    | 0.02   | 0.90 | 1.02                                  | 1.12 | 0.84 | 0.95 | 1.04 |
| 1.40           | 2.93      | 1.13      | 1.06      | 0.07    | 0.07   | 0.99 | 1.15                                  | 1.28 | 0.91 | 1.05 | 1.16 |
| 1.60           | 3.93      | 1.30      | 1.14      | 0.14    | 0.15   | 1.04 | 1.25                                  | 1.43 | 0.97 | 1.13 | 1.26 |
| 1.80           | 5.39      | 1.54      | 1.24      | 0.25    | 0.26   | 1.07 | 1.33                                  | 1.56 | 1.01 | 1.20 | 1.36 |
| 2.00           | 7.53      | 1.88      | 1.37      | 0.39    | 0.40   | 1.06 | 1.39                                  | 1.69 | 1.03 | 1.26 | 1.46 |
| 2.20           | 10.68     | 2.36      | 1.54      | 0.55    | 0.57   | 1.04 | 1.43                                  | 1.81 | 1.03 | 1.31 | 1.55 |
| 2.40           | 15.32     | 3.01      | 1.74      | 0.76    | 0.78   | 1.00 | 1.46                                  | 1.91 | 1.03 | 1.34 | 1.63 |
| 2.60           | 22.16     | 3.90      | 1.97      | 1.01    | 1.04   | 0.94 | 1.47                                  | 2.01 | 1.02 | 1.37 | 1.71 |
| 2.80           | 32.24     | 5.10      | 2.26      | 1.30    | 1.34   | 0.89 | 1.46                                  | 2.10 | 0.99 | 1.39 | 1.79 |
| 3.00           | 47.05     | 6.74      | 2.60      | 1.65    | 1.70   | 0.82 | 1.45                                  | 2.18 | 0.96 | 1.41 | 1.86 |
| 3.20           | 68.75     | 8.94      | 2.99      | 2.06    | 2.12   | 0.76 | 1.43                                  | 2.25 | 0.93 | 1.41 | 1.93 |
| 3.40           | 100.44    | 11.91     | 3.45      | 2.54    | 2.61   | 0.70 | 1.40                                  | 2.32 | 0.89 | 1.41 | 2.00 |
| 3.60           | 146.50    | 15.90     | 3.99      | 3.09    | 3.18   | 0.64 | 1.37                                  | 2.38 | 0.85 | 1.41 | 2.06 |
| 3.80           | 213.11    | 21.24     | 4.61      | 3.74    | 3.84   | 0.58 | 1.34                                  | 2.43 | 0.81 | 1.40 | 2.12 |
| 4.00           | 308.92    | 28.36     | 5.32      | 4.48    | 4.60   | 0.53 | 1.30                                  | 2.48 | 0.77 | 1.39 | 2.17 |
| 4.20           | 445.89    | 37.81     | 6.15      | 5.33    | 5.48   | 0.48 | 1.26                                  | 2.53 | 0.73 | 1.37 | 2.23 |
| 4.40           | 640.53    | 50.30     | 7.09      | 6.31    | 6.48   | 0.43 | 1.22                                  | 2.57 | 0.68 | 1.35 | 2.28 |
| 4.60           | 915.34    | 66.74     | 8.17      | 7.42    | 7.63   | 0.39 | 1.19                                  | 2.61 | 0.64 | 1.33 | 2.32 |
| 4.80           | 1300.89   | 88.27     | 9.40      | 8.69    | 8.93   | 0.36 | 1.15                                  | 2.64 | 0.60 | 1.31 | 2.37 |
| 5.00           | 1838.27   | 116.34    | 10.79     | 10.13   | 10.41  | 0.32 | 1.11                                  | 2.67 | 0.57 | 1.28 | 2.41 |

## C.4 Tables for $\gamma = 1.3$

Table C.4: Nozzle integrals and parameters for  $\gamma = 1.3$

| $M$       |           | $\gamma = 1.3$ |         | $\theta$ |      |      | $f(M)$ |      | $\int_{x/L=0}^{x/L=1} f(M) \frac{dx}{L}$ |      |      |
|-----------|-----------|----------------|---------|----------|------|------|--------|------|--|------|------|
|           |           |                |         | 15°      | 20°  | 30°  | 45°    | $m$  | $m$                                      | $m$  | $m$  |
| $P_t/P_e$ | $A_e/A^*$ | $D_e/D^*$      | $L/D^*$ |          |      | $m$  |        | $m$  |  | $m$  |      |
| 1.00      | 1.83      | 1.00           | 0.00    | 0.00     | 0.00 | 0.75 | 0.85   | 1.00 | 0.20                                     | 0.67 | 1.00 |
| 1.20      | 2.33      | 1.03           | 0.02    | 0.02     | 0.02 | 0.87 | 0.99   | 1.09 | 0.00                                     | 0.00 | 0.00 |
| 1.40      | 3.06      | 1.12           | 0.06    | 0.06     | 0.07 | 0.95 | 1.10   | 1.23 | 0.81                                     | 0.92 | 1.01 |
| 1.60      | 4.09      | 1.27           | 0.13    | 0.14     | 0.15 | 1.00 | 1.20   | 1.36 | 0.88                                     | 1.01 | 1.12 |
| 1.80      | 5.56      | 1.48           | 0.23    | 0.23     | 0.25 | 1.02 | 1.26   | 1.48 | 0.93                                     | 1.09 | 1.21 |
| 2.00      | 7.67      | 1.77           | 0.34    | 0.35     | 0.38 | 1.01 | 1.31   | 1.58 | 0.96                                     | 1.15 | 1.30 |
| 2.20      | 10.65     | 2.16           | 0.48    | 0.50     | 0.54 | 0.99 | 1.35   | 1.67 | 0.98                                     | 1.19 | 1.38 |
| 2.40      | 14.86     | 2.65           | 0.65    | 0.67     | 0.73 | 0.96 | 1.37   | 1.76 | 0.99                                     | 1.23 | 1.45 |
| 2.60      | 20.78     | 3.30           | 0.84    | 0.87     | 0.94 | 0.92 | 1.37   | 1.83 | 0.98                                     | 1.27 | 1.52 |
| 2.80      | 29.05     | 4.12           | 1.07    | 1.09     | 1.19 | 0.87 | 1.37   | 1.90 | 0.97                                     | 1.29 | 1.58 |
| 3.00      | 40.55     | 5.16           | 1.32    | 1.35     | 1.47 | 0.82 | 1.36   | 1.96 | 0.96                                     | 1.31 | 1.64 |
| 3.20      | 56.40     | 6.48           | 1.60    | 1.64     | 1.78 | 0.82 | 1.36   | 1.96 | 0.94                                     | 1.32 | 1.70 |
| 3.40      | 78.13     | 8.13           | 1.92    | 1.97     | 2.14 | 0.77 | 1.35   | 2.01 | 0.91                                     | 1.32 | 1.75 |
| 3.60      | 107.66    | 10.20          | 2.27    | 2.33     | 2.53 | 0.72 | 1.33   | 2.06 | 0.88                                     | 1.33 | 1.79 |
| 3.80      | 147.53    | 12.77          | 2.66    | 2.74     | 2.97 | 0.67 | 1.30   | 2.10 | 0.85                                     | 1.32 | 1.84 |
| 4.00      | 200.94    | 15.94          | 3.10    | 3.19     | 3.46 | 0.62 | 1.28   | 2.14 | 0.82                                     | 1.32 | 1.88 |
| 4.20      | 271.98    | 19.85          | 3.58    | 3.68     | 3.99 | 0.58 | 1.25   | 2.17 | 0.79                                     | 1.31 | 1.92 |
| 4.40      | 365.77    | 24.62          | 4.10    | 4.22     | 4.58 | 0.54 | 1.22   | 2.20 | 0.76                                     | 1.30 | 1.95 |
| 4.60      | 488.72    | 30.43          | 4.68    | 4.81     | 5.22 | 0.50 | 1.19   | 2.23 | 0.73                                     | 1.29 | 1.99 |
| 4.80      | 648.78    | 37.47          | 5.30    | 5.45     | 5.91 | 0.46 | 1.17   | 2.25 | 0.70                                     | 1.28 | 2.02 |
| 5.00      | 855.73    | 45.96          | 5.98    | 6.15     | 6.67 | 0.43 | 1.14   | 2.27 | 0.67                                     | 1.26 | 2.05 |
|           |           |                |         |          |      | 0.40 | 1.11   | 2.29 | 0.64                                     | 1.25 | 2.07 |

## C.5 Tables for $\gamma = 1.4$

Table C.5: Nozzle integrals and parameters for  $\gamma = 1.4$

| $M$  |        | $\gamma = 1.4$ |           | $\theta$  |      |      | $f(M)$ |      | $\int_{x/L=0}^{x/L=1} f(M) \frac{dx}{L}$ |      |      |      |      |      |      |
|------|--------|----------------|-----------|-----------|------|------|--------|------|--|------|------|------|------|------|------|
|      |        | $P_t/P_e$      | $A_e/A^*$ | $D_e/D^*$ | 15°  | 20°  | 30°    | 45°  | $m$                                      | $m$  |      |      |      |      |      |
| 1.00 | 1.89   | 1.00           | 1.00      | 1.00      | 0.00 | 0.00 | 0.00   | 0.73 | 0.83                                     | 0.91 | 0.20 | 0.67 | 1.00 | 0.00 | 0.00 |
| 1.20 | 2.42   | 1.03           | 1.02      | 0.02      | 0.02 | 0.02 | 0.02   | 0.84 | 0.96                                     | 1.06 | 0.79 | 0.90 | 0.99 | 0.79 | 0.90 |
| 1.40 | 3.18   | 1.11           | 1.06      | 0.06      | 0.06 | 0.06 | 0.08   | 0.91 | 1.06                                     | 1.19 | 0.85 | 0.98 | 1.09 | 0.85 | 0.98 |
| 1.60 | 4.25   | 1.25           | 1.12      | 0.12      | 0.13 | 0.14 | 0.17   | 0.96 | 1.14                                     | 1.30 | 0.90 | 1.05 | 1.17 | 0.90 | 1.05 |
| 1.80 | 5.75   | 1.44           | 1.20      | 0.21      | 0.21 | 0.23 | 0.28   | 0.97 | 1.20                                     | 1.40 | 0.92 | 1.10 | 1.24 | 0.92 | 1.10 |
| 2.00 | 7.82   | 1.69           | 1.30      | 0.31      | 0.32 | 0.35 | 0.42   | 0.97 | 1.25                                     | 1.49 | 0.94 | 1.14 | 1.31 | 0.94 | 1.14 |
| 2.20 | 10.69  | 2.00           | 1.42      | 0.43      | 0.44 | 0.48 | 0.59   | 0.95 | 1.27                                     | 1.57 | 0.95 | 1.17 | 1.37 | 0.95 | 1.17 |
| 2.40 | 14.62  | 2.40           | 1.55      | 0.57      | 0.59 | 0.64 | 0.78   | 0.93 | 1.29                                     | 1.64 | 0.94 | 1.20 | 1.43 | 0.94 | 1.20 |
| 2.60 | 19.95  | 2.90           | 1.70      | 0.73      | 0.75 | 0.81 | 0.99   | 0.89 | 1.30                                     | 1.70 | 0.94 | 1.22 | 1.48 | 0.94 | 1.22 |
| 2.80 | 27.14  | 3.50           | 1.87      | 0.90      | 0.93 | 1.01 | 1.23   | 0.85 | 1.29                                     | 1.75 | 0.92 | 1.24 | 1.53 | 0.92 | 1.24 |
| 3.00 | 36.73  | 4.23           | 2.06      | 1.10      | 1.13 | 1.22 | 1.50   | 0.81 | 1.29                                     | 1.79 | 0.91 | 1.25 | 1.57 | 0.91 | 1.25 |
| 3.20 | 49.44  | 5.12           | 2.26      | 1.31      | 1.34 | 1.46 | 1.79   | 0.77 | 1.27                                     | 1.83 | 0.89 | 1.25 | 1.61 | 0.89 | 1.25 |
| 3.40 | 66.12  | 6.18           | 2.49      | 1.54      | 1.58 | 1.72 | 2.10   | 0.72 | 1.26                                     | 1.87 | 0.87 | 1.25 | 1.65 | 0.87 | 1.25 |
| 3.60 | 87.84  | 7.45           | 2.73      | 1.79      | 1.84 | 2.00 | 2.45   | 0.68 | 1.24                                     | 1.90 | 0.84 | 1.25 | 1.68 | 0.84 | 1.25 |
| 3.80 | 115.89 | 8.95           | 2.99      | 2.06      | 2.12 | 2.30 | 2.82   | 0.64 | 1.22                                     | 1.93 | 0.82 | 1.25 | 1.71 | 0.82 | 1.25 |
| 4.00 | 151.84 | 10.72          | 3.27      | 2.35      | 2.42 | 2.63 | 3.22   | 0.61 | 1.20                                     | 1.95 | 0.80 | 1.24 | 1.74 | 0.80 | 1.24 |
| 4.20 | 197.55 | 12.79          | 3.58      | 2.67      | 2.74 | 2.98 | 3.64   | 0.57 | 1.18                                     | 1.97 | 0.77 | 1.24 | 1.76 | 0.77 | 1.24 |
| 4.40 | 255.26 | 15.21          | 3.90      | 3.00      | 3.09 | 3.35 | 4.10   | 0.54 | 1.16                                     | 1.99 | 0.75 | 1.23 | 1.79 | 0.75 | 1.23 |
| 4.60 | 327.59 | 18.02          | 4.24      | 3.36      | 3.45 | 3.75 | 4.59   | 0.51 | 1.13                                     | 2.01 | 0.72 | 1.22 | 1.81 | 0.72 | 1.22 |
| 4.80 | 417.66 | 21.26          | 4.61      | 3.74      | 3.84 | 4.17 | 5.11   | 0.48 | 1.11                                     | 2.03 | 0.70 | 1.21 | 1.83 | 0.70 | 1.21 |
| 5.00 | 529.09 | 25.00          | 5.00      | 4.14      | 4.26 | 4.62 | 5.66   | 0.45 | 1.09                                     | 2.04 | 0.68 | 1.20 | 1.85 | 0.68 | 1.20 |

# Bibliography

- [1] A. H. Epstein, S. D. Senturia, O. Al-Midani, G. Anathasuresh, A. Ayon, K. Breuer, K. S. Chen, F. E. Ehrich, E. Esteve, L. Fréchette, G. Gauba, R. Ghodssi, C. Groshenry, S. Jacobson, J. L. Kerrebrock, J. H. Lang, C. C. Lin, A. London, J. Lopata, A. Mehra, J. O. Mur Miranda, S. Nagle, D. J. Orr, E. Piekos, M. A. Schmidt, G. Shirley, S. M. Spearing, C. S. Tan, T. S. Tzeng, and I. A. Waitz. Micro-heat engines, gas turbines, and rocket engines - the mit microengine project. In *28<sup>th</sup> AIAA Fluid Dynamics Conference*. Paper AIAA-97-1773, 1997.
- [2] R.L. Bayt, A. A. Ayón, and K.S. Breuer. A performance evaluation of mems-based micronozzles. In *33rd AIAA/ASME/SAE/ASEE Joint Propulsion Conference and Exhibit*. AIAA/ASME/SAE/ASEE, July 3-9 1997. AIAA-97-3169.
- [3] R.L. Bayt and K.S. Breuer. Viscous effects in supersonic mems-fabricated micronozzles. In *Proceedings of the 3rd ASME Microfluids Symposium*. ASME, 1998.
- [4] J. M. Protz. *An Assessment of the Aerodynamic, Thermodynamic, and Manufacturing Issues for the Design, Development, and Microfabrication of a Demonstration Micro Engine*. PhD thesis, Massachusetts Institute of Technology, September 2000.
- [5] A.P. London. *Development and test of a microfabricated bipropellant rocket engine*. PhD thesis, Massachusetts Institute of Technology, 2000.
- [6] A. Mehra. Computational investigation and design of low Reynolds number micro-turbomachinery. Master's thesis, Massachusetts Institute of Technology, June 1997.
- [7] A. Mehra. *Development of a High Power Density Combustion System for a Silicon Micro Gas Turbine Engine*. PhD thesis, Massachusetts Institute of Technology, February 2000.
- [8] A.A. Ayón, R.L. Bayt, and K.S. Bruer. Deep reactive ion etching: a promising technology for micro- and nanosatellites. *Z. Angew. Math. Phys.*, 10:1135–1144, 2001.

- [9] S.A. Jacobson and A.H. Epstein. An informal survey of power mems. In *International Symposium on Micro-Mechanical Engineering*. Paper ISMME2003-K18, December 2003.
- [10] L. Cui. Design and system analysis of micro-scale rankine cycle power systems. Master's thesis, Massachusetts Institute of Technology, 2003.
- [11] J. J. Peck. Development of a catalytic combustion system for the mit micro gas turbine engine. Master's thesis, Massachusetts Institute of Technology, September 2003.
- [12] S. Diez. Preliminary performance characteristics of a microfabricated turbopump. Master's thesis, Massachusetts Institute of Technology, September 2003.
- [13] L. G. Fr chet, C. Lee, S. Arslan, and Y. C. Liu. Design of a microfabricated rankine cycle steam turbine for power generation. In *ASME International Mechanical Engineering Congress and Exposition*. Paper IMECE2003-42082, 2003.
- [14] C.S. Protz. *Experimental investigation of microfabricated bipropellant rocket engines*. PhD thesis, Massachusetts Institute of Technology, 2004.
- [15] N. Savoulides. *Development of a MEMS Turbocharger and Gas Turbine Engine*. PhD thesis, Massachusetts Institute of Technology, 2004.
- [16] A.H. Epstein. Millimeter-scale, micro-electro-mechanical systems gas turbine engines. *Journal of Engineering for Gas Turbines and Power*, 126:205–226, April 2004.
- [17] L. G. Fr chet, C. Lee, and S. Arslan. Development of a mems-based rankine cycle steam turbine for power generation: Project status. In *4<sup>th</sup> International Workshop on Micro and Nano Technology for Power Generation and Energy Conversion Applications, Kyoto, Japan*, pages 92–95. Power MEMS '04, 2004.
- [18] B.C.H Yen. *A fully-integrated multi-watt permanent-magnet turbine generator*. PhD thesis, Massachusetts Institute of Technology, 2008.
- [19] L.G. Fr chet, S.A. Jacobson, K.S. Breuer, F.F. Ehrich, R. Ghodssi, R. Khanna, C.W. Wong, X. Zhang, M.A. Schmidt, and A.H. Epstein. High-speed microfabricated silicon turbomachinery and fluid film bearings. *Micro-electromechanical Systems, Journal of*, 14(1), 2005.
- [20] C. J. Teo. *MEMS Turbomachinery Rotordynamics: Modeling, Design and Testing*. PhD thesis, Massachusetts Institute of Technology, June 2006.

- [21] N. Savoulides, S. A. Jacobson, H. Li, L. Ho, R. Khanna, C. J. Teo, J. M. Protz, L. Wang, D. Ward, M. A. Schmidt, and A. H. Epstein. Fabrication and testing of a high-speed microscale turbocharger. *Journal of Microelectromechanical Systems*, 17(5), July 2008.
- [22] L. G. Fréchette, C. Lee, and S. Arslan. Design principles and measured performance of multistage radial flow microturbomachinery at low reynolds numbers. *Journal of Fluids Engineering*, 130(111103), 2008.
- [23] J. J. Peck. *Development of a Liquid-Fueled Micro-Combustor*. PhD thesis, Massachusetts Institute of Technology, June 2008.
- [24] F. Herrault. *Microfabricated air-turbine and heat-engine-driven permanent-magnet generators*. PhD thesis, University of Toulouse, 2009.
- [25] J. Lang. *Multi-Wafer Rotating MEMS Machines: Turbines, Generators, and Engines*. Springer, 2009.
- [26] L. G. Fréchette and C. Lee. A silicon microturbopump for a rankine-cycle power generation microsystem– part i: Component and system design. *Journal of Microelectromechanical Systems*, 20(1), February 2011.
- [27] C. Lee, L. Mokhtar, and L. G. Fréchette. A silicon microturbopump for a rankine-cycle power generation microsystem– part ii: Fabrication and characterization. *Journal of Microelectromechanical Systems*, 20(1), February 2011.
- [28] F.H. Cocks. *Energy Demand and Climate Change: Issues and Resolutions*. Wiley-VCH Verlag GmbH & Co, Weinheim, DE, 2009.
- [29] J.L. Kerrebrock. *Aircraft Engines and Gas Turbines*. The MIT Press, Cambridge, Massachusetts, 2<sup>nd</sup> edition, 1992.
- [30] J.D. Mattingly, the American Institute of Aeronautics, and Astronautics. *Elements of propulsion: gas turbines and rockets*. American Institute of Aeronautics and Astronautics, 2006.
- [31] W.G. Gardner, I. Wang, J.W. Jaworski, N.A. Brikner, and J.M. Protz. Experimental investigation and modeling of scale effects in jet ejectors. *Journal of Micromechanics and Microengineering*, 20:085027, 2010.
- [32] A.P. Camacho, I. Wang, J.W. Jaworski, and J.M. Protz. Scaling effects on the efficiency of micro-scale gas turbines. In *The 10th International Workshop on Micro and Nanotechnology for Power Generation and Energy Conversion Applications*. Power MEMS '10, 2010.
- [33] A. P. Camacho. The design of a micro-turbogenerator. Master's thesis, Duke University, May 2011.

- [34] Y.A. Cengel. *Heat and Mass Transfer: Fundamentals and Applications*. McGraw–Hill, New York, 3rd edition, 2003.
- [35] F.P. Incropera and D.P. DeWitt. *Fundamentals of Heat and Mass Transfer*. John Wiley & Sons, Inc., New Jersey, 5 edition, 2002.
- [36] G.P. Sutton. *Rocket Propulsion Elements: An Introduction to the Engineering of Rockets*. John Wiley and Sons, Inc., 6th edition, 1992.
- [37] E.M. Greitzer, C.S. Tan, and M.B. Graf. *Internal Flows: Concepts and Applications*. Cambridge University Press, Cambridge, UK, 2004.
- [38] S. Jovanovic. Design of a 50-watt air supplied turbogenerator. Master’s thesis, Massachusetts Institute of Technology, June 2008.
- [39] A.P. London, A.A. Ayón, A.H. Epstein, and S.M. Spearing. Microfabrication of a high pressure bipropellant rocket engine. *Sensors and Actuators*, 92(1):351–357, 2001.
- [40] D.G. Shepherd. *The Principles of Turbomachinery*. MacMillan Publishing Company, New York, 1956.
- [41] C.J. Teo, L.X. Liu, H.Q. Li, L.C. Ho, S.A. Jacobson, F.F. Ehrich, A.H. Epstein, and Z.S. Spakovszky. High-speed operation of a gas-bearing supported mems-air turbine. *Journal of Tribology*, 131, July 2009.
- [42] Z.S. Spakovszky and L.X. Liu. Scaling laws for ultra-short hydrostatic gas journal bearings. In *Transactions of the ASME, Journal of Vibrations and Acoustics*, volume 127, pages 254–261, 2005.
- [43] S.F. Bart, L.S. Tavrow, M. Mehregany, and J.H. Lang. Microfabricated electrohydrodynamic pumps. In *Sensors and Actuators, A21-A23*, pages 193–197.
- [44] P. Woias. Micropumps– past, progress and future prospects. *Sensors and Actuators B*, 105:28–38, 2005.
- [45] D.J. Laser and J.G. Santiago. A review of micropumps. *Journal of Micromechanics and Microengineering*, 14:R35–R36, 2004.
- [46] N. Nguyen, X. Huang, and T. K. Chuan. Mems-micropumps: A review. *Transactions of the ASME*, 124:382–392, June 2002.
- [47] P.W.B. Semmens and A.J. Goldfinch. *How Steam Locomotives Really Work*. Oxford University Press, New York, NY, 2000.
- [48] W.G. Gardner, J.W. Jaworski, A.P. Camacho, and J.M. Protz. Experimental results for a microscale ethanol vapor jet ejector. *Journal of Micromechanics and Microengineering*, 20:045019, 2010.

- [49] N. A. Brikner. Modeling and analysis of a giffard injector-pumped bipropellant microrocket. Master's thesis, Duke University, May 2010.
- [50] N.A. Brikner, W.G. Gardner, I. Wang, and J.M. Protz. Modeling and design of a giffard injector-pumped bipropellant microrocket. In *The 10th International Workshop on Micro and Nanotechnology for Power Generation and Energy Conversion Applications*. Power MEMS '10, 2010.
- [51] N.A. Brikner, W.G. Gardner, and J.M. Protz. A study and design of a giffard injector-pumped bipropellant microrocket. In *57th JANNAF Propulsion Meeting*. AIAA/ASME/SAE/ASEE, May 3-7 2010.
- [52] N.A. Brikner, W.G. Gardner, and J.M. Protz. A design of a giffard injector-pumped bipropellant microrocket. In *Proceedings of the 46th Joint Propulsion Conference & Exhibit*. AIAA/ASME/SAE/ASEE, July 25-28 2010.
- [53] W.G. Gardner, J.W. Jaworski, I. Wang, N.A. Brikner, and J.M. Protz. Microscale ethanol vapor ejector and injector. In *Proceedings of SPIE Micro and Nanotechnology Sensors, Systems and Applications II, April 5-9*, pages 7679–98. SPIE, 2010.
- [54] B.A. Wilhite, C. Livermore, Y. Gong, A.H. Epstein, and K. F. Jensen. Design of a mems-based microchemical oxygen-iodine laser ( $\mu$ coil) system. *IEEE Journal of Quantum Electronics*, 40:1041–1055, 2004.
- [55] C. Livermore, T. Hill, B. Wilhite, L. Velasquez, and A.H. Epstein. Microtechnology for compact, efficient high-power lasers. In *SPIE Newsroom*. SPIE, September 2007.
- [56] F. Eid, L.F. Velasquez-Garcia, and C. Livermore. Design, fabrication and demonstration of a MEMS steam generator for ejector pump applications. *Journal of Micromechanics and Microengineering*, 20:551–561, 2010.
- [57] K. Isomura, M. Murama, S. Teramoto, K. Hikichi, Y. Endo, S. Togo, and S. Tanaka. Experimental verification of the feasibility of a 100 W class micro-scale gas turbine at an impeller diameter of 10 mm. *Journal of Micromechanics and Microengineering*, 16:254–261, 2006.
- [58] D. Satoh, S. Tanaka, K. Yoshida, and M. Esashi. A Micro-Ejector for a Micro-Combustor. pages 359–364, 2003.
- [59] S. Tanaka, K.S. Chang, K.B. Min, D. Satoh, K. Yoshida, and M. Esashi. MEMS-based components of a miniature fuel cell/fuel reformer system. *Chemical Engineering Journal*, 101:143–149, 2004.

- [60] Y. Fan, Y. Suzuki, and N. Kasagi. Development of large-entrainment-ratio micro ejector for catalytic combustor. In *Power MEMS*, pages 132–135, November 2005.
- [61] A. Bejan. *Advanced Engineering Thermodynamics*. John Wiley & Sons, New Jersey, 2006.
- [62] William F.M. Goss. *Locomotive Performance: The result of a series of researches conducted by the engineering laboratory of Purdue University*. John Wiley & Sons, New York, 1907.
- [63] W.F.M. Goss. American Engineer Tests: Locomotive Draft Appliances: Section V – Tables of Results. *American Engineer and Railroad Journal*, 77:70–76, 1903.
- [64] W.F.M. Goss. American Engineer Tests: Locomotive Draft Appliances: Section VI – Discussion of Results. *American Engineer and Railroad Journal*, 77:82–83, 1903.
- [65] W.F.M. Goss. American Engineer Tests: Locomotive Draft Appliances: Section VI – Diagrams. *American Engineer and Railroad Journal*, 77:149–155, 1903.
- [66] W.F.M. Goss. American Engineer Tests: Locomotive Draft Appliances: Section VI – Diagrams (continued). *American Engineer and Railroad Journal*, 77:162–164, 1903.
- [67] W.F.M. Goss. American Engineer Tests: Locomotive Draft Appliances: Section VII – Summary of Results. *American Engineer and Railroad Journal*, 77:239–241, 1903.
- [68] W.F.M. Goss. American Engineer Tests: Locomotive Draft Appliances: Section VII – Summary of Results (continued). *American Engineer and Railroad Journal*, 77:302–304, 1903.
- [69] W.F.M. Goss. American Engineer Tests: Locomotive Draft Appliances: Section VII – Summary of Results (concluded). *American Engineer and Railroad Journal*, 77:327–329, 1903.
- [70] H. Giffard. Improved-feed water apparatus for steam-boilers. United States Patent Number 27,979, April 24 1860.
- [71] Stickland L. Kneass. *Practice and Theory of the Injector*. John Wiley and Sons, Inc., New York, NY, 3rd edition, 1910.
- [72] M.H. Resal. *Reserches Theoriques sur les Effects Mechaniques de l’Injecteur Automoteur de M. Giffard*. E. Trunot, Paris, FR, 1862.

- [73] T. Crawford. *The Model Injector: Theory, design principles and details for making your own miniature live steam injector*. Australian Model Engineering, Higgins, AU, 2003.
- [74] M. Doms and J. Mueller. A Micromachined Vapor Jet Pump. *Sensors and Actuators A*, 119:462–467, 2004.
- [75] M. Doms and J. Mueller. Design, Fabrication, and Characterization of a Micro Vapor-Jet Vacuum Pump. *ASME Journal of Fluids Engineering*, 129:1339–1345, 2007.
- [76] W. Presz and M. Werle. Multi-Stage Mixer/Ejector Systems. *38th AIAA/ASME/SAE/ASEE Joint Propulsion Conference*, July 2002. AIAA 2002-4064.
- [77] A.E. Kroll. The Design of Jet Pumps. *Chemical Engineering Progress*, 1, 1947.
- [78] S. B. Riffat, G. Gan, and S. Smith. Computational fluid dynamics applied to ejector heat pumps. *Journal of Heat Recovery Systems*, 16(4):291–297, 1996.
- [79] S. B. Riffat and S. A. Omer. Cfd modeling and experimental investigation of an ejector refrigeration system using methanol as the working fluid. *International Journal of Energy Research*, 25:115–128, 2001.
- [80] T. Sriveerakul, S. Aphornratana, and K. Chunnanond. Performance prediction of steam ejector using computational fluid dynamics: Part 1. validation of the cfd results. *International Journal of Thermal Sciences*, 46:812–822, 2007.
- [81] H. El-Dessouky, H. Ettouney, I. Alatiqi, and G. Al-Nuwaibit. Evaluation of Steam Jet Ejectors. *Chemical Engineering and Processing*, 41:551–561, 2002.
- [82] J.H. Keenan, E.P. Neumann, and F. Lustwerk. An investigation of ejector design by analysis and experiment. Technical Report OCLC 11503176, MIT: Guided Missiles Program, 1948.
- [83] G.K. Batchelor. *An Introduction to Fluid Dynamics*. Cambridge University Press, New York, 1967.
- [84] F.M. White. *Viscous Fluid Flow*. McGraw-Hill, Inc., New York, NY, 1991.
- [85] A.H. Shapiro. *The Dynamics and Thermodynamics of Compressible Fluid Flow*, volume 1. The Roland Press Company, New York, 1953.
- [86] A.P. Camacho, W.G. Gardner, I. Wang, H. Shen, J.W. Jaworski, C. Gilmore, S.O. Pelekies, J.A. Dunnmon, and J.M. Protz. Experimental results of an ejector drive micro turbine generator. In *The 10th International Workshop on Micro and Nanotechnology for Power Generation and Energy Conversion Applications*. Power MEMS '10, 2010.

- [87] Engineering Sciences and Data Unit (EDSU). Ejector and jet pump design, 1986.
- [88] E. M. Greitzer, R. W. Patterson, and C. S. Tan. An approximate substitution principle for viscous heat conducting flows. *Proc. R. Soc. Lond. A*, 401:163–193, 1985.
- [89] W. Presz and E. Greitzer. A Useful Similarity Principle for Jet Engine Exhaust System Performance. *24th AIAA/ASME/SAE/ASEE Joint Propulsion Conference*, July 1988. AIAA 88-3001.
- [90] Y.A. Cengel and J. M. Cimbala. *Fluid Mechanics: Fundamentals and Applications*. McGraw–Hill, New York, 2006.
- [91] J.H. Horlock. *Advanced Gas Turbine Cycles*. Elsevier Science, Oxford, UK, 2003.
- [92] G. Cattadori, L. Galbiati, L. Mazzocchi, and P. Vanini. A single-stage high pressure steam injector for next generation reactors: Test results and analysis. *International Journal of Multiphase Flow*, 21(4):591–606, 1994.
- [93] Y. Abe, Y. Kawamoto, C. Iwaki, T. Narabayashi, M. Mori, and S. Ohmori. Heat transfer and flow characteristics of supersonic steam injector. In *Annals of the Assembly for International Heat Transfer Conference*, volume 13.
- [94] N. Deberne, J.F. Leone, A. Duque, and A. Lallemand. A model for calculation of steam injector performance. *International Journal of Multiphase Flow*, 25:841–855, 1999.
- [95] W. Sellers. Improvement in the giffard injector. United States Patent Number 39,313, July 21 1863.
- [96] D. R. Lide and ed. *CRC Handbook of Chemistry and Physics*. CRC Press, Boca Raton, FL, 2005.
- [97] A. Ugural. *Stresses in Plates and Shells*. McGraw-Hill, New York, NY, 2nd edition, 1999.
- [98] W.G. Gardner, I. Wang, J.W. Jaworski, N.A. Brikner, and J.M. Protz. Experimental investigation of scale effects in multi-stage ejectors. In *The 10th International Workshop on Micro and Nanotechnology for Power Generation and Energy Conversion Applications*. Power MEMS '10, 2010.
- [99] I.A. Waitz, Y.J. Qiu, T.A. Manning, A.K.S. Fung, J.K. Elliot, J.M. Kerwin, J.K. Krasnodebski, M.N. O’Sullivan, D.E. Tew, , E.M. Greitzer, F.E. Marble, C.S. Tan, and T.G. Tillman. Enhanced Mixing with Streamwise Vorticity. *Prog. Aerospace Sci.*, 33:323–351, 1997.

- [100] W.M. Presz, B.L. Morin, and R.G. Gousy. Forced Mixer Lobes in Ejector Designs. *J. Propulsion*, 4(4):350–355, July-August 1988.

# Biography

William Geoffrey Gardner was born on May 23, 1984 in New Orleans, Louisiana. He graduated from Duke University in 2009 with a B.S.E. in Mechanical Engineering and Materials Science. He is the 2010 recipient of the Dean's Award for Excellence in Mentoring. William is the inventor or co-inventor on two US patent applications and has authored or co-authored the following publications:

*Peer reviewed*

Gardner, W G, Wang, I, Jaworski, J W, Brikner, N A, Protz, J M, "Experimental investigation and modeling of scale effects in jet ejectors." 2010, J. Micromechanics and Microengineering, 20 085027.

Gardner, W G, Jaworski, J W, Camacho, A P, Protz, J M, "Experimental results for a microscale ethanol vapor jet ejector." 2010, J. Micromechanics and Microengineering, 20 045019.

Gardner, W G, Wang, I, Jaworski, J W, Brikner, N A, Protz, J M, "Experimental investigation of scale effects in multi-stage jet ejectors", Proc. Power MEMS, Nov. 20 - Dec. 3, 2010.

Brikner, N A, Gardner, W G, Wang, I, Protz, J M, "Modeling and Design of a Giffard Injector Pumped Microrocket", Proc. Power MEMS, Nov. 20 - Dec. 3, 2010.

Camacho, A P, Gardner, W G, Wang, I, Shen, H S, Jaworski, J W, Gilmore, C K, Pelekies, S O, Dunnmon, J A, Protz, J M, "Experimental Results of an Ejector Driven Micro Turbine Generator", Proc. Power MEMS, Nov.20 - Dec. 3, 2010.

*Proceedings*

Gardner, W G, Jaworski, J W, Wang, I, Brikner, N A, Protz, J M, “Microscale Ethanol Vapor Ejector and Injector”, Proc.of SPIE Micro- and Nanotechnology Sensors, Systems and Applications II, Apr. 5-9, 2010, 7679-98.

Pelekies, S O, Shuhmann, T, Gardner, W G, Camacho, A, Protz, J M, “Fabrication of a mechanically aligned single-wafer MEMS turbine with turbocharger”, Proc.of SPIE Unmanned/Unattended Sensors and Sensor Networks VII, Sept. 20, 2010, 7833-06.

Brikner, N A, Gardner, W G, Wang, I, Protz, J M, “A Study and Design of a Giffard Injector-Pumped Bipropellant Microrocket”, Proc. of the 57th JANNAF JPM 2010, May 3 - 7, 2010.

*In review*

Gardner, W G, Wang, I, Brikner, N A, Jaworski, J W, Protz, J M, “Experimental results and modeling for a microfabricated Giffard jet injector driven by ethanol vapor.” 2010, J.Micromechanics and Microengineering, (under review).

Brikner, N A, Gardner, W G, Shen, H S, Protz, J M, “Investigation of Heat Transfer and Scale Effects on the Performance of a Giffard Injector Pumped Microrocket”, J. Thermal Sciences, (accepted 04/19/11).

He is a member of the American Institute of Aeronautics and Astronautics (AIAA), American Society of Mechanical Engineers (ASME), Society of Automotive Engineers (SAE), and International Society for Photonics and Optics (SPIE).